

Wireless Power Receiving Unit

*Analysis, design and implementation of
inductive power receiving unit for wireless
circuits*

Rikesh Chauhan



Thesis submitted for the degree of
Master in Electronics and Computer Technology
(Microelectronics)
60 credits

Department of Physics
Faculty of mathematics and natural sciences

UNIVERSITY OF OSLO

Autumn 2017

Wireless Power Receiving Unit

*Analysis, design and implementation of
inductive power receiving unit for
wireless circuits*

Rikesh Chauhan



© 2017 Rikesh Chauhan

Wireless Power Receiving Unit

<http://www.duo.uio.no/>

Printed: Reprocentralen, University of Oslo

Abstract

Going wireless has revolutionised handheld and wearable devices today. On comparing battery technology with other aspects of portable device technology, it has been a bottleneck in new innovation of miniaturised electronic devices. In this work, first energy harvesting techniques are discussed followed by wireless power transfer methods. Eventually it is concluded that magnetic resonance inductive power transfer method is most suitable to implement as wireless power transfer method. Then this technique of cordless power transfer is discussed, analysed and implemented assuming BLE as a typical load to be wirelessly powered or charged. In the course of WPT implementation, the modules like inductive link, rectifier and LDO are designed in 90nm CMOS technology. Finally WPT chip is designed and produced. This project concludes with comparison of simulated and measured performance of the WPT chip.

Preface

This work is a thesis project for Master in Electronics and Computer Technology at Department of Physics, University of Oslo. The project topic is provided by Nordic Semiconductor as a part of its R&D work. It was started in Spring 2016 and concluded in Autumn 2017.

First and foremost, I would like to thank both of my supervisors for their valuable guidance throughout my work . Tor Sverre Lande as my internal supervisor from my university, provided me with both administrative and academic assistance precisely when needed. Likewise, Malihe Zarre Dooghabadi as my external supervisor, assisted me with project requirements and implementation. I must also thank Malihe for encouraging me during the challenging times of my project.

I would also like to thank Olav Stanly Kyrvestad, our lab engineer for helping me in finalising my chip, ordering PCB and components and helping in laboratory setup. Similarly I appreciate the PhD students in the department for answering my questions without hesitation. I should also remember my fellow students who were very engaging in discussing my problems and suggesting creative ideas.

Last but not least, I am very thankful to my family and friends who were always motivating and filling me with positive energy to accomplish my project.

I am very grateful to Nordic Semiconductor and my department for giving me an exciting thesis project which gave me an opportunity to learn and experience analog chip designing.

Rikesh Chauhan
1st October 2017, Oslo

Contents

Abstract	i
Preface	ii
Contents	iii
List of Figures	v
List of Tables	viii
I Introduction and Background	1
1 Introduction	2
1.1 Motivation	2
1.2 Thesis outline	4
2 Background	6
2.1 Energy Harvesting	6
2.2 Wireless Power Transfer	9
2.3 This project	15
II Component Design and Analysis	17
3 Rectifier	18
3.1 Introduction	18
3.2 Design	19
3.3 Simulation result	24
4 Low Dropout Regulator	28
4.1 Introduction	28

Contents

4.2 Design	29
4.3 Simulation result	32
5 Antenna Design	40
5.1 Introduction	40
5.2 Inductor Model	42
5.3 Inductive Transfer Link	44
5.4 Magnetic Resonance Coupling	45
III WPT System Design and Implementation	49
6 PMS and WPT Systems	50
6.1 Introduction	50
6.2 Power Management System	51
6.3 WPT System	58
IV WPT Chip Production, Test and Verification	66
7 Test and Verification	67
7.1 Chip and PCB	67
7.2 Measurement Setup	68
7.3 Measurement Result and Discussion	69
V Conclusion	81
8 Conclusion	82
8.1 Design issues	82
8.2 Future Work	84
Appendices	85
A Rectifier Implementation	86
B LDO Implementation	89
C PMS Chip	92
D Test PCBs	95
E Matlab code for PMS measurement	101
Acronyms	104
Bibliography	106

List of Figures

1.1	Mobile performance development trend [1]	3
2.1	Functional block diagram of energy harvesting system .	7
2.2	Power density of energy sources and consumption of electronic devices [5]	8
2.3	Near-field coupling models	10
2.4	Far-field harvesting model	11
2.5	Commercial application of wireless power transfer	13
2.6	Qi	14
2.7	AirFuel	15
2.8	Functional block diagram of complete design	16
3.1	Rectifier topologies: conventional and gate cross coupled	20
3.2	Gate cross coupled full wave active rectifier	21
3.3	Comparator circuit, RCC	23
3.4	Testbench for rectifier	24
3.5	Voltage and current waveforms of the rectifier	25
3.6	Voltages waveform for pre and post layout	25
3.7	Rectified DC output for pre and post layout	26
3.8	Voltage and power conversion efficiency	27
4.1	Generic LDO with pMOS pass device	29
4.2	CMOS implementation of LDO	30
4.3	LDO testbench setup	31
4.4	LDO transient simulation	33
4.5	LDO step load regulation	34
4.6	LDO step line regulation	34
4.7	Regulated voltage with supply variation	35
4.8	Regulated voltage with load variation	36
4.9	LDO stability before and after compensation	37
4.10	PSSR performance	38

List of Figures

5.1	Inductive coupling	40
5.2	Real antenna model	42
5.3	Antenna model	43
5.4	Antenna coupling model	44
5.5	Resonant coupled inductive link	46
5.6	Link reflection loss before and after tuning	47
5.7	Link gain before and after tuning	48
6.1	WPT block diagram	51
6.2	WPT PMS implementation	52
6.3	Test bench for PMS simulation	53
6.4	Input voltage waveform of PMS	54
6.5	V_{rec} and V_{reg} voltages of PMS	55
6.6	Ripple in V_{rec} and V_{reg}	56
6.7	Current and power consumption	57
6.8	Lumped model of inductive link	59
6.9	Input voltage waveforms	60
6.10	V_{rec} and V_{reg} voltages	61
6.11	Ripple in V_{rec} and V_{reg}	61
6.12	Primary voltage and current	62
6.13	Diode current and voltages	63
7.1	Micrograph of PMS chip	68
7.2	Measurement setup	69
7.3	Measured rectifier waveform for 10 mA load	70
7.4	Measured rectifier waveform for 1 mA load	71
7.5	Measured rectifier output for various load	72
7.6	LDO input sweep for 5 mA load	74
7.7	LDO load sweep	75
7.8	PMS performance	76
7.9	WPT from 5 mm coupling: voltage waveform	77
7.10	WPT 5 mm coupling: Voltage and current at primary coil	78
7.11	Primary voltage and current for various inductive link	79
A.1	Schematic of Rectifier	87
A.2	Layout of Rectifier	88
B.1	Schematic of LDO	90
B.2	Layout of LDO	91
C.1	Schematic of PMS chip	93
C.2	Layout of PMS chip	94

List of Figures

D.1 Primary antenna layout	96
D.2 Primary antenna PCB	96
D.3 Secondary antenna	97
D.4 Secondary antenna PCB	97
D.5 Test PCB schematic	98
D.6 Test PCB board layout	99
D.7 Test PCB board	100

List of Tables

2.1	Target specifications	15
3.1	Rectifier design parameters	23
3.2	Rectifier performance summary	27
4.1	LDO design parameters	30
4.2	LDO performance summary	39
5.1	Characterisation of antenna	43
5.2	Coupling parameters for varying coils distance	44
5.3	Performance of resonant inductive link	47
6.1	PMS test-bench stimuli voltages and components	53
6.2	PMS performance summary	58
6.3	WPT performance summary for 5 mm coupling	64
6.4	WPT performance summary for all inductive link	64
7.1	Rectifier measured performance	73
7.2	WPT measured performance for 5 mm coupling	78
7.3	WPT measured performance for all inductive links	80

Part I

Introduction and Background

Chapter 1

Introduction

1.1 Motivation

We start with the technology development trend in microelectronics. The progress of different aspects of technology is discussed and compared with power/battery development. We end the chapter concluding the need for going cordless for supplying power for microelectronics.

1.1.1 Technology Trend

Size and Weight : Lighter and Tighter

Reduction in size and weight has been most dramatic that in course of some decades miniaturisation trend went from a room-sized fixed electronic into a wearable device. Most important milestone contributing for lighter and tighter devices is development of transistor in 1950s replacing large and bulky vacuum tubes, and development first IC in 1965 making it possible to integrated hundreds of transistors on a single silicon substrate of some square mm. Since then as stated by Moore's law, IC size is continuously shrinking. A typical modern IC now consists of billions of transistors of some tens of nm feature size.

Operation: Multi-functional and Higher speed

On the contrary to shrinking device size, integrated functionality and device speed is increasing proportionally. The introduction of SOCs created of new dawn of multi-functionality IC by integrating many electronic components and/or systems on a single silicon substrate. Sim-

Introduction

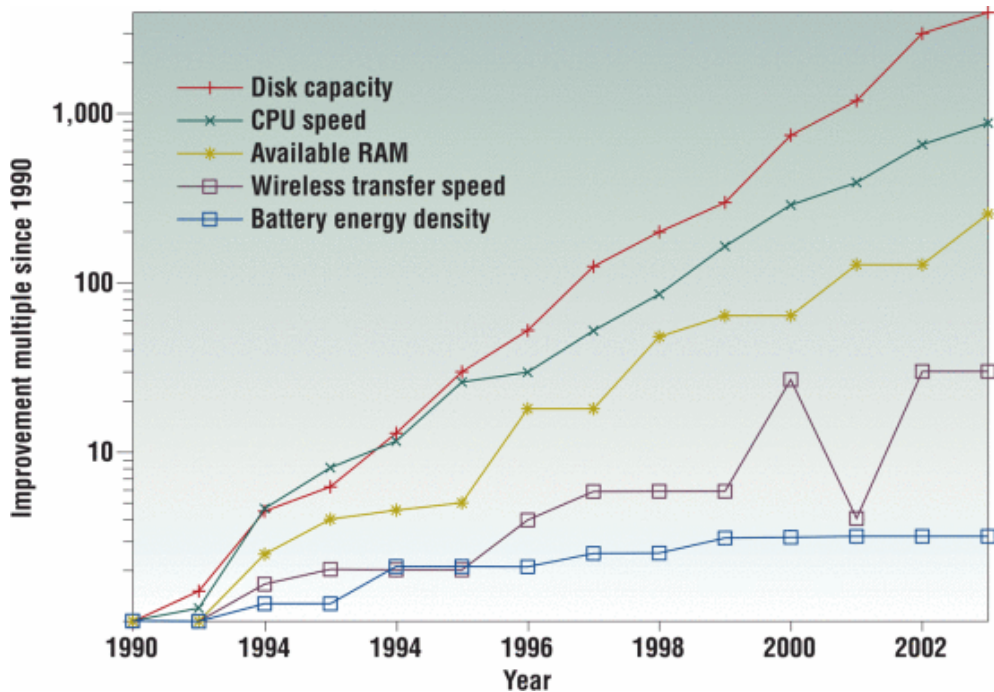


Figure 1.1: Mobile performance development trend [1]

ilarly multi-core CPU with parallel programmed instruction significantly increased work payload as stated by Amdahl's law. Similarly recent developments in IoT has introduced whole new dimension on multi-functionality by connecting many devices to a same local network or the internet[2].

Power consumption: Low-power

In terms of power consumption, though power density has increased due to increased transistor density and speed, power consumption per transistor and energy per operation, EOP, has significantly reduced. It is due to gradual shrinking in feature size and decrease in supply voltage. Similarly there has been a lot progress in LP design introducing new power optimal design techniques both at logic/circuit level and architecture level. Lately run time power optimisation technique by tracing realtime work load like dynamic voltage scaling and switching between different operation modes (sleep, nap, doze and active) have been popularly used to reduce power consumption[3].

Power supply: Cut the Cord

In spite of dramatic technological advancement, battery technology has not evolved equally as good, see figure 1.1. It is not like there has been no progress in battery technology at all. There has been a lot improvements like increased volumetric energy density thereby reducing size, increased gravimetric energy density thereby reducing weight, reduced self discharge thereby increasing life time and increased charged cycle thereby increasing reuse[4]. Today Li-ion has better choice for powering devices because of its better combined above mentioned characteristics and hence used excessively in portable and wearable devices.

But use of battery in today's portable and wearable devices is constraining the overall development of devices. Batteries contribute significant proportion of total weight and size of the device. They supply limited power which means require regular recharge and in the long run need replacement. During recharge either device or battery has to be physically connected to power outlet.

A power source with high power density which perpetually and wirelessly power devices could eliminate all the above problems and challenges mentioned above. But how far have we gone to achieve this? In the next chapter, we will discuss the techniques of energy harvesting and wireless power transfer studied and implemented so far. Bluetooth Low Energy, BLE is taken as a reference device to drive and a power harvesting circuit is designed and implemented for BLE.

1.2 Thesis outline

A brief overview of this thesis report is presented. For better organisation and clarity of content, it is divided into four parts and eight chapters.

- **Chapter 1** discusses the motivation behind this work. It compares technology trends and concludes the need of going cordless power source for modern microelectronics devices.
- **Chapter 2** presents the background for this work. It discusses various energy harvesting and wireless power transfer techniques.

Introduction

- **Chapter 3** onwards, design of functional blocks is discussed. It starts with design and analysis of rectifier topology used.
- **Chapter 4** is about design, implementation and analysis of LDO.
- **Chapter 5** discusses about modelling the antenna required and its performance.
- **Chapter 6** presents design of wireless power harvesting system using the discrete functional blocks and simulation results are presented. First only the power management system is simulated and then complete power transfer system with inductive transfer link.
- **Chapter 7** discusses the production, test and verification of produced power harvesting chip. First test PCB and chip layout is discussed. Then measurement data of the chip is presented and finally compared with the simulated results.
- **Chapter 8** presents summary and concluding remarks of this work including problems and challenges faced along with prospective future work.

Chapter 2

Background

2.1 Energy Harvesting

In this chapter, we discuss the options to eliminate or minimise the bottlenecks of battery used in portable and wearable devices. We start with energy harvesting techniques and then wireless power transfer techniques.

There has been success in harvesting low power from ambient sources and a lot of effort and resources is being used for harvesting high power. As discussed earlier the technological advancement has given us low power electronics. These LP devices can now be powered solely by harvested energy, eventually making battery-less wirelessly powered electronic device a reality.

Energy harvesting system generally constitutes of energy source, transducer and power conditioning unit as shown in figure 2.1. Energy source can either be artificial like human walking or natural like sunlight. Transducer are devices which converts the energy from source which may be to electrical energy. And power conditioning unit process the harvested energy so that it can be used either to directly power a load or to store the energy.

Depending upon the type of energy harvested from the surrounding environment, energy harvesting devices can be broadly classified into kinetic, electromagnetic and thermal energy sources[4]. These are briefly discussed below.

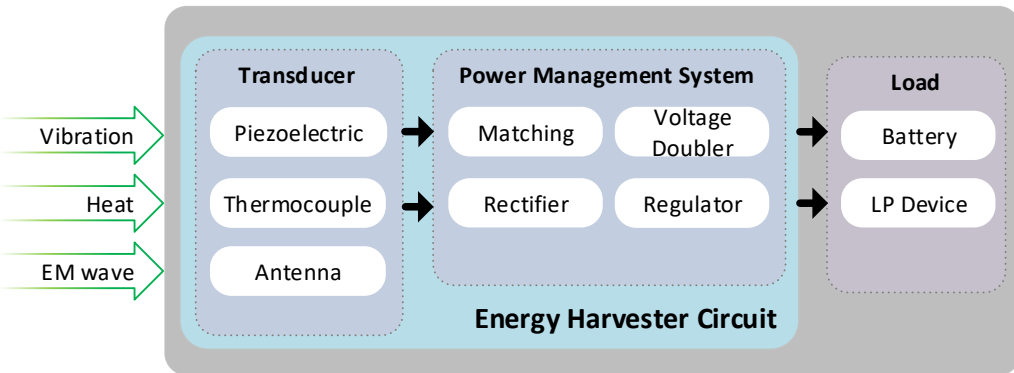


Figure 2.1: Functional block diagram of energy harvesting system

2.1.1 Kinetic energy harvesting

In kinetic energy harvesting, kinetic energy due to mechanical deformation of transducer is converted into electrical energy. Piezoelectrical material is good example of transducer for kinetic energy harvesting. Piezoelectrical materials are those which exhibit piezoelectric effect: when subjected to mechanical strain, it generates electrical charge proportional to applied strain. Strain is applied with either compression, slap or bending of the material.

2.1.2 Harvesting from Radiation

Electromagnetic energy harvesting is extraction of useful energy from ambient light or RF radiation. Solar energy harvesting is the most popular and widely successful EM energy harvesting for large scale energy generation. It makes use of semiconductor device called solar cells as transducer. These transducer converts incident light energy to electric energy due to photoelectric effect: when light is incident on semiconductor, electrons are emitted from the surface. Its application ranges from LP wrist watch to grid of photovoltaic system. The other popular example is harvesting from RF radiation, which are available almost everywhere in modern cities, to power RFIDs. In this technique, antenna or rectenna are used as transducer. However harvesting from RF radiation has been limited to very low power only.

2.1.3 Thermal energy harvesting

Similarly in thermal energy harvesting, thermal energy from any source in the environment is converted to useful electric energy. Thermopile is an example of thermal energy harvesting using thermocouples in series as transducer. Thermocouple is a electric device with two different conductors forming junctions. A thermocouple generates voltage proportional to temperature between junctions, known as Seebeck effect. Connecting thermocouples in series increased the harvested voltage as in thermopile.

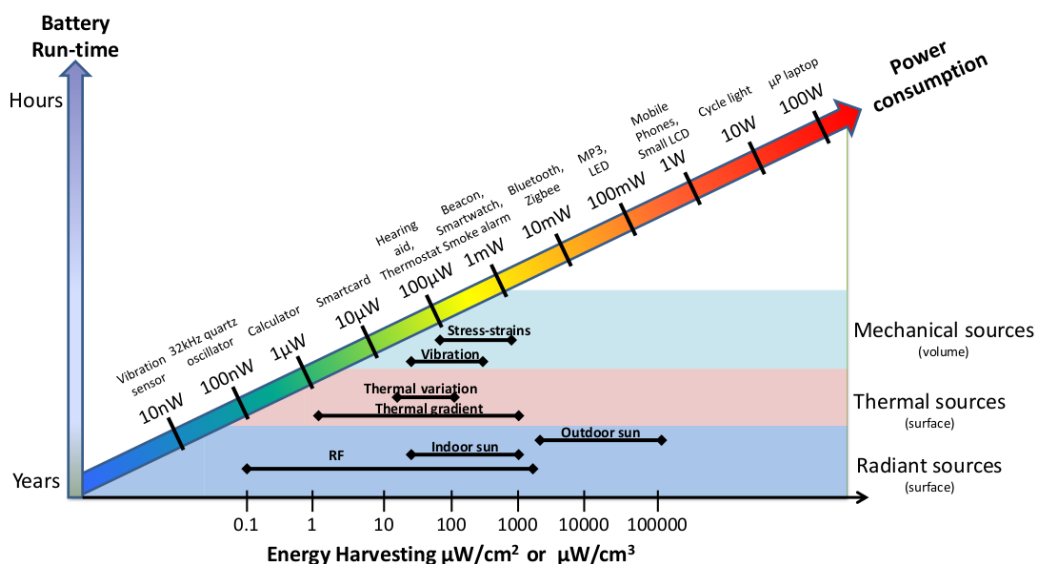


Figure 2.2: Power density of energy sources and consumption of electronic devices [5]

Figure 2.2 shows power density of different energy sources and power consumption of electronic devices. It is seem that the above discussed energy sources have a low power density which means very low power and some low power micro-electronic devices only have the privilege of integrating energy harvesting techniques so far. For most of the devices, the harvested power is not high enough to drive them yet. This means perpetual high density energy source is yet not realisable for most of the devices. But what about wireless transfer of already available power? We will discuss it ahead.

2.2 Wireless Power Transfer

As discussed earlier since the evolution of battery technology is not at par with rest of the development in microelectronic devices and energy harvesting techniques from natural sources has not yet evolved to high power density, wireless power transfer is by far best option to minimise challenges in battery powered devices.

Wireless power transfer is technique of cordlessly transferring electric energy across a air gap either to drive a load or to charge a battery. It eliminates the need of physical power cables to recharge battery. and in the best case completely remove the battery. Wireless power transfer methods implemented today can be broadly classified into radiative and non-radiative power transfer on the basis of transfer distance which can be further sub-classified on the basis of power transfer principle [6] as discussed below.

2.2.1 Non-radiative wireless power transfer

Non radiative method of wireless power transfer based on magnetic field coupling between two coils within the distance of coil dimension. Since magnetic field diminishes rapidly after distance greater than radius of coil, assuming that distance is less than near field and far field boundary, $\lambda/2\pi$ [7, pp. 63], better coupling and hence power transfer can happen only within this short distance, and thus it is also called near field power transfer. Near field also means that radiative EM wave is not yet fully created and hence the name non-radiative WPT. As energy transfer in magnetic field is non radiative, it is safe even to transfer higher power as there is no RF exposure. This is one of the main reason of its widespread application today.

Inductive power transfer, IPT

IPT is based on electromagnetic induction between two coils. Electric energy is transferred by coupling of magnetic field from the primary to secondary coil. As stated by Faraday law of induction, alternating current flowing in primary coil generates varying magnetic filed which is when coupled with secondary coil includes voltage/current across the

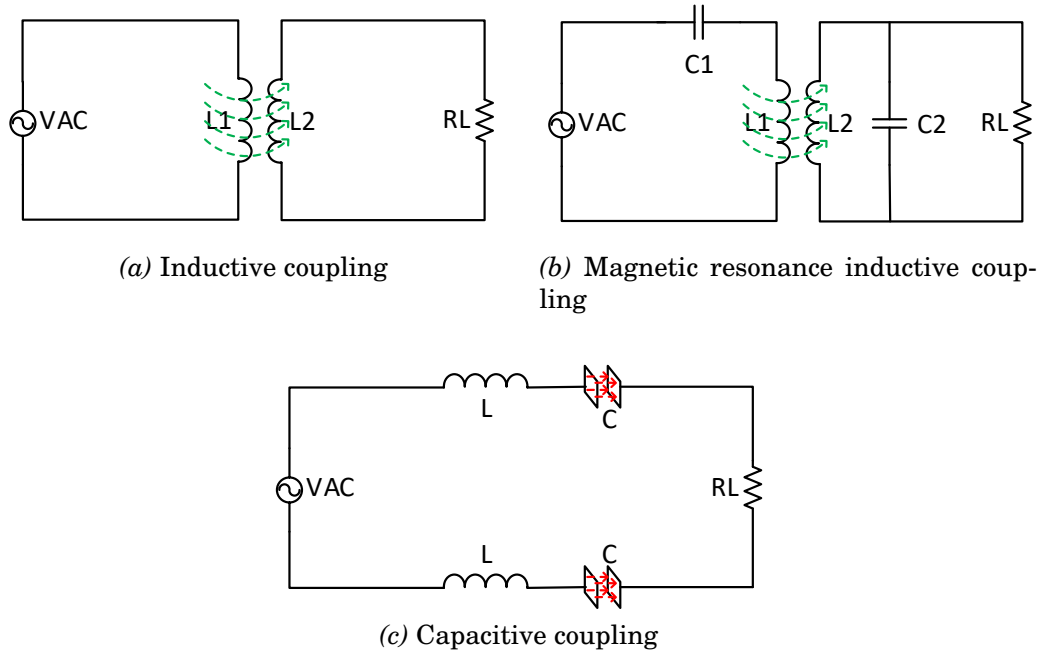


Figure 2.3: Near-field coupling models

secondary coil.

In such conventional inductive coupling, larger air gap and difficulty in perfect alignment between the coils contribute to weak coupling, which directly translates into poor power transfer efficiency. This is why it is mostly used in LP devices and for short range in tens of mm transfer like RFIDs.

Magnetic resonance power transfer

The principle of magnetic resonance power transfer is same as IPT but with strong coupling between the coils. Instead of simple coil as in IPT, resonance is created at both primary and secondary coil at the same operating frequency. Such resonant IPT is often concisely called as Witricity, for wireless electricity and is less affected by coil misalignment and physical distance compared to conventional IPT [8]. A very key application of resonant IPT is that it can be used to simultaneously transfer/charge multiple power receivers from a single large source coil [9].

Because of its strong coupling between the coils, it can effectively transfer power for mid range in tens of cm. It is mostly used in wireless charging of medical implants and consumer electronics.

Capacitive power transfer, CPT

In capacitive power transfer, power transfer is done through capacitive coupling, use of E-field, between sending and receiving plates as transferring interface. For low power transfer, it is seen effective over IPT because of lower cost, smaller size and no shielding for EMI. However for higher power transfer is limited due to requirement of larger plate area and very close coupling [10].

2.2.2 Radiative wireless power transfer

Radiative power transfer uses RF EM wave as a medium to deliver power. In contrast to near field, power is transferred through E-field of EM wave. The E-field can only develop after $\lambda/2\pi$ distance, at far field region, from the source [7, pp. 112], and energy can only be harvested in this far field region, it is called far field power transfer. However as EM wave is radiative and high power RF exposure has safety concerns on human.

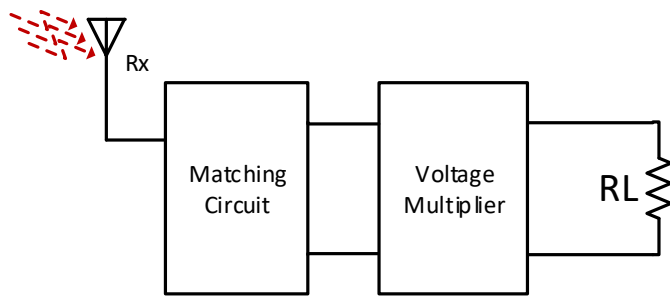


Figure 2.4: Far-field harvesting model

Non-directive and directive radiative WPT

Radiative power transfer can be divided into directive and non-directive radiative power transfer. Non-directive power transfer is same as discussed in EM energy harvesting, where energy is harvested from isotropically radiated RF wave in the surrounding. Whereas in directive power transfer, dedicated transmitter antenna/antenna array is used to transmit EM wave to a particular direction of receiver antenna location. This point to point far field transfer technique is also called energy beam-forming and has better transfer efficiency than non-directive method.

Health concerns as governed by FCC and IEEE safety regulation policy on human exposure has limited its use to low power harvesting over longer distance using RF wave. But, as RF wave is also information carrier wave in wireless communication, its capacity to transmit both data and power simultaneously is expected to introduce new application in wireless communication field [6].

2.2.3 WPT Applications

It is seen today that IPT and magnetic resonance IPT are mostly used because of easier implementation, lower cost, wide range power transfer capability. For high power transfer in order of kilowatt, IPT is mostly used in the field of industrial automation like automated material handling and industrial micro-robots and automotive like electric vehicle charging. Similarly both IPT and magnetic resonance IPT are used for transferring power medium power up-to tens of watt. Their typical uses have been in charging battery in medical equipments and consumers electronics. In case of microelectronics devices like medical implants, body sensors, pacemaker etc, magnetic resonance IPT is mostly used both to charge a battery or directly drive the device.

In context of radiative power transfer, non-directive technique is mostly used in low power sensors and implants. Because of the low power requirement, mostly omnipresent RF signals are used to harvest energy. This technique has been used in both perpetually supplying power like in body sensor which continuously monitor some activity or sporadically supplying power like in RFID and body implants which work only when required. [6] reports future application

Background

of microwave power transfer can be in SPS (Solar Power Satellite) system and SHARP (Stationary High Altitude Relay Platform). SPS uses satellite for harvesting solar energy in space and transfer that power to earth. Similarly SHARP is stationary charging station for unmanned aerial vehicles in stratosphere region by beaming power from earth.



(a) Qualcomm EV charger

(b) Qualcomm mobile phone charger with foreign object detection feature



(c) IDT concept of wireless charging of bionic devices

Figure 2.5: Commercial application of wireless power transfer

2.2.4 Charger Standards

When wireless charging was introduced into consumer daily appliances, it was quickly realised the need of standard design protocols to maintain uniformity and avoid confusion for the manufacturers. Here are some mostly used standards in the market. Most common commercial standards are discussed below use both IPT and resonant IPT techniques for charging, and have two elements: transmitter for transferring power and receiver device usually integrated into mobile, handheld or wearable devices. Both the transmitter and the receiver use the same control and management protocol in order to detect compatible electronic devices, exchange charging state information and control charging process.

Qi

Qi standard was introduced by Wireless Power Consortium in August 2008. It has standardised two categories of chargers: low power charger for mobile and music players and medium power charger. The power transfer was based on IPT and now is operating with magnetic resonance IPT too. Qi standard allow transmitter/charger to be either single fixed coil, single moving coil or array of coils. The transmitter coil type determines the positioning of the receiver, either guided or free. Qi charger also have foreign object detection feature [11]. Qi uses the same frequency for communication and power transfer, 80-300 KHz [12].



Figure 2.6: Qi

A4WP

A4WP is another independent wireless charging standard. It uses magnetic resonance IPT technique for power transfer. The main differences between A4WP from Qi are multiple device charging from a single charger, also called power transmitting unit, PTU and longer charging range. Similarly there are different category of PTUs from 1 to 5, most of them still on roadmap and supports wireless charging

from low power to high power. A4WP used different frequency band for communication and power transfer, which are 2.4 GHz and 6.78 MHz respectively [13].

AirFuel Alliance

AirFuel Alliance is newly created wireless charging standard by merging Alliance for Wireless Power, A4WP and Power Matters Alliance, PMA in 2015 with backing of major device manufacturers [14]. Like A4WP, PMA was IPT based independent wireless charging standard. AirFuel Alliance is believed to fight the market dominance of Qi standard. AirFuel is expecting to expand charging standard beyond consumer electronics to industrial, medical and military applications [15].



Figure 2.7: AirFuel

2.3 This project

As mentioned in the last chapter, a typical microelectronics system, BLE, used extensively in all portable and wearable is taken as a reference load for this project. The purpose of this work will be to make a wireless power transfer system for cordlessly driving a load or charging a battery of 1.8 V with 10 mA current. The target specification for this work is listed in table 2.1.

Table 2.1: Target specifications

Technology	TSMC 90nm 9M-1P
Chip area	TBA mm ²
Input AC voltage	2.5 Vp
Operating frequency	13.56 MHz
Maximum load	10 mA
Output DC voltage	1.8 V

Background

Figure 2.8 is the functional block diagram of proposed implementation of wireless power transfer in this work. From the discussion in wireless power transfer section, it is seen that IPT is the best option for being mature, easy and safe implementation. Since tuning the IPT transfer link at the operating frequency increases the transfer efficiency, magnetic resonance link is designed for this work. The antennas are designed with the specifications provided by Nordic Semiconductor. The power management system includes rectifier, LDO and reference and bias circuit. The biasing and reference circuit is designed solely for learning the design technique without much effort on the accuracy of the generated biases and references. So externally supplied bias and reference will be the secondary option.

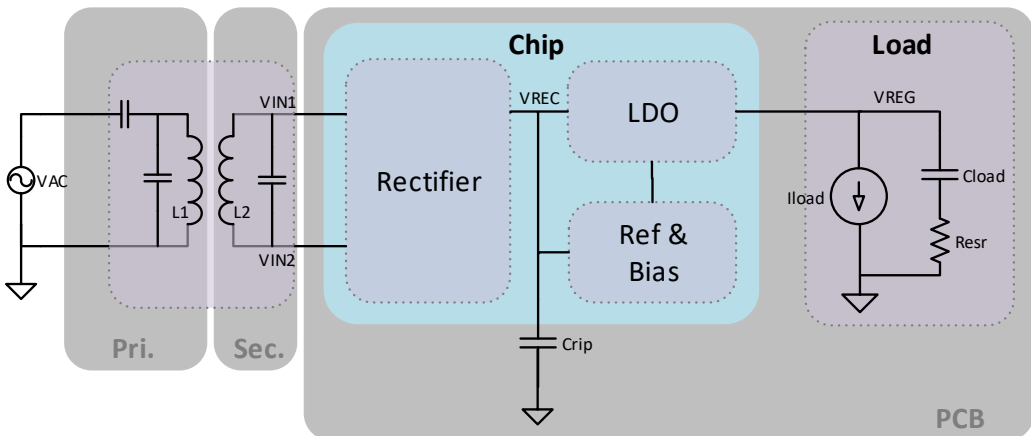


Figure 2.8: Functional block diagram of complete design

The chapter ahead discusses the design, analysis and implementation of the functional blocks in figure 2.8 starting with rectifier. The physics behind each block will be less discussed, however the design choices and reasoning of choices will be clearly stated. 2.5 V transistor of 90 nm process is used because most of the similar work are done in higher technology nodes. So this choice is taken as design challenge.

Part II

Component Design and Analysis

Chapter 3

Rectifier

3.1 Introduction

The most basic rectifier is conventional full wave bridge structure where the diodes are replaced by the diode connected MOS devices in CMOS technology. This topology though being simple to implement, has a major drawback. It requires at least twice the threshold voltage, V_{tn} , of a MOS device as there are two diode connected MOSEs in the conduction path for each cycle of the input signal.

Gate cross coupled and fully gate cross coupled topologies are improvements over conventional full wave rectifier. In gate cross coupled rectifier, two diodes of conventional rectifier is replaced by two gate cross coupled MOSEs working as switches where the voltage drop for every cycle is reduced to one threshold voltage. Similarly, in the fully gate cross coupled rectifier, all diodes are replaced by switches and hence the voltage drop is further reduced to twice the conduction drop only for every cycle. Even though this topology has least voltage drop, it suffers from the problem of reverse charge leakage because when the input ac amplitude is less than the output rectified voltage and the conducting pass devices are on simultaneously and current flows backward from output to input.

All the above discussed topology suffer from either large voltage drop or large power loss because of which their use are limited in low power and low voltage devices. The popular techniques for higher efficiency are using gate cross coupled rectifier along with passive or active circuitry for controlling other two pass devices. In passive rectifier,

additional circuitry including bootstrap capacitor are used to reduce or eliminate threshold voltage one of which is discussed in this paper [16]. However, use of on-chip bootstrap capacitors limits its use where chip area and speed is of importance. On the other hand, in active rectifier, active circuitry is used to control pass devices. The use of active circuitry increases both Voltage Conversion Efficiency (VCE) and Power Conversion Efficiency (PCE) because the pass devices are made to conduct in linear region and hence less conduction drop, and reverse current flow can be completely eliminated and hence less power loss. However active rectifier is not problem free either. The major issue is starting of the active circuit as there is no regulated supply during start up.

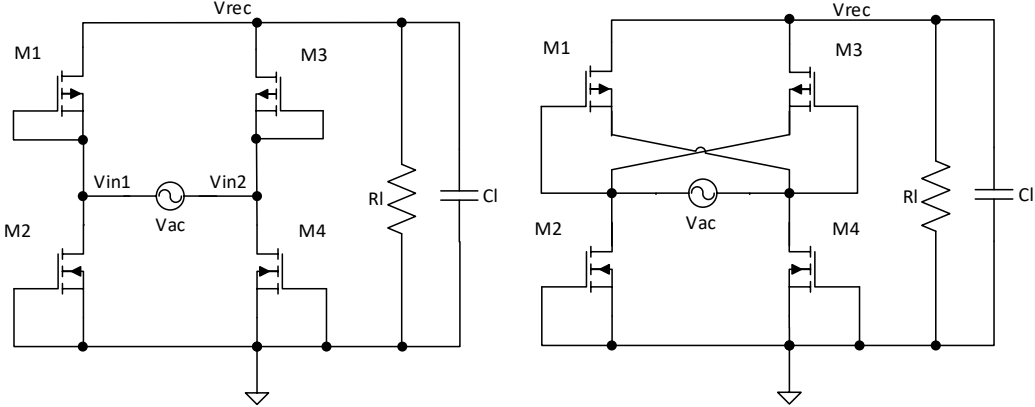
3.2 Design

In this project, active rectifier is chosen, primarily for better VCE and PCE and secondarily to avoid the use of large on-chip capacitors. [17] and [18] have discussed same active rectifier topology with a slight difference in active circuitry. [17] has implemented a comparator with compensating the delay of comparator's output falling whereas [18] has implemented a comparator with compensating both the falling and the rising delay of comparator's output in expense of added circuit complexity and power consumption. [17] has been used here for its simple design.

Figure 3.1a, 3.1b and 3.2 is the CMOS implementation of conventional full wave bridge rectifier, gate cross coupled rectifier and proposed active rectifier in [17]. The problem with 3.1a and 3.1b has already been briefly mentioned above. Though 3.1b is significantly improvement over 3.1a, it is still not a favourable topology with respect to the design technology chosen. In the gate cross couple rectifier of 3.1b, the cross coupled pMOSes act as switches, so the only voltage drop across them is conduction drop due to channel resistance. However the other two nMOSes are diode connected, so they have at least V_{tn} drop across them which means $V_{in} \geq V_{dc} + V_{tn}$ for conduction.

The proposed active circuit in 3.2 is improvement over 3.1b which eliminates V_{tn} drop required for conduction by replacing diode connected nMOS with devices controlled by active circuit as shown in figure 3.3. The active circuit is a four input comparator that turns on nMOSes

Rectifier



(a) Conventional full wave bridge rectifier (b) Gate cross coupled full wave rectifier

Figure 3.1: Rectifier topologies: conventional and gate cross coupled

fast when $Vin > Vrec$ and turns off fast to avoid flow of current.

For the illustration of operation of comparator, consider the case when $Vin1 > Vin2$ i.e. $Vin1 > 0$ and $Vin2 < 0$. During this half cycle, comparator $D1$ output is low and turns off $Mn2$ and also, $Mp1$ is reversed biased and hence there is no path to flow current along $Mn2$ and $Mp1$. For simplicity, assume $Vin = Vin1 - Vin2$. When Vin reaches Vtp , $Mp3$ turns on which shorts $Vin1$ to $Vrec$. When $Vin > Vrec$, $D2$ output goes high, which turns on $Mn4$ and starts the conduction path for the first half cycle and starts charging Cl . When Vin reaches maximum, it starts to decrease and at $Vin < Vrec$, conduction stops as output of $D2$ is low and $Mn4$ is off. As Vin further decreases to below Vtp , $Mp3$ is off too. This way rectifier in 3.2 conducts during positive half cycle eliminating the Vtn drop seen in 3.1b. Now the only drop is the conduction drop due to channel resistance of two pass devices along the conduction path. This drop is much less because during conduction both the device are operating in the linear region with small resistance. The operation is similar for $Vin2 > Vin1$ where $Mn4$ and $Mp3$ are off and $Mn2$ and $Mp1$ conduct to charge Cl .

Figure 3.3 is the implementation of four input comparator $D2$ used in 3.2 as proposed in [17]. It is designed to self power and bias because no steady state supply is available at start up. $M1$, $M2$ and $M7$ monitors voltage across $Mn4$ i.e $Vin2 - Vgnd$ and $M3$, $M4$ and $M8$ monitors voltage across $Mp3$ ie $Vin1 - Vrec$. So when $Vin1 - Vrec > Vin2 - Vgnd$

Rectifier

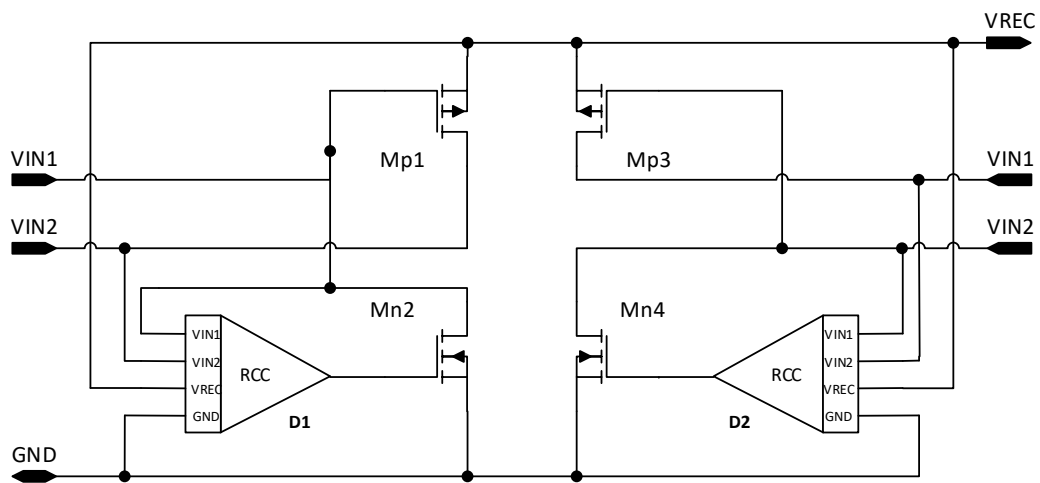


Figure 3.2: Gate cross coupled full wave active rectifier

which means $V_{in} > V_{rec}$, output of $D2$ is high and turns on $Mn4$ instantly. But when $V_{in} < V_{rec}$, the output of comparator is delayed to fall which causes $Mn4$ to conduct in reverse direction leading to significant reduction in power delivered to load. $M8$ is introduced in order to overcome this problem which adds offset currents to increase V_{an} and V_{pn} faster, causing the output to decrease faster and turns off $Mn4$ before $V_{in} < V_{rec}$. This reverse current control technique compensates the comparator delay and increases the power efficiency of the rectifier.

The design parameters for the rectifier is listed in table 3.1. The dimensions of the pass devices are first hand calculated by using square law current equation and devices parameters values given in the technology documents, and later optimised with simulation tool in order to make the rectifier to deliver the required current. Since nMOS does not have to have same device size as pMOS to deliver same current, optimal size ratio equation from [19] is used to find nMOS pass devices sizes. Thought maximum load for this work is 10 mA, It is always simulated with 1 mA extra load. This extra current is to account for the fact that RCC is self powered and LDO which will follow this rectifier will be powered by V_{rec} . Similarly, the value of ripple rejection capacitor is chosen 100nF. This size of filter capacitor is calculated from capacitor current-voltage relationship with the assumption of keeping peak to peak ripple voltage below 5 mV to deliver 11 mA current.

Rectifier

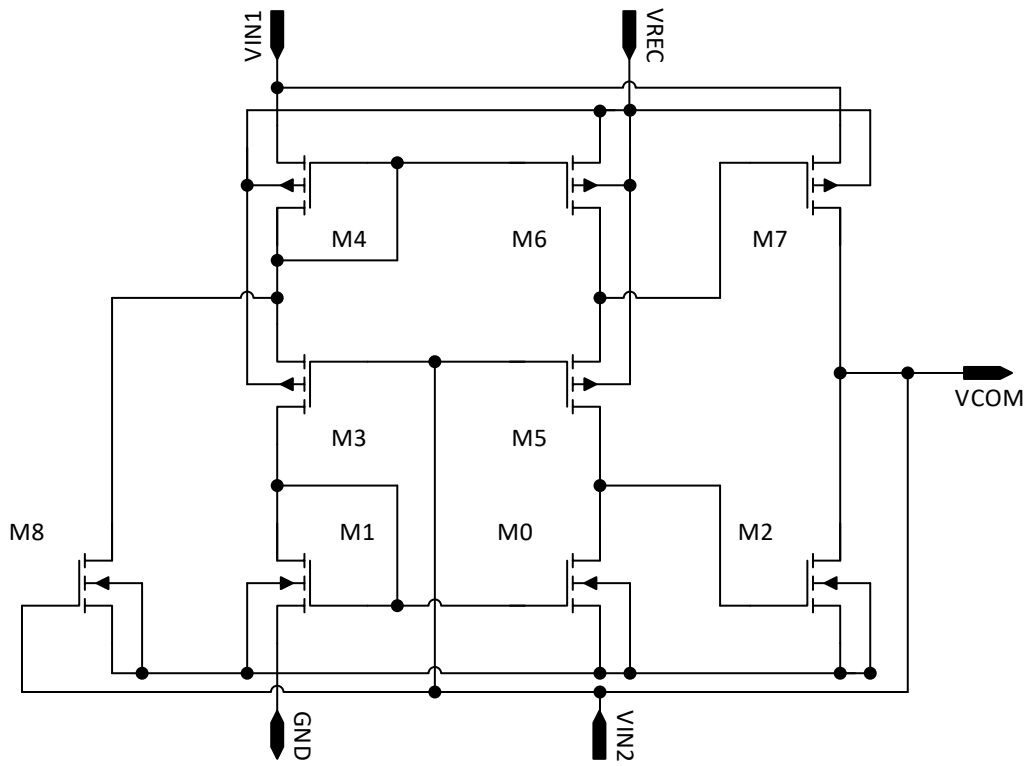


Figure 3.3: Comparator circuit, RCC

Table 3.1: Rectifier design parameters

Wn/Ln, Wp/Lp	720um/280nm, 1.2mm/280nm
Rectifier area	TBA mm ²
Operating frequency	13.56 MHz
Input ac magnitude	2.5 Vp
Load current	11 mA
Ripple rejection capacitor	100 nF

3.3 Simulation result

3.3.1 Transient performance

Figure 3.4 is the test bench setup for simulation of the rectifier. Figure 3.5 show the simulation results showing voltages at the input ac and output rectified DC voltages and current through rectifying MOSes. These waveforms clearly follows the working principle discussed above. Two important observations can be made from plots. First, the rectified output V_{rec} is 2.2 V for V_{pp} ac input of 2.5 V for driving which means the voltage loss has been significantly reduced and the loss of around 300 mV yields to the conduction loss due the channel resistance. Secondly, the reverse current from output to input has been effectively eliminated as there is only positive current flowing to the load when all conducting devices are on.

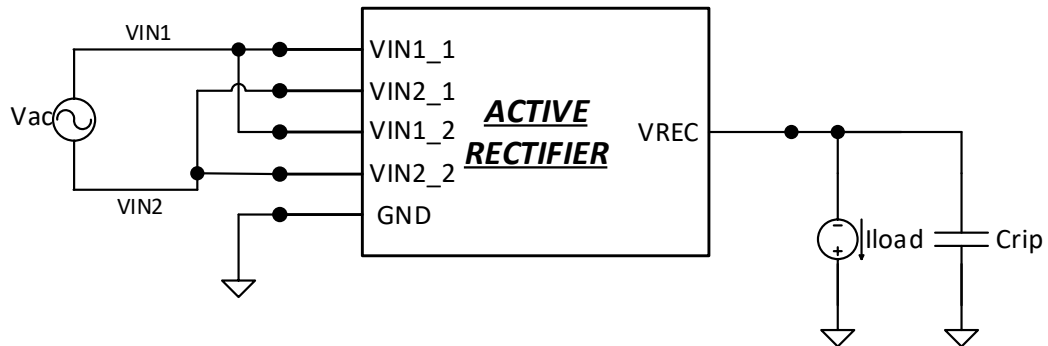


Figure 3.4: Testbench for rectifier

Figure 3.6 presents both pre and post layout results of input voltages, $Vin1$ and $Vin2$ and output voltage, V_{rec} , for one cycle of ac input. The closer view of rectified output is shown in figure 3.7. The voltage drop of about 60 mV in layout result is accounted for the voltage drop due to the resistance of high current conduction path.

Rectifier

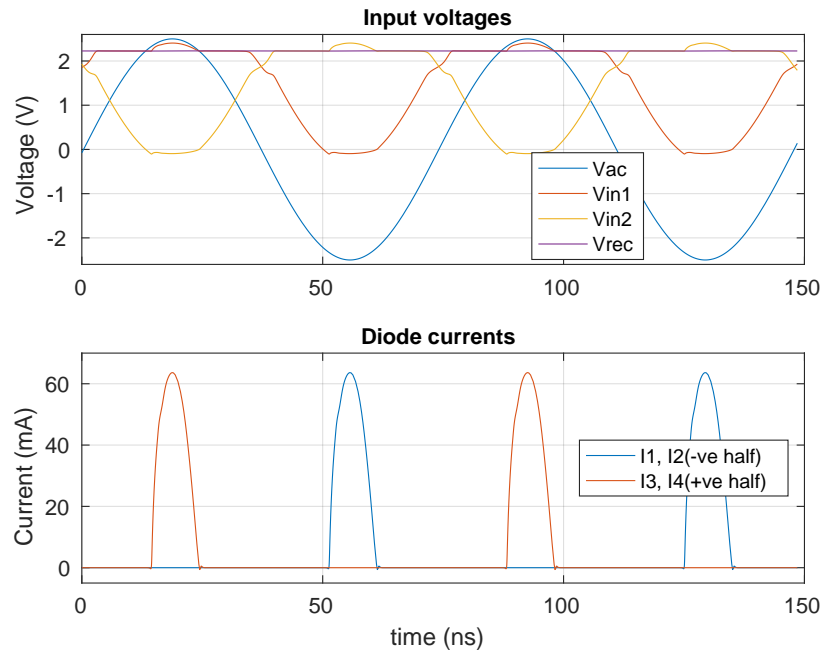


Figure 3.5: Voltage and current waveforms of the rectifier

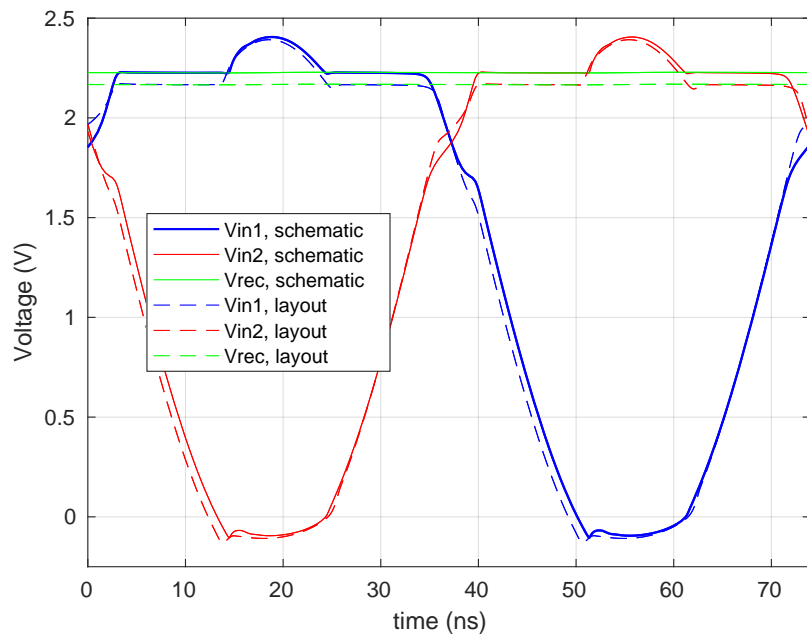


Figure 3.6: Voltages waveform for pre and post layout

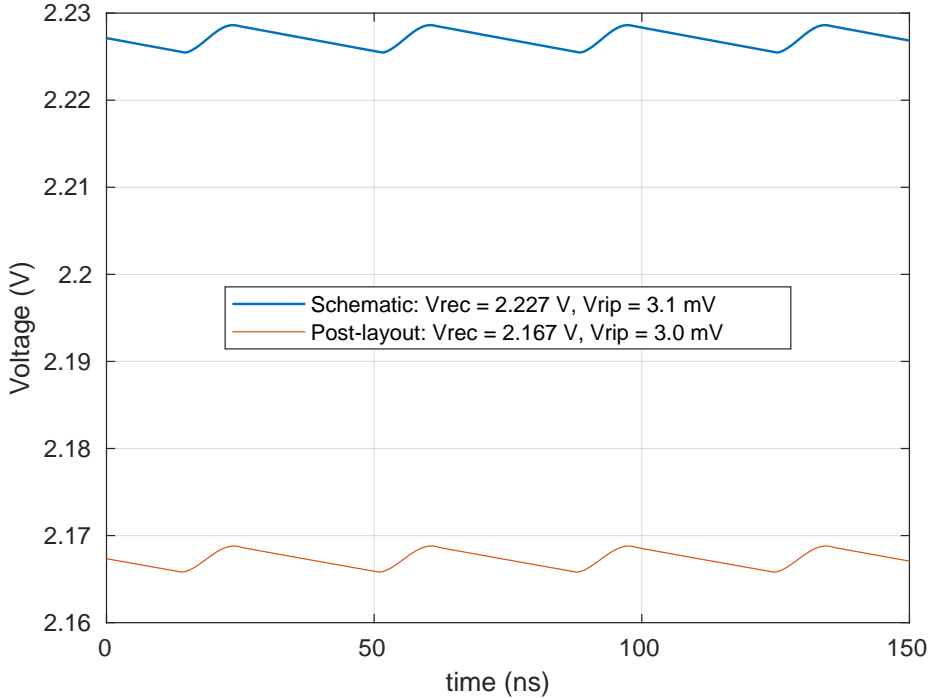


Figure 3.7: Rectified DC output for pre and post layout

3.3.2 DC performance

Similarly, figure 3.8 shows PCE, ratio of powered delivered to load to average power from the source and VCE, ratio of rectified DC, V_{rec} to peak ac input, $|V_{in}|$ with respect to magnitude peak ac input signal. $|V_{in}|$ is gradually increased in peak magnitude in step of 50 mV and VCE and PCE is calculated for every step. The plot shows both PCE and VCE are very less for input ac amplitude less than 1.8 V. It can be explained by the fact that required bias current and gate drive voltage for RCC circuit are not achieved for smaller input.

Table 3.2 comparatively summarises performance for pre and post layout result of the design. The layout design is attached in appendix. The layout is made symmetrical with four inputs, as seen in test bench figure 3.4, instead of two. This is done to make the current conducting path equal which result in equal drop in voltage when it reaches the rectifying MOSes. Similarly the paths from the pad to the rectifier inputs are mask blocked for random metal fill to avoid inter layer

coupling. The high current conduction routes are designed with wide parallel path of many higher level metal layers for reducing resistance in conduction path.

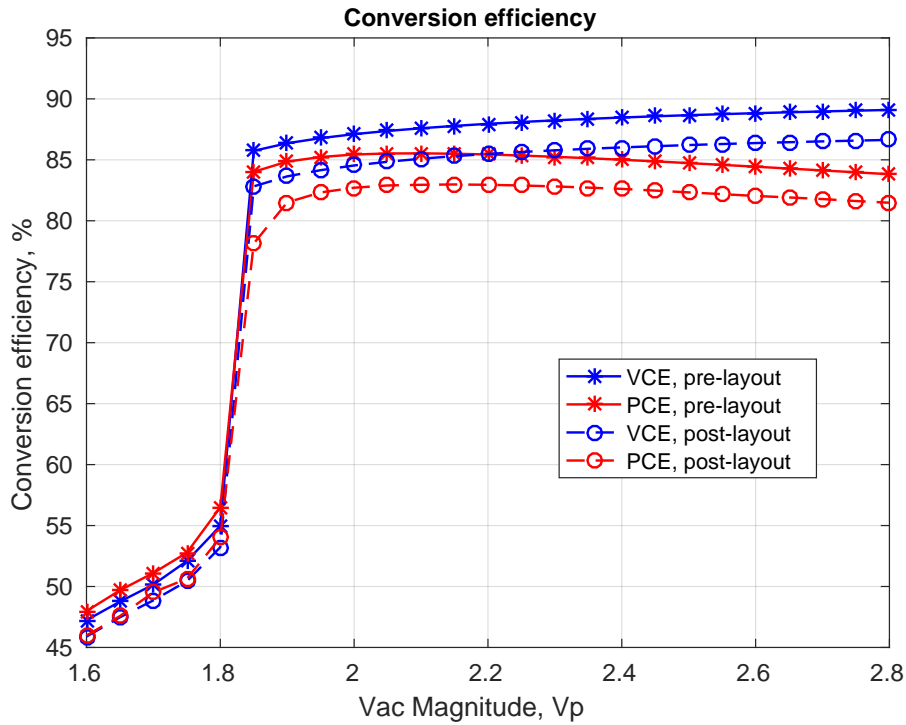


Figure 3.8: Voltage and power conversion efficiency

Table 3.2: Rectifier performance summary

	Schematic	Post-layout
Rectified DC	2.23 V	2.17 V
Ripple Vpp	3.1 mV	3 mV
Peak diode current	63.7 mA	63.1 mA
PCE	84.5 %	82.9 %
VCE	88.6 %	86.2 %

Chapter 4

Low Dropout Regulator

4.1 Introduction

Voltage regulator follows the rectifier designed above in order to regulated the rectified voltage to 1.8 V and deliver maximum load current of 10 mA. Since the output from the active rectifier is 2.2 V and the required regulated voltage is 1.8 V, charge pump or SMPS of boost type is irrelevant here. Buck SMPS could be an option for voltage regulation but LDO is preferred for it better performance in terms of noise and faster settling of regulated voltage. [20].

Figure 4.1 shows a circuit of typical LDO with pMOS as pass element. As shown in the figure, the components includes an error amplifier (EA), a pass device (M_{pass}), a feedback circuit (R_1 and R_2) and load (C_{out} and I_{load}). A more general and complete LDO circuit also includes circuitry for generation of reference voltage and bias current/voltage. In this project it will be discussed separately later. The working principle of LDO is that the error amplifier compares the scaled down regulated voltage, V_{div} with V_{ref} and regulates the internal resistance of the pass transistor such that the error, $V_{ref} - V_{div}$ is least or zero ideally.

[21] and [22] discusses two examples of CMOS implementation of LDO. [21] has proposed bulk modulation technique for improving load regulation and stability of capacitor-less LDO. Similarly [22] has proposed techniques for increasing current efficiency of LDO especially at no or low load condition. Though the techniques discussed in these designs have not been used, they have given good insight into different design parameters of LDO.

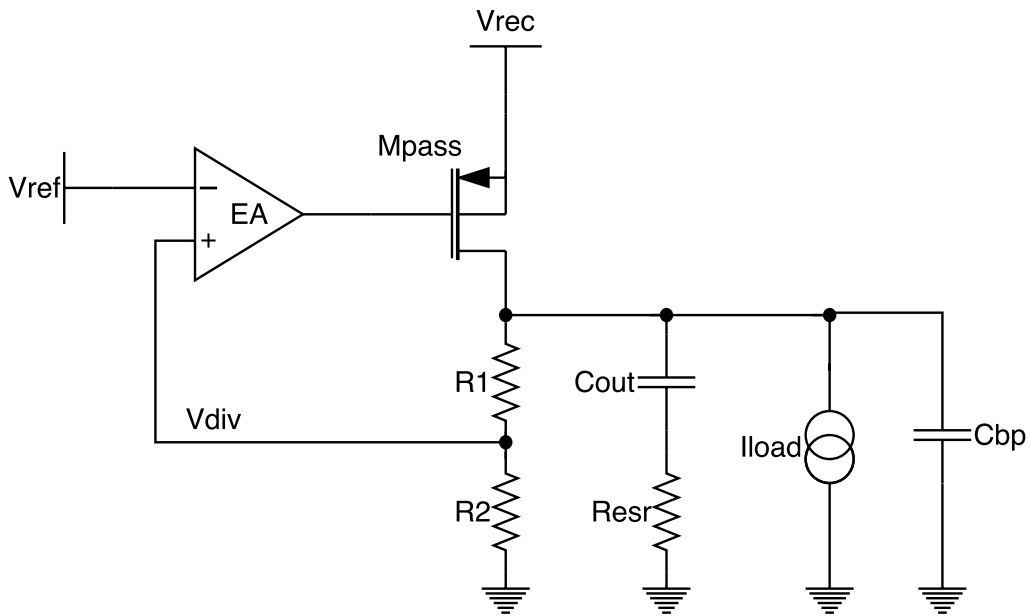


Figure 4.1: Generic LDO with pMOS pass device

4.2 Design

Figure 4.2 shows the CMOS implementation of LDO in this project. The components in this design include a folded cascode differential amplifier as error amplifier, pMOS buffer, pMOS pass device and feedback network of resistors.

As briefly mentioned above, the error amplifier amplifies the error i.e. difference in scaled regulated voltage, V_{div} and reference voltage, V_{ref} . It is known that an amplifier with higher open loop DC gain reduces the closed loop gain error and hence amplifier with higher gain is desired here which in turn increases the accuracy of regulated voltage, V_{reg} [21]. Typically error amplifier has gain $> 40dB$ which is not achieved with a single stage amplifier with this technology. Higher gain can be achieved by cascading multiple single stage but with increased difficulty in making the multistage amplifier stable. So for achieving higher DC gain and at the same time for stability convenience, folded cascode amplifier [23, pp. xx] is chosen.

Low Dropout Regulator

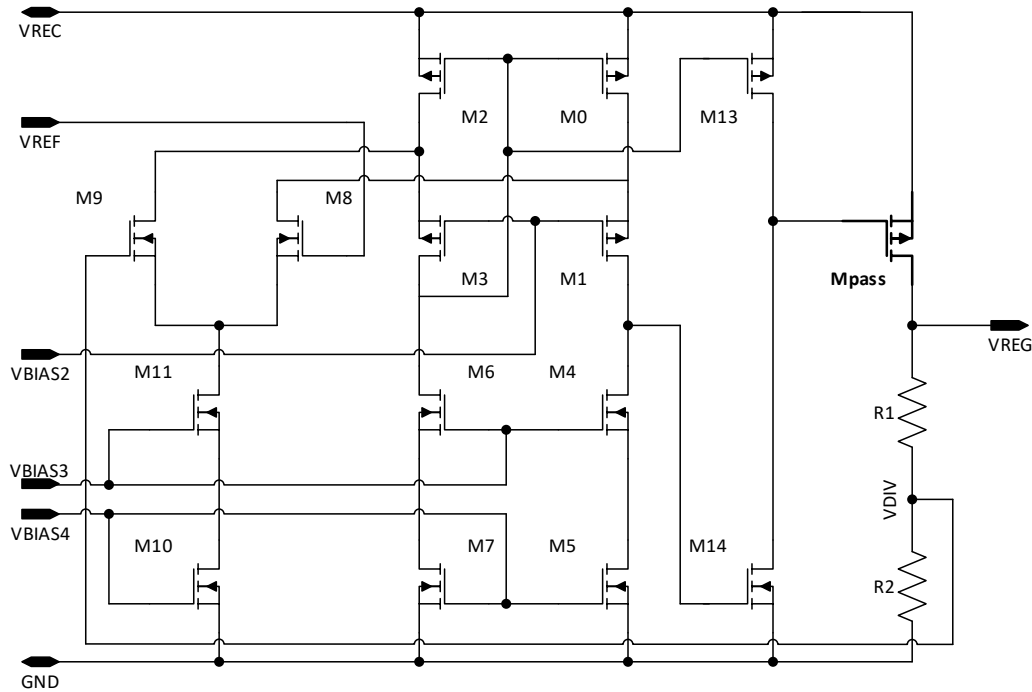


Figure 4.2: CMOS implementation of LDO

Table 4.1: LDO design parameters

Pass device	pMOS
$(W_p/L_p)_{pass}$	540um/280nm
Input supply	>2.2 V
Error amplifier	folded cascode
V_{bias2}	1.1 V
V_{bias3}	0.88 V
V_{bias4}	0.68 V
V_{ref}	1.18 V
C_{load}	> 2.5 μF
R_{esr}	> 0.5 Ω
Regulated output voltage	1.8 V
$I_{load \text{ max.}}$	10 mA

The amplifier has a nMOS differential input stage, preferably for its higher mobility for achieving more gain. Reference voltage, V_{ref} will

Low Dropout Regulator

be bandgap voltage, 1.17 V, of silicon and thus ICMR for EA lies almost at half the supply voltage. This amplifier drives a pMOS buffer which is used to supply sufficient current to drive the large pass transistor. Moreover, pMOS as a buffer passes 1 better which means it can turn off the pass device completely and hence LDO regulates better at low load or no load condition. However for heavier load/larger load current, this pMOS buffer is not able to pull down the gate of pass device sufficiently lower. This is overcome by making the pass device large enough to feed the required maximum load current.

The pass device is a pMOS transistor in this design. It is chosen because it has several advantages over its counterparts like nMOS and BJT devices in terms of dropout voltage, quiescent current, input voltage, thermal response and noise[24]. Prominently, there are two factors that give pMOS edge over other devices; dropout voltage and quiescent current, when it comes to application in low power and low voltage devices. nMOS as a pass device requires a positive drive voltage with respect to output to operate. On the other hand, pMOS is driven by a negative signal with respect to input which means pMOS is preferable for a low input LDO. Similarly compared to BJTs, pMOS requires less headroom and less quiescent current to be driven[24], [25], which means low dropout and low power operation, typical requirement of today's micro devices' power supply.

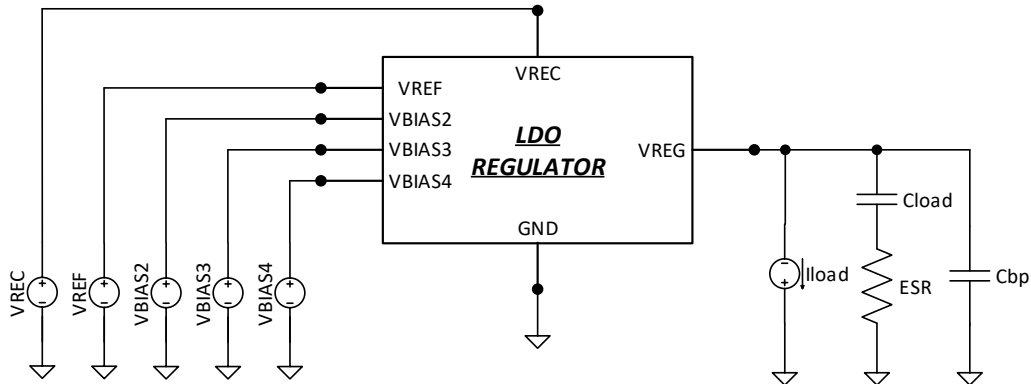


Figure 4.3: LDO testbench setup

However, pMOS as a pass device in LDO causes challenges in stability. As mentioned above, LDO utilises a high gain feedback loop in order to provide a regulated output voltages independent of load cur-

rent and in any system with feedback loop, the locations of poles and zeros determine stability of the system. In case of the pMOS LDO, the pass device is configured in a common source configuration. LDO with big output cap has a dominant pole at the output, which is a low frequency pole. The second pole is located at the gate of pass device because as mentioned earlier pMOS pass device is large and has a big parasitic capacitance. This second pole may be located closer to the dominant pole, resulting in significant reduction in phase margin (PM). Consequently, this may lead to instability of the LDO with pMOS pass device. Various methods have been implemented for ensuring the stability of the pMOS LDO. In this project, a large external capacitor, C_{load} in figure 4.1, is used for stabilising the system at the cost of additional settling time. When an external capacitor is used for designing a stable LDO, the minimum value of capacitance, C_{load} and minimum value of its equivalent series resistance (ESR), R_{esr} should be specified[25]. C_{load} determines the dominant pole of the LDO and R_{esr} in series with C_{load} introduces a left half plane zero below unity gain frequency, UGF of LDO in order to cancel out the non-dominant pole below UGF, producing a stable LDO system.

4.3 Simulation result

4.3.1 Transient response

Figure 4.4 is the transient simulations of the LDO which illustrates generation of regulated output voltage, V_{reg} for both maximum load, 10 mA. For maximum load, it takes around 210 us to produce stable voltage. Since a large capacitor is used for stabilising LDO, it takes longer time to settle to final steady value. A slight longer time to stable value in post layout can be accounted additional parasitic capacitance of interconnects at the output of LDO.

Figure 4.5 and 4.6 show the transient response of LDO for line, V_{rec} and load, I_{load} variation. It gives information about how well and how fast regulated output settles for line and load variations. In figure 4.5 load is given as pulse varying from 10 uA to 10 mA with both falling and rising time of 1 ns keeping input supply constant to 2.2 V. Sudden increase in load causes the output voltage to drop. The error amplifier then takes some time to adjust the gate voltage of pass device to low to

Low Dropout Regulator

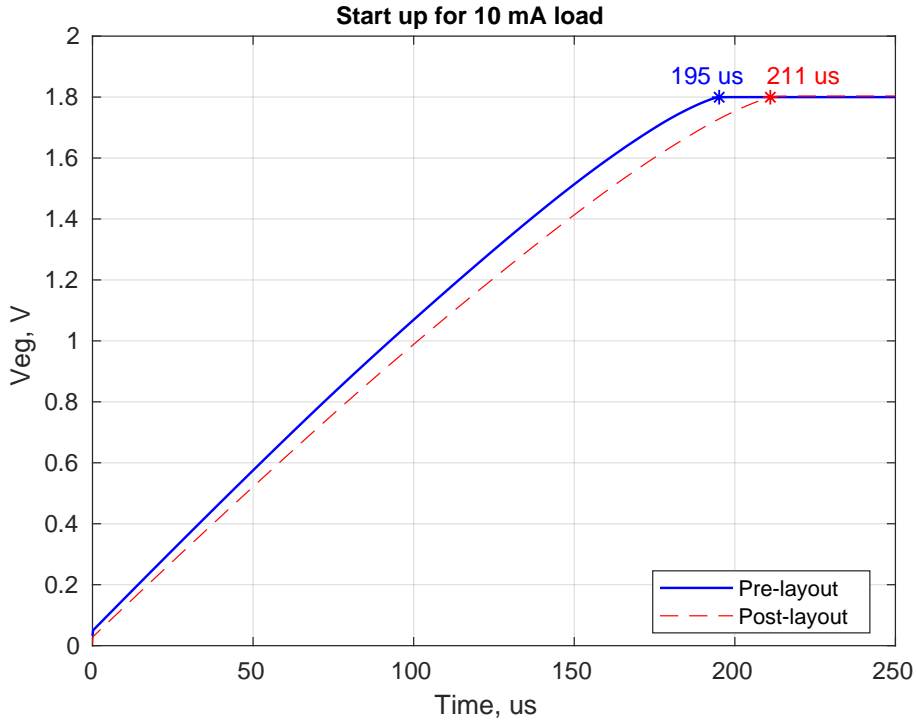


Figure 4.4: LDO transient simulation

fully turn on the device. Likewise when the load suddenly drops to minimum, it causes the output voltage to increase. Again error amplifier adjust it back by increasing the gate voltage of pass device to turn it off. Similarly for line variation observation, input, V_{rec} is pulsed from 2 V to 2.5 V with 1 ns rising and falling time keeping load current constant to 10 mA. Sudden increase in input voltage causes output to increase and vice-versa. As in load variation case, similar recovery pattern is seen. In both case of load and line regulation, the out put voltage is maintained quickly, less than 0.15 us. Both results from schematic and post layout have same transition behaviour except post layout result offset by 3.7 mV as explained in DC response section below.

Line regulation, change in regulated output voltage due to maximum change in input voltage and load regulation, change in output voltage due to maximum change in load current are calculated from values shown in respective plots and are listed in table 4.2.

Low Dropout Regulator

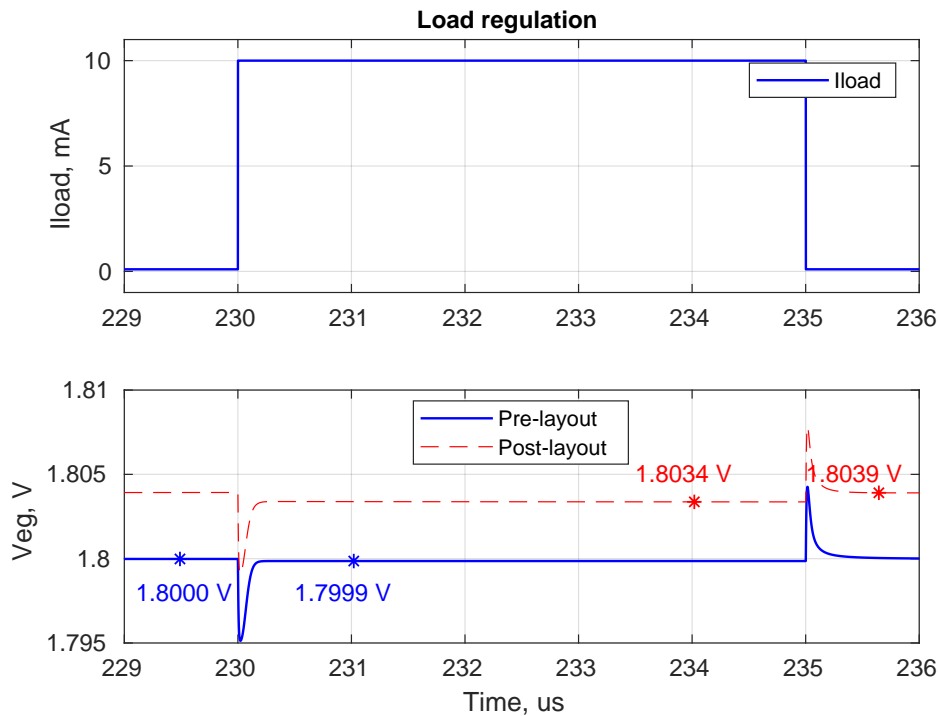


Figure 4.5: LDO step load regulation

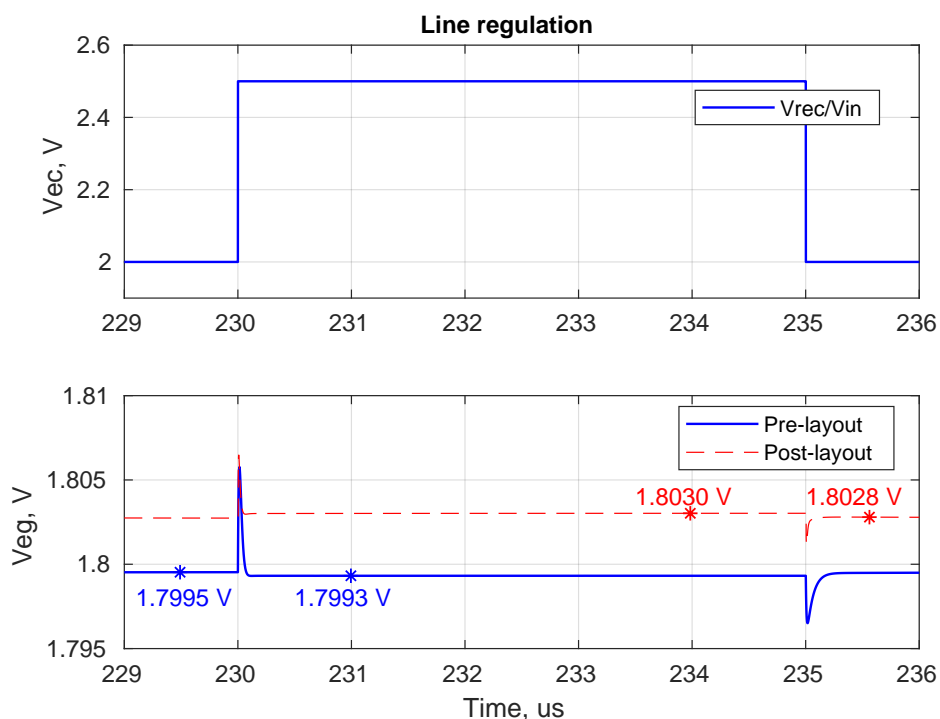


Figure 4.6: LDO step line regulation

4.3.2 DC response

Figure 4.7 and 4.8 show LDO response to input voltage, V_{rec} sweep and output load, I_{load} sweep. As seen in 4.7, the regulator is turned off for input below 1.85 V. Since the input is also the supply for the entire design, higher voltage is required for creating proper biasing of internal folded cascode error amplifier. However after turning on, it requires only 100 mV drop for proper regulation for maximum load and is even lesser for lighter load. This shows that minimum value of supply required for LDO to function properly is 1.95 V. In 4.8, it is seen that regulated output voltage for post layout simulation is 3.7 mV higher than for schematic. Since $V_{reg} = (1 + R_1/R_2) * V_{ref}$, the mismatch in the resistors has resulted in slightly higher ratio, consequently increasing the close loop gain.

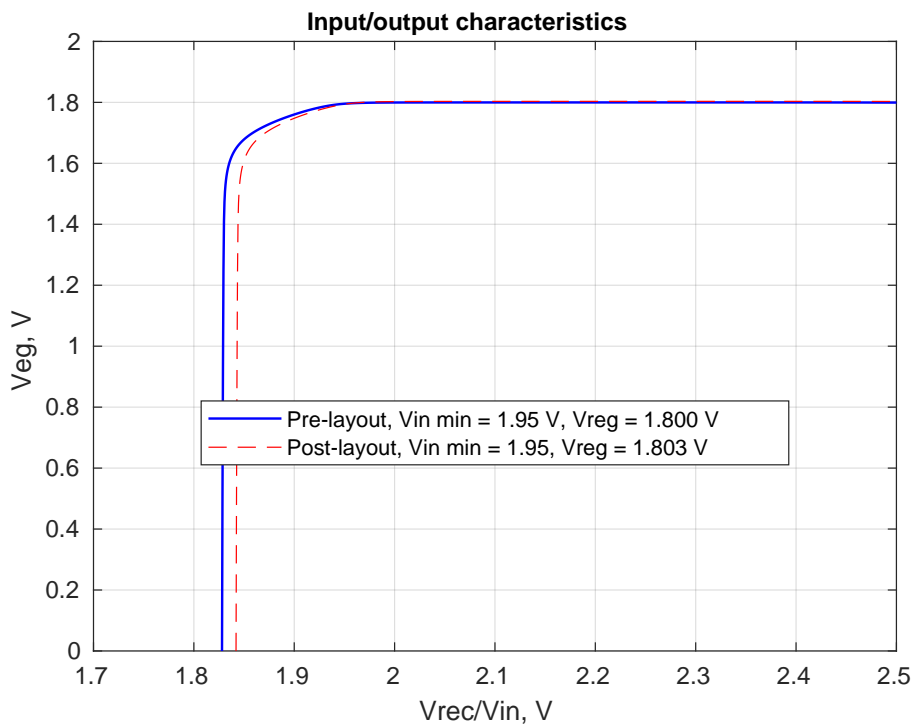


Figure 4.7: Regulated voltage with supply variation

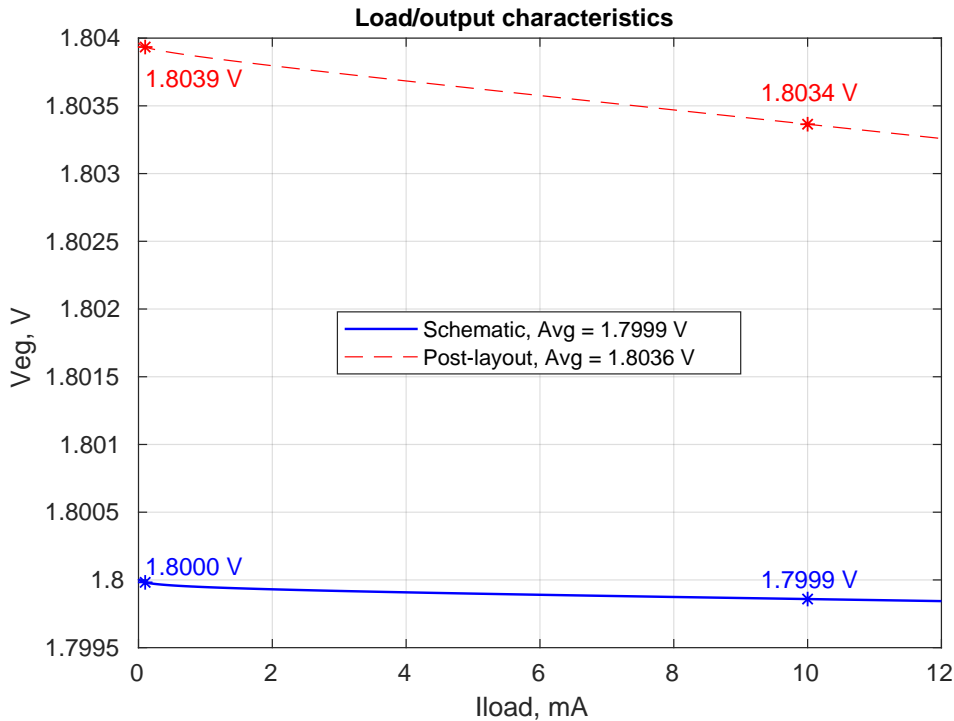


Figure 4.8: Regulated voltage with load variation

4.3.3 AC response

Figure 4.9 is open loop gain and phase margin of LDO without and with compensation. In the upper uncompensated bode plot, two poles below UGF are seen: the first one at 300 KHz due to output resistance of pass device and its parasitic capacitance, and the second one at 60 MHz due to buffer output resistance and gate capacitance of pass device. UGF is at 100 MHz. Due to these two poles both occurring below UGF, the PM fallen to -45°. For making the LDO stable, as discussed in the beginning, a capacitor, C_{load} , 2.5 uF with specific series equivalent resistance, R_{esr} , 0.8 Ω is used at the output. C_{load} and pass device output resistance creates the dominant pole at 1 KHz and R_{esr} and C_{load} creates a left half plane zero below UGF which cancels the non dominant pole. This eventually gives 75°PM and 30 dB GM.

Likewise figure 4.10 is the plot showing PSSR of this LDO. It can be seen that it has poor PSSR performance for frequency higher than 200 KHz. Low frequency noise like 50Hz supply ripple is effectively rejec-

ted. In this design 13.56 MHz ripple and its first harmonics is expected in the input of LDO because rectified output from rectifier operating at 13.56 MHz as input signal is used as supply and/or input for this LDO. Unfortunately, PSSR performance is worst around this frequencies. However the ripple rejection is still -36 dB at 13.56 MHz which is decent. As seen in figure 4.9, the open loop gain of LDO feedback circuit is 90 dB, which has contributed in achieving decent PSSR even at higher frequency[26]. This paper also discusses that UGF frequency corresponds to the roll off frequency of PSSR, which can also been seen by comparing plots 4.9 and 4.10. The stability technique in this design also gives adverse effect on PSSR performance as UGF is significantly lowered by large output capacitor.

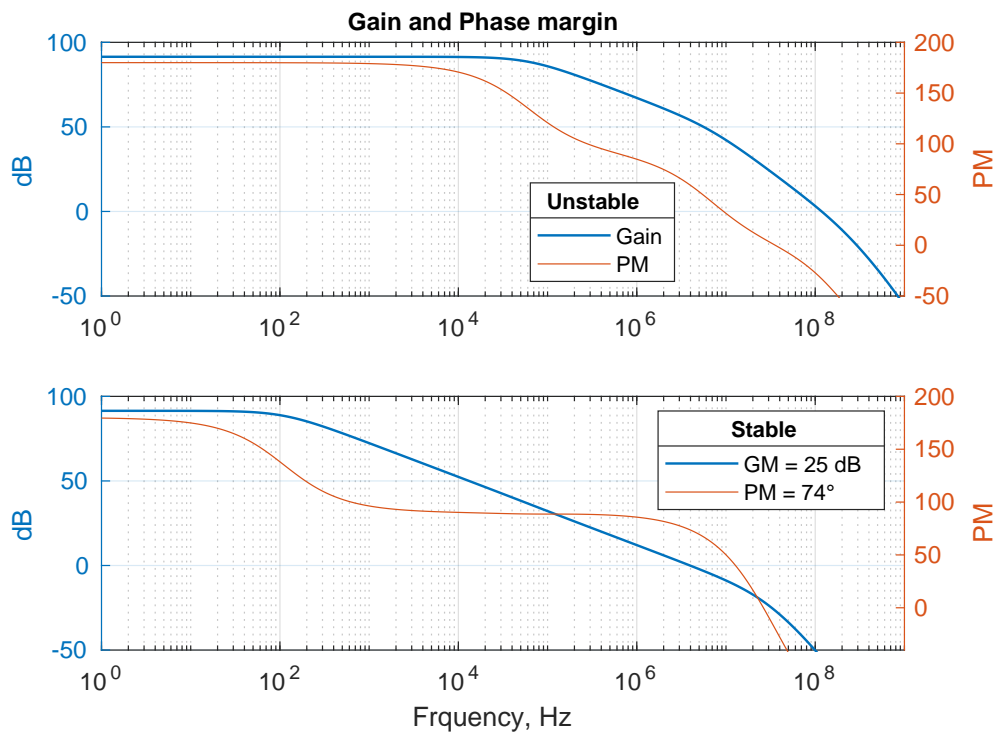


Figure 4.9: LDO stability before and after compensation

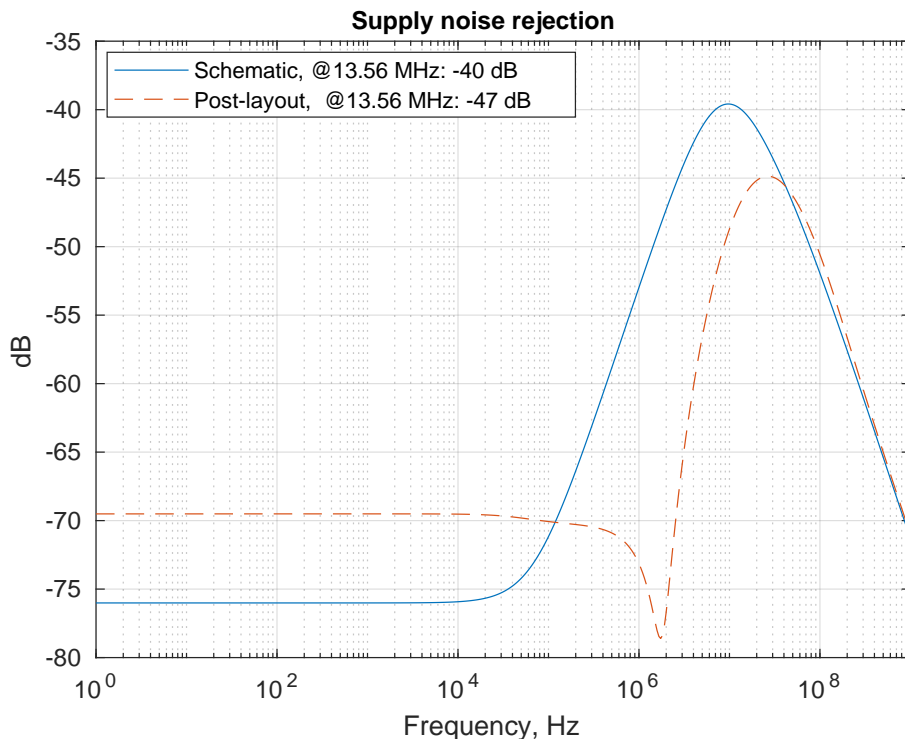


Figure 4.10: PSSR performance

Table 4.2 summarizes the performance of LDO regulator discussed above. Power efficiency is calculated as power delivered to load to power consumed from the source. Quiescent current includes biasing currents for error amplifier, feedback resistors and buffer which is obtained by taking the difference of current drawn from the source and current delivered to the load. Both power efficiency and quiescent current is calculated for maximum load operation.

Low Dropout Regulator

Table 4.2: LDO performance summary

	Schematic	Post-layout
PSSR	-36 dB @ 13.56 MHz	-59 dB @ 13.56 MH
Phase margin	75°	
Gain margin	30 dB	
Power efficiency	80.9 %	81 %
Quiescent current	105 uA	114 uA
Load regulation	17 uV/mA	53 uV/mA
Line regulation	435 uV/V	-1.162 mV/V

Chapter 5

Antenna Design

5.1 Introduction

All the components discussed above are part of any power management system which takes DC input from power line and creates regulated output as required. However, the objective here is to replace direct power line connection with wireless link. Since the intention is to just create a wireless power transfer link, the option which is easier to implement, convenient to operate and gives higher transfer efficiency is the primary choice here. And the literatures in wireless power transfer studies show inductive coupling meets all these requirement.

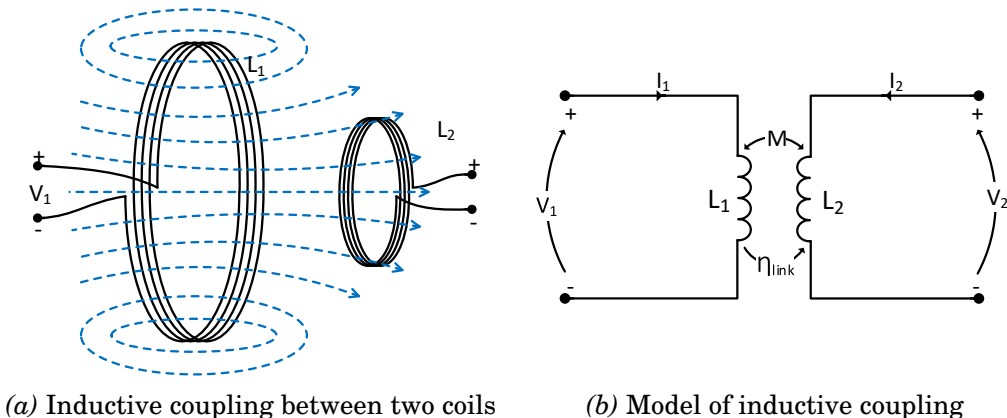


Figure 5.1: Inductive coupling

Inductive coupling boils down to principle of electromagnetic induction as first discovered by Faraday, shown in figure 5.1 . When alter-

ating electric current, I_1 is passed through a coil, say primary, L_1 , it generates changing magnetic flux, Φ . If another coil, say secondary, L_2 is placed in this changing magnetic flux region, alternating voltage, V_2 is induced across L_2 as given by equation 5.1. M is mutual inductance between the coils and k is coupling coefficient which is the ratio of magnetic flux crossing L_2 to total magnetic flux generated by L_1 , which depends in shape, size, separation and orientation of the two coils.

$$V_2 = M \frac{dI_2}{dt} \quad (5.1)$$

$$M = k \sqrt{L_1 L_2} \quad (5.2)$$

In other word, power from primary coil is transferred wirelessly to secondary coil through magnetic field and this is popularly known as inductive power transfer. And this induced ac voltage is rectified and then used to power up the load. The maximum power transfer efficiency across the inductive link for optimal load, η_{link} is given as [27]

$$\eta_{link} = \frac{k^2 Q_{L_1} Q_L}{1 + k^2 Q_{L_1} Q_L} \cdot \frac{Q_L}{Q_{L_2} Q_L} \quad (5.3)$$

Here k is coupling coefficient, Q_{L_1} and Q_{L_2} are quality factor for respective coils and Q_L is quality factor of loaded secondary coil. This shows that transfer efficiency increases with increase in coupling and quality factor. However for any practical design, it is impossible to get higher efficiency because of poor coupling between the coils. For such poorly coupled linked, leakage inductance given as $L_2(1 - k^2)$, is much greater than mutual inductance[28] which causes more wastage of magnetic flux. This leakage inductance can be cancelled by adding capacitor and creating resonance at the operating frequency. This method of creating better wireless energy transfer link is popularly known as magnetic resonance coupling.

In this project, first an antenna coil is designed and characterised. Then inductive link created using the antenna and finally magnetic resonance technique is implemented to increase transfer efficiency at the operating frequency. The antenna dimensions are provided by Nordic Semiconductor. Since having similar shape and size of antennas is important in gaining more transfer efficiency, the same antenna type is used as both primary and secondary coils.

5.2 Inductor Model

Figure 5.2 is a lumped model of a planar antenna/coil/inductor made on a PCB. R_p , series DC resistance of wire and C_p , inter-winding self capacitance. These parasitics determine quality factor, Q and self resonance frequency, SRF of the antenna as given in equations 5.4 and 5.5.

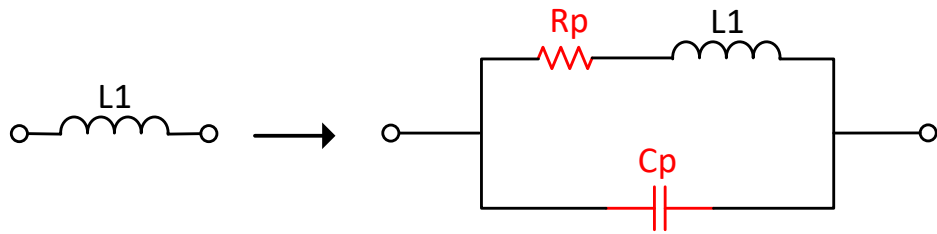


Figure 5.2: Real antenna model

$$Q = \frac{\omega L}{R_p} \quad (5.4)$$

$$SRF = \frac{1}{2\pi\sqrt{LC_p}} \quad (5.5)$$

For purpose of this work, with provided dimensions of the antenna, it is first modelled in HFSS as shown in figure 5.3a and its equivalent lumped circuit in figure 5.3b. It is important to note here that L_1 in 5.3b is as in 5.2. However, in the discussion ahead, these parasitics are not explicitly mentioned for the sake of simplicity because the parameter extraction will include these factors too and on the other hand the operating frequency here is much less than coil SRF. To realise a real antenna, physical parameters of materials used for making printed antenna on a PCB are also given for the model. After completing model, frequency sweep is done for extracting S parameter of the antenna which was eventually used to estimate self inductance of the modelled coil. The performance estimation of single antenna here and couple system later is based on formulas in [29]. In order to check

and compare the estimated inductance value from the model, Modified Wheeler Formula, a mathematical approximation model described in [30] is used. The qualities of antenna obtained from extracted S-parameter are listed in table 5.1. The table shows that modelled inductance value is less than mathematically approximated value. This difference can be explained with two things. Firstly, mathematical calculation assumed that the antenna is spiral and rectangular with sharp edge but the model has rounded edge. Secondly, during modelling besides dimensions of the coils, physical parameters of coil materials are also used but these are not considered for mathematical calculation.

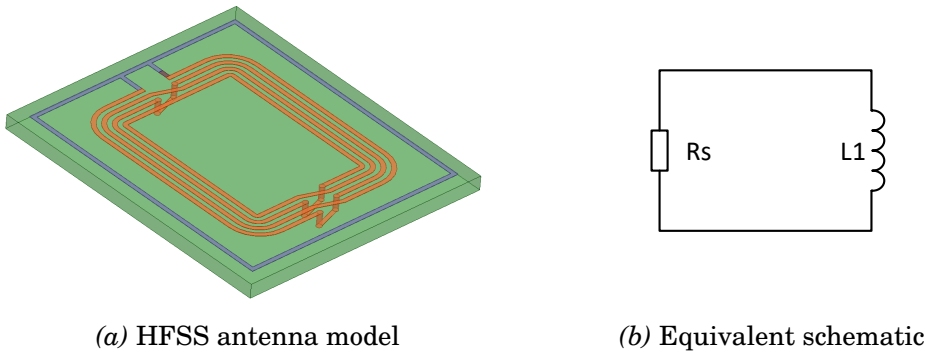


Figure 5.3: Antenna model

Table 5.1: Characterisation of antenna

	HFSS model	Modified Wheeler [30]
Self Inductance, L_1	509 nH	644 nH
SRF	125.65 MHz	-
Parasitic Resistance, R_p	0.66 Ω	-
Parasitic Capacitance, C_p	3.2 pF	-

5.3 Inductive Transfer Link

In the next step, an inductive link is realised by using two antennas: one as primary and other as secondary, aligned one over other and separated by air gap as shown in figure 5.4a, equivalently shown as lumped schematic in figure 5.4b. Coupling system of these antennas is simulated for varying distance of magnetic field interaction to observe the difference in performance. The same procedure as used for single coil above, is used to extract self inductance of each coil, L_1 and L_2 , mutual inductance of two coils, $L_{12} = L_{21} = M$, coupling coefficient between the coils, k and quality factor, Q . The extracted values for coil separation of 1mm, 5mm and 10mm are listed in table 5.2 calculated at operating frequency of 13.56 MHz.

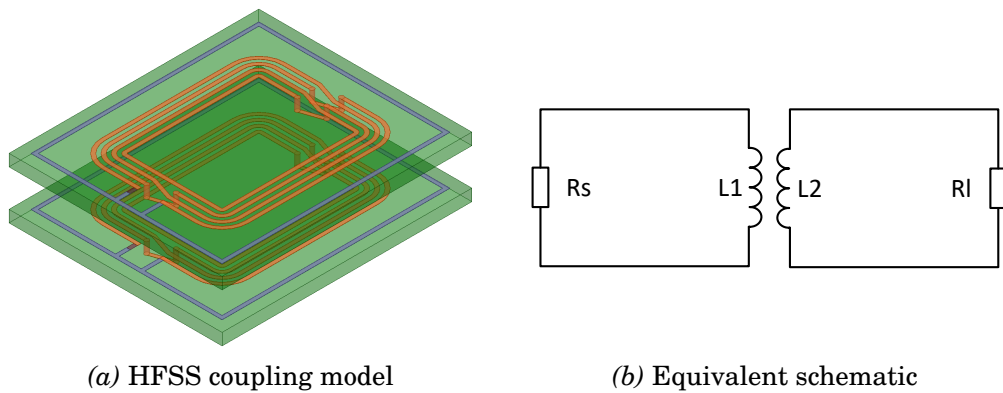


Figure 5.4: Antenna coupling model

Table 5.2: Coupling parameters for varying coils distance

	Sepr: 2 mm	Sepr: 5 mm	Sepr: 10 mm	Unit
L_1^*	357	481	501	nH
L_2^*	353	476	496	nH
M	254	122	50	nH
k	0.52	0.25	0.10	-
Q_{L_1}	39-60	57-63	62	-
Q_{L_2}	40-64	61-67	67	-

In table 5.2, L_1^* and L_2^* are leakage inductance of primary and

secondary coil when they are mutually coupled. Similarly M and k , which are related as in equation 5.2, are both decreasing with distance as expected because with increase in separation between the antenna, less and less magnetic flux generated by primary coil is linked with the secondary, creating a loosely coupled inductive link.

As already stated, power transfer efficiency depends on k of coupling system and Q 's of coils and hence high k and high Q is always desirable and obviously coil optimisation is the most important part of coupling system design. [31] and [27] discusses some techniques to optimise transfer efficiency of inductive link: [31] about matching the load for better resonance whereas [27] about designing optimal coil geometry for higher Q . The former one compares the efficiency of general inductive coupling and conventional resonant coupling and their limitation in achieving higher efficiency. This eventually proposes optimal resonant load transformation which has better immunity to poor coupling and load variation. Likewise, the later one describes step by step iterative process of designing an antenna with optimal geometry for the given design constraints.

5.4 Magnetic Resonance Coupling

In this project, conventional magnetic resonance coupling as in is implemented to tune both primary and secondary at same frequency. The purpose here is to tune the secondary antenna of coupling system to the operating frequency to cancel the leakage inductance and increase quality factor, and tune the primary antenna to the same frequency to increase the driving current. Thus creating resonance in an inductive link maximise the power transmission from the source to the load.

For the purpose of making a resonant inductive link, the S parameter of coupled antenna system in HFSS is exported to ADS in order to design tuning networks using capacitors. Impedance of primary antenna is matched to $R_s (= 50\Omega)$ source resistance and impedance of secondary is matched to load impedance, R_L as shown in 5.5. Here R_L represent ac load combined of rectifier, LDO and electronic device as dc load. This ac load is approximated to 115Ω as in [28]. C_{p1} , series capacitor and C_{p2} , shunt capacitor together with L_1 created parallel resonant circuit at 13.56 MHz on the primary side and C_{s1} , shunt ca-

pacitor together with L_2 creates the secondary resonant circuit at same operating frequency. Parallel secondary tuning with C_{s1} is chosen as this is recommended when $X_{L_2} < R_L$ and so it is in this work. Similarly in primary side both, first series C_{p1} and then parallel C_{p2} , is chosen in order to cancel both real and imaginary of primary impedance[32]. Thus a pair of LC tank circuit is made tuned at same frequency. Such matching network is designed for all three coil separation distances as above, but resonant coupling system with 5 mm separation is taken as a typical example and presented here.

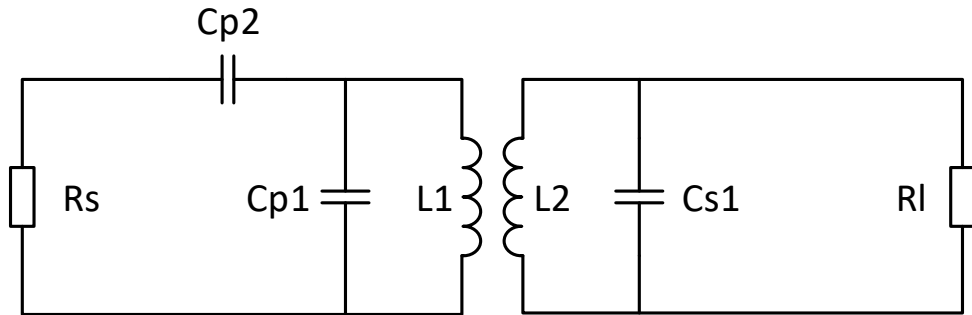


Figure 5.5: Resonant coupled inductive link

In figure 5.6, reflection power losses: return loss, S_{11} at primary antenna terminals and reverse return loss, S_{22} at secondary antenna are presented comparatively before and after tuning. This shows that the reflection losses have been significantly reduced, at least by 25 dB, due to magnetic resonance created at the operating frequency.

Likewise, in figure 5.7, power transfer gain, S_{21} , from primary to secondary antenna is shown. It can be seen that power transfer has been improved by 13 dB at the resonant frequency. The power transfer efficiency, η_{link} in given equation 5.3 is obtained empirically from S_{21} as follows.

$$\eta_{link} = \eta_{pri} * \eta_{sec} = |S_{21}|^2 \quad (5.6)$$

The above η_{link} calculation is valid for perfectly matched ports and gives maximum possible power gain from primary to secondary antenna.

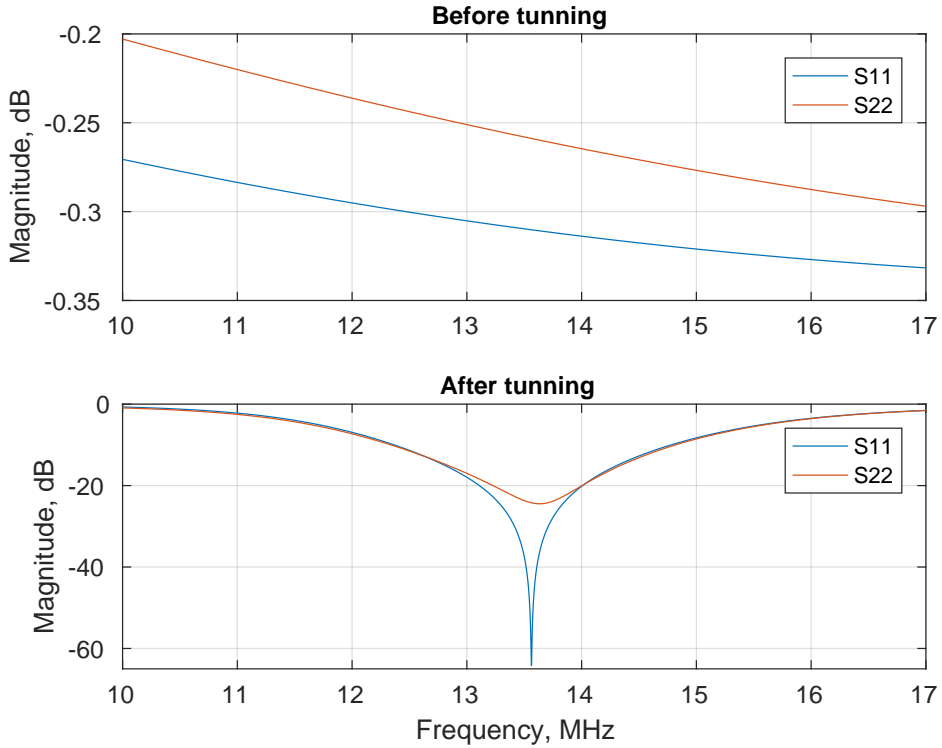


Figure 5.6: Link reflection loss before and after tuning

The above discussion is also done for other two separation, 1.5 mm and 10 mm, of coupling coils. The performance of magnetic resonant inductive link for all cases designed in this work is summarised in table 5.3.

Table 5.3: Performance of resonant inductive link

	Sepr: 1.5 mm	Sepr: 5 mm	Sepr: 10 mm	Unit
C_{P1} ,	660	126	51	pF
C_{P2}	80	190	227	pF
C_{S1}	288	288	288	pF
ω	13.56	13.56	13.56	MHz
$S11$	-55	-61	-29	dB
$S22$	-30	-24	-9	dB
$S21$	-0.28 (0.97)	-0.61 (0.93)	-2.50 (0.75)	dB (mag.)
η_{link}	94	86	56	%

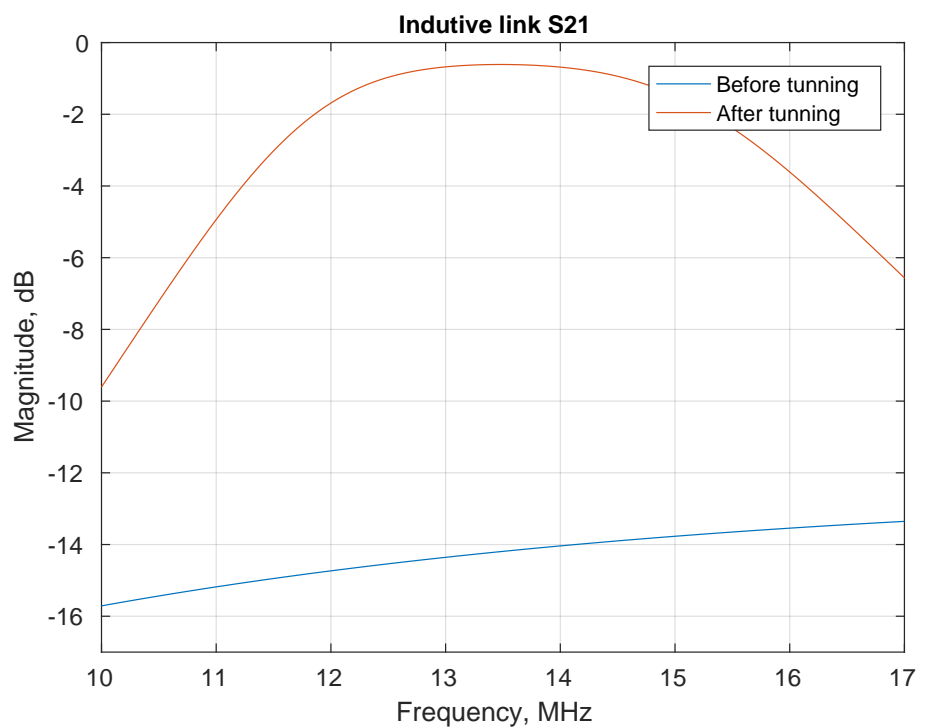


Figure 5.7: Link gain before and after tuning

Part III

WPT System Design and Implementation

Chapter 6

PMS and WPT Systems

6.1 Introduction

Wireless power transfer, WPT system always constitutes two main units: power transmitting unit, PTU and power receiving unit, PRU. Each unit comprises of resonator, power conditioner and control circuits as shown in figure 6.1. Both the resonators in PRU and PTU are tuned to operating frequency, which create a physical transfer link. Power conditioner circuit in PTU includes at least power amplifier and matching circuit, whereas in PRU, it includes matching circuit, rectifier and regulator. Similarly both these units have control block which facilitates transfer procedure and communication between these units. In this work, design and analysis of PRU is the main objective.

In figure 6.1 above, the block highlighted in blue is the PRU system in this design. Secondary coil, Rx is the receiver resonator, and rectifier and regulator is power conditioning block. The primary coil is driven by a power source and AC signal is generated at the secondary as discussed earlier in antenna design section. The rectifier then rectifies this AC signal to DC. The DC output of the rectifier is then fed to LDO to produce regulated DC output required to drive a load. The reference and biasing circuit generates required reference and biasing DC voltages for the LDO.

The PRU unit is broken down into two sub units for step wise analysis. As seen in the block diagram, it is functionally divided into Transfer Link and Power Management System (PMS). Firstly, PMS is simulated excluding the transfer link to characterise the perform-

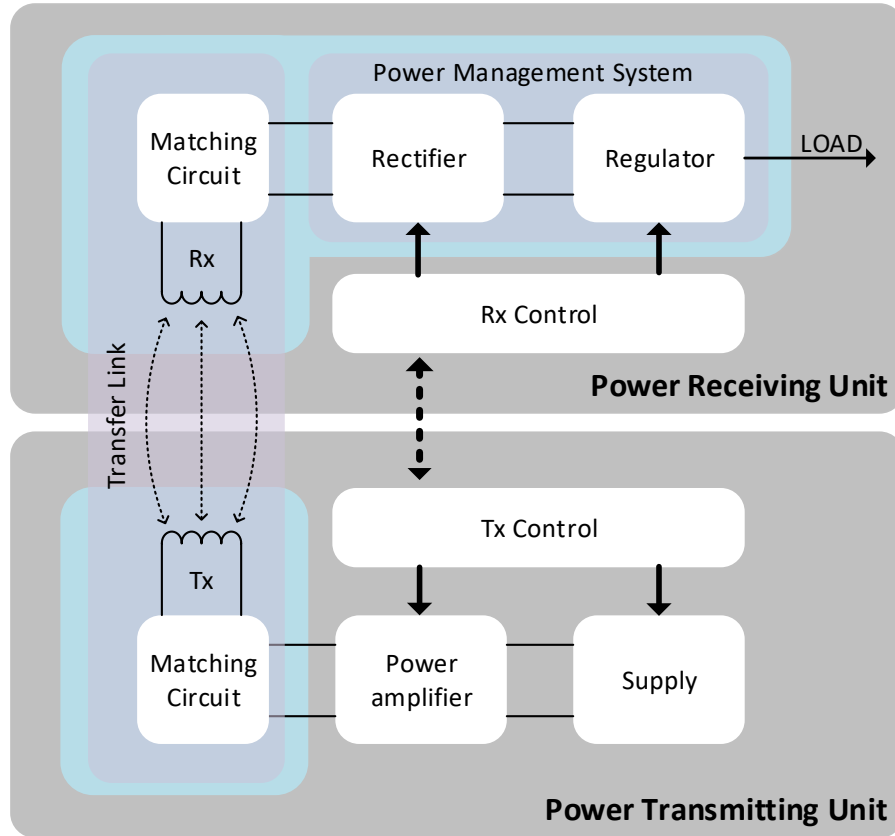


Figure 6.1: WPT block diagram

ance of PMS. Secondly, the whole PRU system: PMS with transfer link created with coupled antenna, Tx and Rx, is simulated to observe the performance of whole PRU. Though it has already been told earlier, one important thing must be mentioned here again before going further. Even though reference and biasing circuit has been integrated into the PMS system, it has been designed with an option to override it externally. This externally supplied reference and biasing will be primarily used for the PRU system simulation. The result with on-system biases and reference will be explicitly noted when used.

6.2 Power Management System

Figure 6.2 is the top level of PMS in this design and test bench setup is shown in figure 6.3. The purpose here is to give differential signal

PMS and WPT Systems

V_{in1} and V_{in2} to PMS system and see V_{rec} and V_{reg} outputs while driving load. The voltage signal from source V_{ac} is fed to balun in order to generated V_{in1} and V_{in2} . The other inputs are external biases, reference, control and supply for LDO and buffer. Other outputs are bias voltages to examine the performance of BGR circuit which can be disabled with external control signal V_{ctl} low.

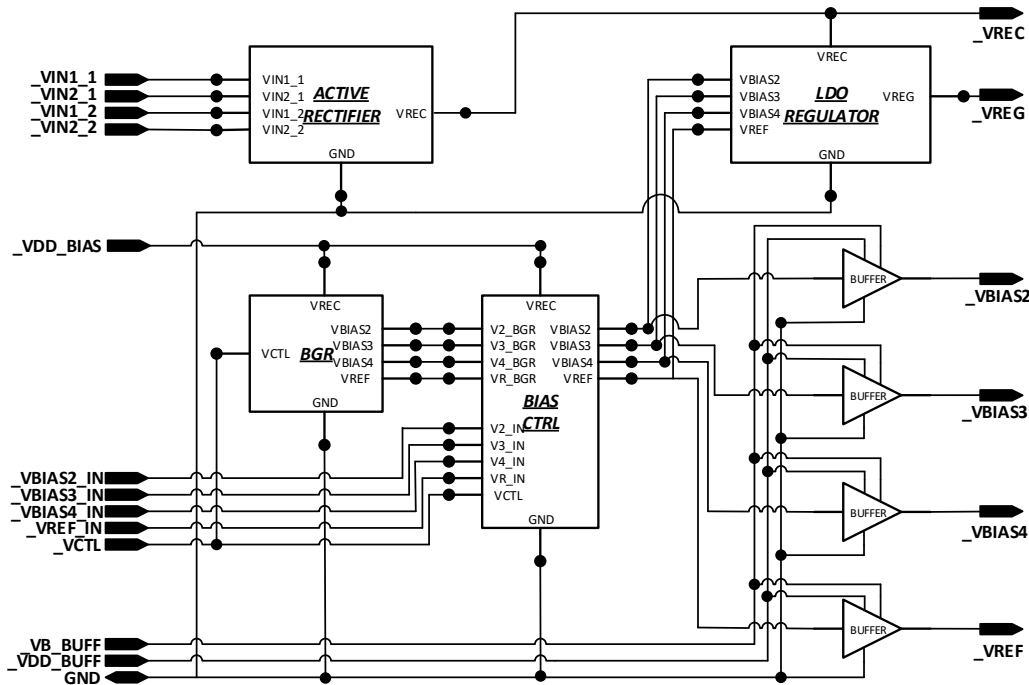


Figure 6.2: WPT PMS implementation

PMS and WPT Systems

Table 6.1: PMS test-bench stimuli voltages and components

V_{in}	2.6 V _p
Operating frequency	13.56 MHz
V_{ac}	> 100 nF
V_{bias2}, V_{bias3} & V_{bias4}	1.1, 0.88 & 0.68 V
C_{load} & R_{esr}	> 2.5 μ F & > 0.5 Ω
$I_{load} = I_{max}$	10 mA
$V_{dd_{buff}}$ & $V_{dd_{bias}}$	2.5 & 2.2 V
$V_{b_{buff}}$	1.4 V
V_{cntl}	0 V for external biases 2.5 V for internal biases

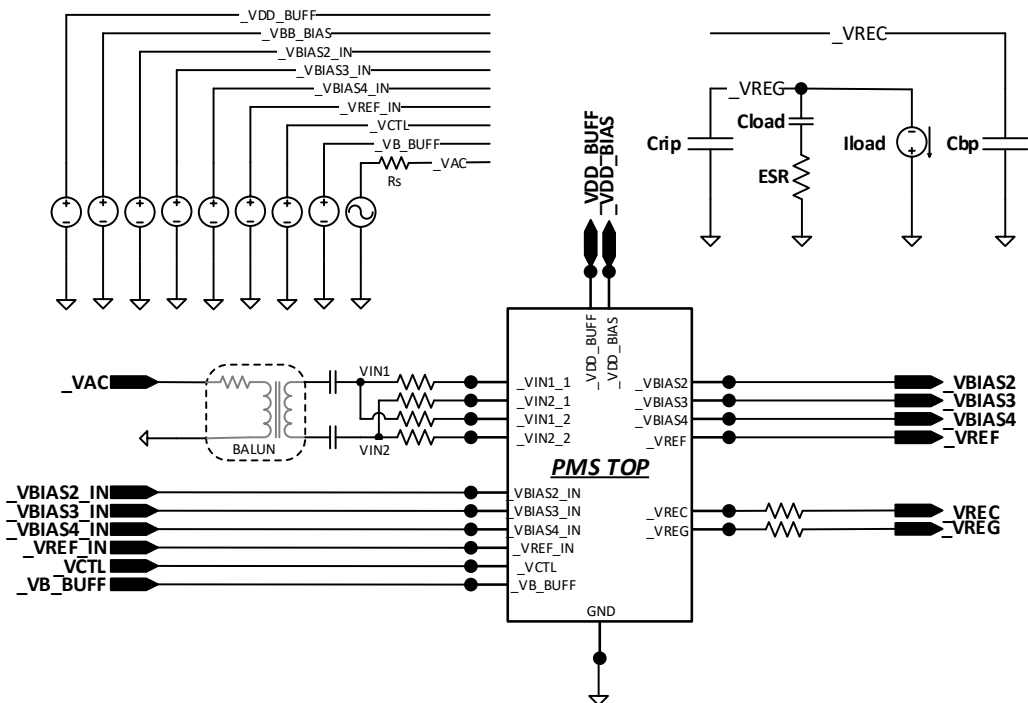


Figure 6.3: Test bench for PMS simulation

In the test-bench in figure 6.3, stimuli voltages like input and biases and components like capacitors and resistors are used. The values for these stimuli and components are listed in table 6.1. V_{ac} is set to 2.6 V in order to compensate voltage drop of pad resistance.

6.2.1 Simulation result

Figure 6.4 and 6.5 shows input and output waveforms of PMS block when supplying 10 mA current to the load. On comparing V_{rec} with that of rectifier only section, two distinct difference can be observed: additional drop in V_{rec} and additional time to get maximum V_{rec} . As already mentioned that final parasitic extraction from layout not just include the core but also the tracks from pad to the core inputs, which obviously contributes more resistance in the conduction path and hence more drop in V_{rec} . Similarly, passive and active rectification region is clearly seen here. C_{load} being a large capacitor, it is taking longer time to start the active rectification. The regulated output, V_{reg} is similar to as discussed in LDO section.

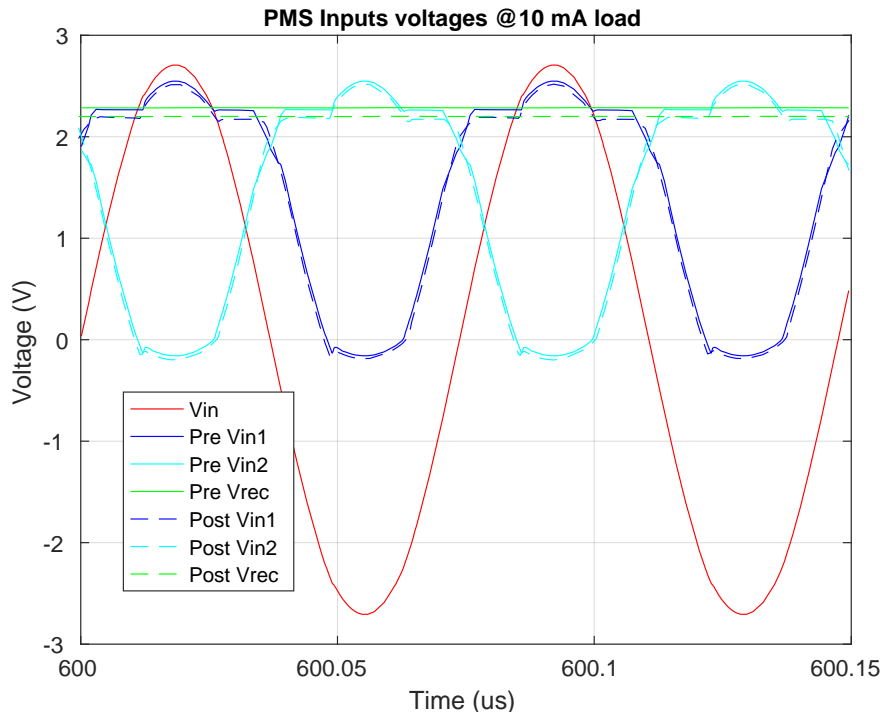


Figure 6.4: Input voltage waveform of PMS

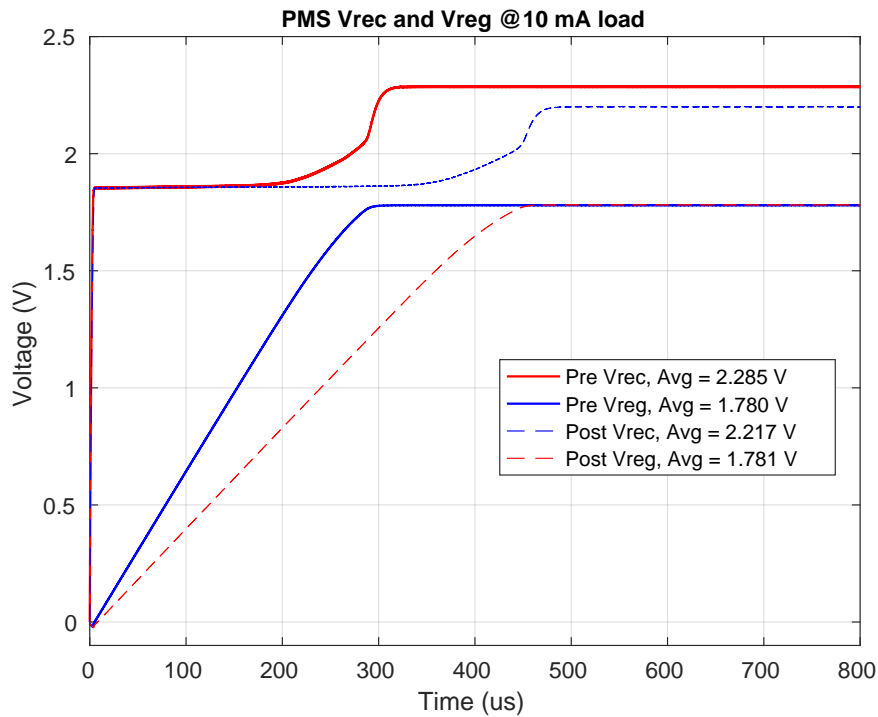


Figure 6.5: V_{rec} and V_{reg} voltages of PMS

Figure 6.6 gives a zoomed view of rectified, V_{rec} and regulated, V_{reg} output voltages. Their characteristics are same as discussed in rectifier and LDO section.

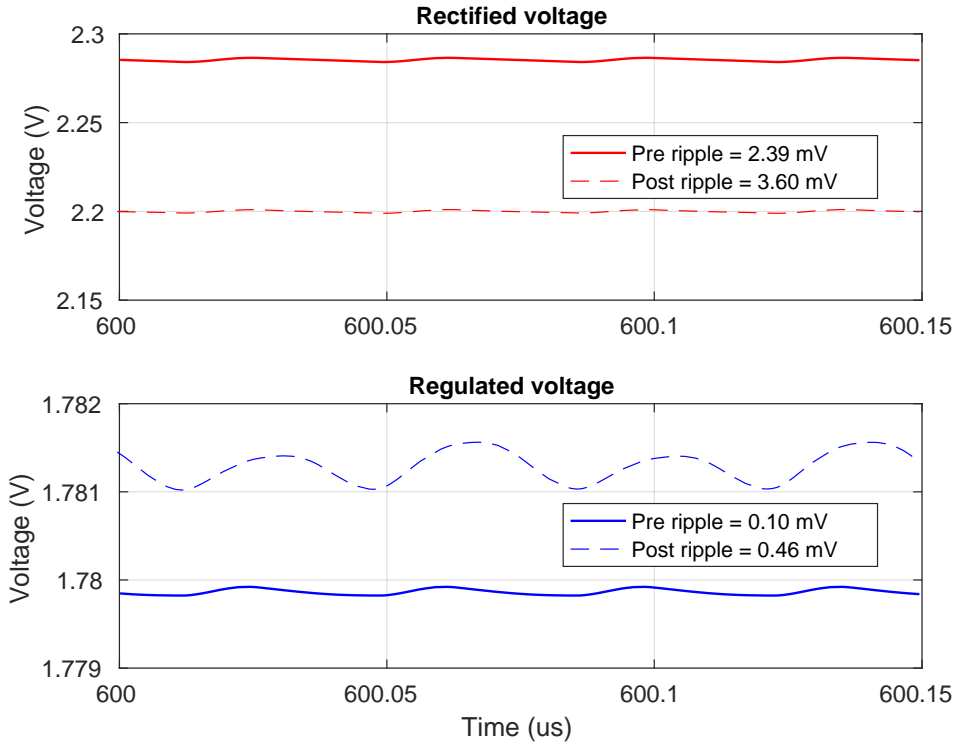


Figure 6.6: Ripple in V_{rec} and V_{reg}

Figure 6.7 shows diode currents corresponding to its input voltages. It is seen that diodes turn off slightly later than intended. This has resulted in reverse leakage of current. Since rectifying diodes are realised with large MOSes, these diodes have larger gate to source capacitance. So when the diodes are turned on and off, it requires some time to charge and discharge, resulting in delay of turning off diodes. The other reason might be, if the parasitic capacitance of diodes are not equal, it results in different charging and discharging of time of diodes, resulting in even conduction of current through them. Same is the reason for rms diode current being slightly less in post layout. The other important observation is peak diode though V_{in1} path is less than through V_{in2} path which means paths from pad to diode inputs are asymmetrical with V_{in1} track having higher resistance.

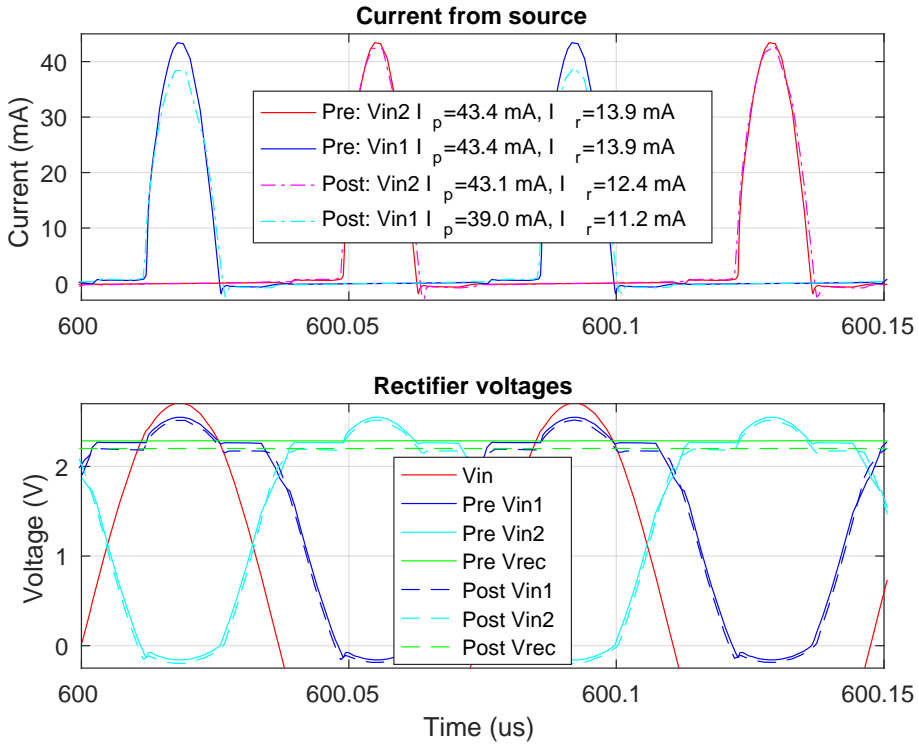


Figure 6.7: Current and power consumption

The total power consumed from signal source, V_{ac} are 30.2 mW and 28.4 mW for pre and post layout simulation for delivering 17.8 mW to the load. Slightly less power is consumed in post layout which is explained by two things: reduced rms current of diodes as explained earlier and reduced V_{rec} . Since V_{rec} is the input to the LDO, less V_{rec} means pass device in LDO has to drop less voltage increasing LDO efficiency.

This results in power transfer efficiency, η_{pms} of 58.9 % and 62.7 % respectively. In theory these values should be equal to

$$\eta_{pms} = \eta_{rect} * \eta_{ldo} \quad (6.1)$$

Using η_{rect} from table 3.2 and η_{ldo} from table 4.2, the pre and post layout efficiencies are 68.5 % and 67.2 % respectively. This disagreement in value is due to inclusion of pad resistance and pad to core resistance in top test bench of PMS.

The performance of PMS system is tabulated as in table 6.2.

Table 6.2: PMS performance summary

	Schematic	Post-layout
V_{rec}	2.285 V	2.217 V
ΔV_{rec}	2.4 mV _{pp}	3.6 mV _{pp}
V_{reg}	1.780 V	1.781 V
ΔV_{reg}	0.1 mV _{pp}	0.5 mV _{pp}
η_{pms}	58.9 %	62.7 %

6.3 WPT System

6.3.1 Top Testbench

Figure 6.3 is also the test bench for complete WPT PRU unit when the balun block is replaced with wireless transfer link model. Figure 6.8 is the transfer link realised with lumped model of resonant inductive link. The values of lumped elements of inductive link and tuning capacitors are given in table 5.1, 5.2 and 5.3. V_{ac} , a 13.56 MHz voltage source, is connected to V_{pri} input of this model and differential voltages V_{sec+} and V_{sec-} are generated as output, which are used as V_{in1} and V_{in2} inputs for PMS system. The simulation result of 5 mm distance coupling is presented below.

Since the nominal peak to peak value of differential inputs is 2.6V, during simulation magnitude of V_{ac} is gradually increased till the differential signals in secondary antenna reach the nominal value when driving maximum load. Other biasing voltages and component values remain the same as in PMS simulation test bench given in table 6.1.

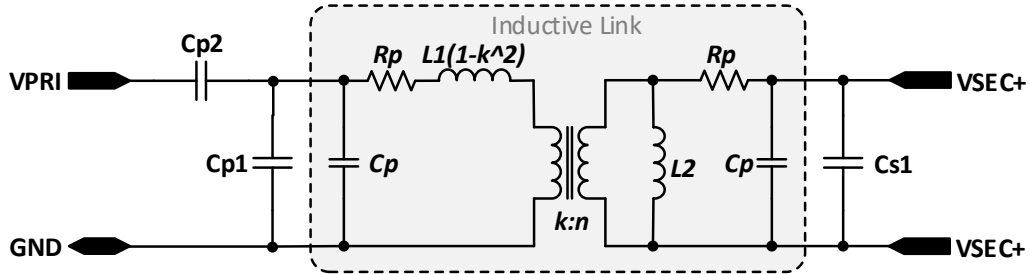


Figure 6.8: Lumped model of inductive link

The parasitic extraction of the complete layout also includes the tracks from pad to core inputs. The pad-frame layout provided by the fab was used to accurately draw the tracks from pad to core I/O terminals.

6.3.2 Simulation result

Figure 6.9 is the plot presenting input voltages to the inductive link and chip: V_{ac} is input to the primary antenna, and V_{in1} and V_{in2} are differential voltages generated across the secondary antenna which are inputs to the chip and V_{in} is $V_{in1} - V_{in2}$. In order to obtain the nominal amplitude of 2.6 V of the differential signals, the amplitude of V_{ac} is required to rise to 3.7 V. It is seen that V_{ac} slightly lags in phase with V_{in} due to shift in resonance frequency. This can be due to mismatch in load at secondary because rectifier being non-linear load, it was modelled as an approximate dc load during tuning of inductive link. Moreover, V_{in} is not perfectly symmetrical here. It is slightly flattened at the peaks because of voltage drop in coil and pad resistance while the diodes are conducting.

In figure 6.10, rectified voltage, V_{rec} and regulated voltage, V_{reg} waveform from the PMS chip is shown where its inputs are the differential signals, V_{in1} and V_{in2} , shown in figure 6.9. On comparing these waveforms with that of PMS system, it is seen that outputs take longer time to reach steady state due to weakly coupled inductive and a large output capacitor.

Figure 6.11 is a closer look over steady state V_{rec} and V_{reg} along with inherent ripple in them.

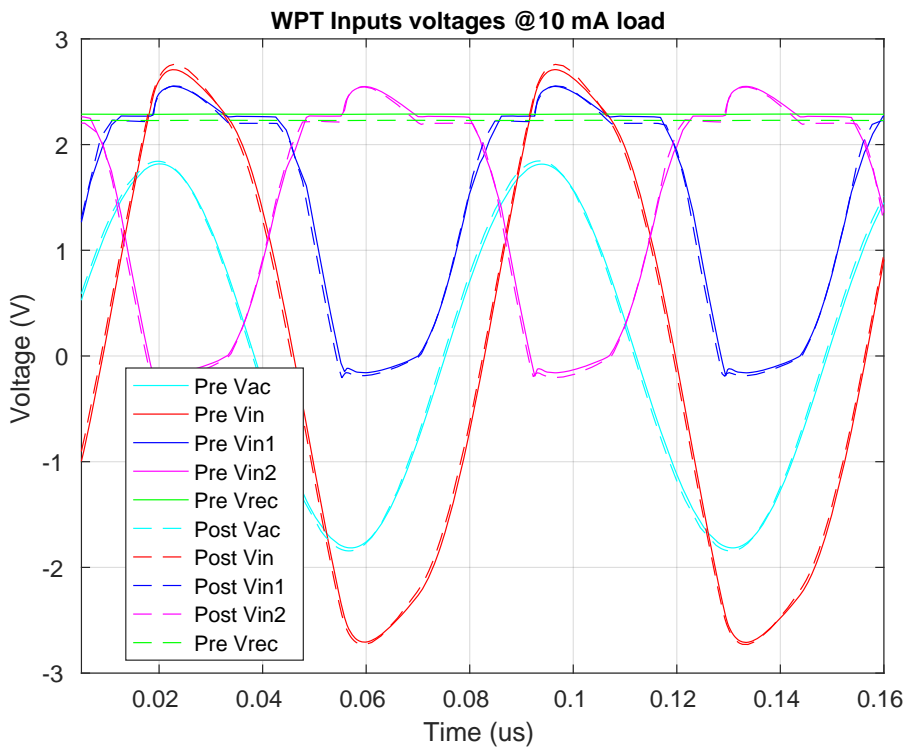


Figure 6.9: Input voltage waveforms

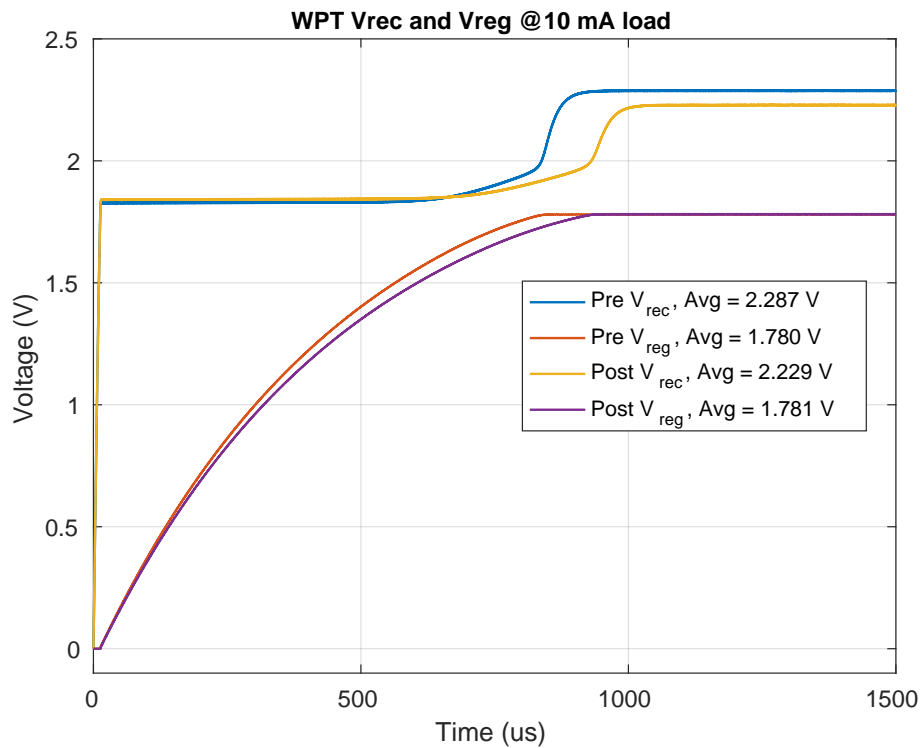


Figure 6.10: V_{rec} and V_{reg} voltages

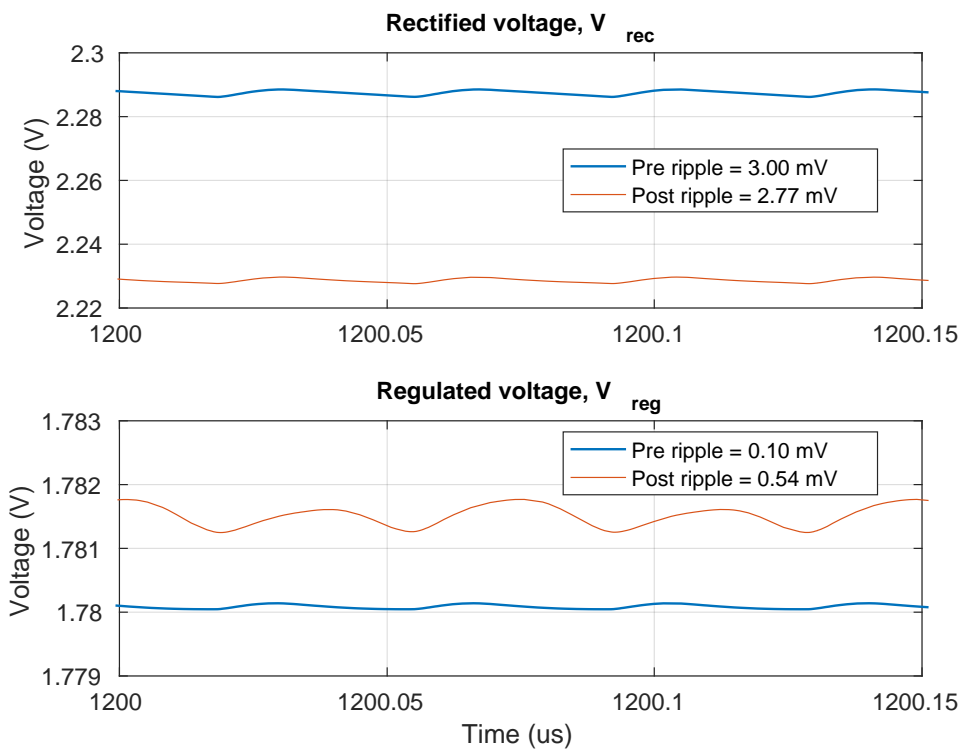


Figure 6.11: Ripple in V_{rec} and V_{reg}

The voltage and current at the primary antenna is shown in figure 6.12. AS already mentioned, V_{ac} is gradually increased to 1.85 V amplitude to get nominal amplitude of differential inputs to the rectifier. Also seen in the plot, current is slightly leading voltage, which means it slightly capacitative and resonance frequency has slight shift.

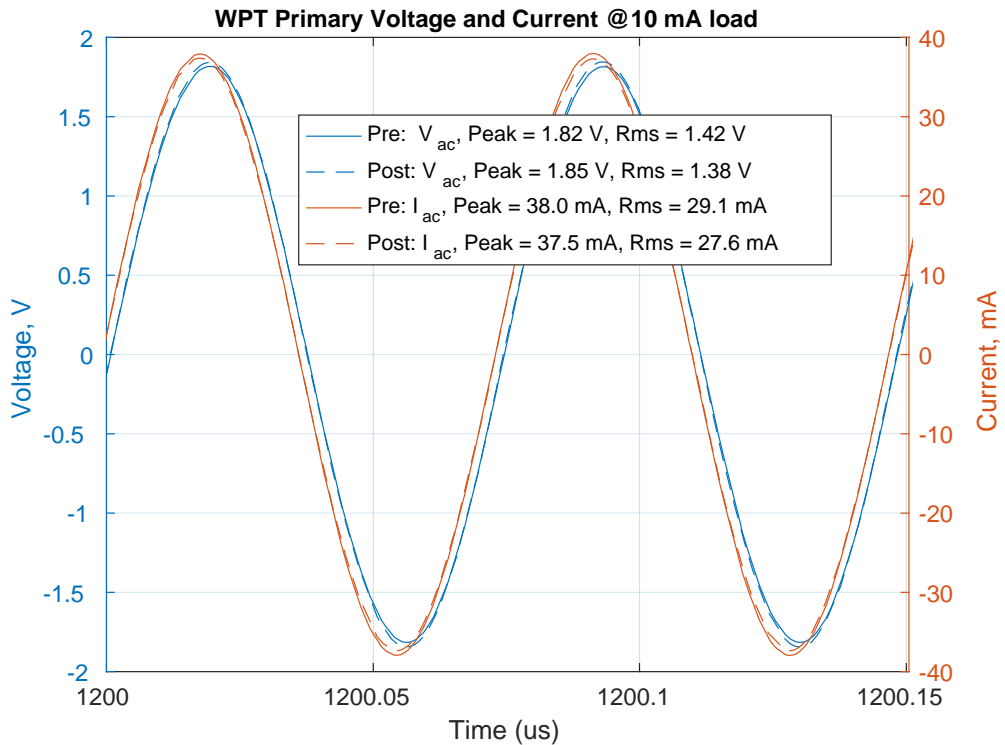


Figure 6.12: Primary voltage and current

Figure 6.13 shows instantaneous diode current waveform with their corresponding input voltages. On comparison with PMS performance, two distinct difference is seen: diode current rising quickly to peak value and higher peak diode current. This is because $V_{in}(V_{in1} - V_{in2})$ changes quickly during turning on time of diodes. That is why the peak of V_{in} is more like a square wave. Similarly as in PMS section, diode in V_{in1} path is conducting less peak current than in V_{in2} path due to two path being resistively asymmetrical in the layout.

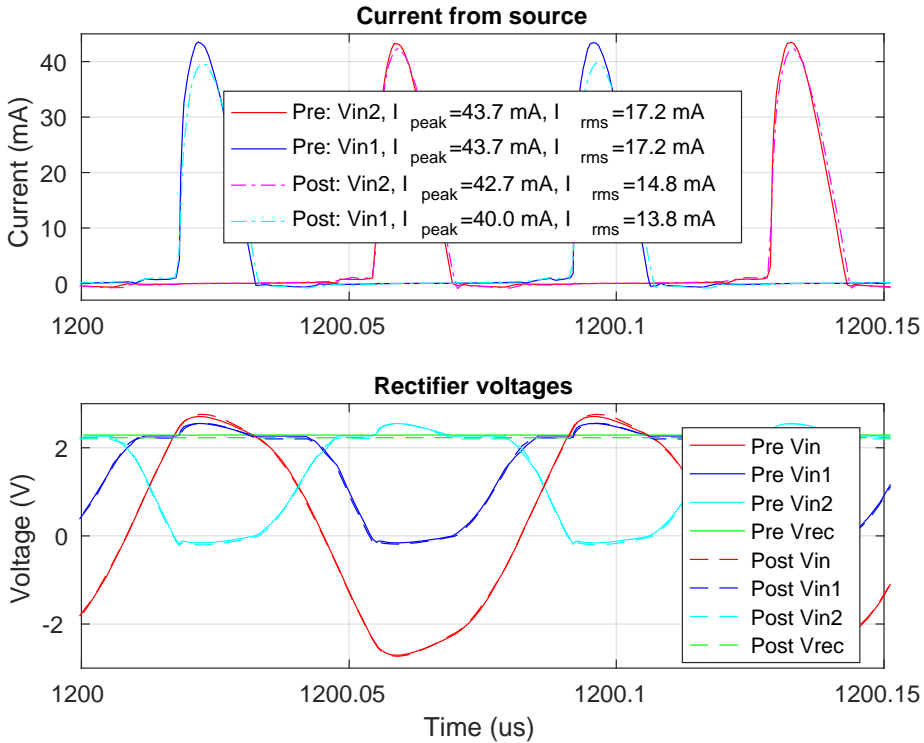


Figure 6.13: Diode current and voltages

From the simulation, it is obtained that primary antenna consumes 37.1 mW and 35.2 mW in pre and post layout result, for delivering 17.81 mW to the load. This results in power transfer efficiency, η_{wpt} , of 48% and 50.6 % respectivley. Using η_{pms} value from table 6.2, η_{link} is obtained 81.5% and 80.7% from pre and post layout result. The theoretical η_{link} for perfectly matched source and load of transfer link is 86%. This difference can be explained with inaccuracy in modelling complete system (PMS chip and DC load) as DC load during tuning of inductive link. As a result this has caused slight shift in resonance frequency and eventually has reduced efficiency.

Just for the cross check, this η_{wpt} of complete WPT system should be equal to

$$\eta_{wpt} = \eta_{link} * \eta_{rect} * \eta_{ldo} \quad (6.2)$$

Using table 5.3, 3.2 and 4.2, efficiencies obtained from equation 6.2 are 56.7% and 57.8% respectively for pre and post layout results. As already discussed this difference can be explained with resistive loss in

PMS system and load mismatch in resonant inductive link.

Finally, the performance of the above discussed WPT system for maximum load and coil separation of 5 mm is tabulated in table 6.3.

Table 6.3: WPT performance summary for 5 mm coupling

	Schematic	Post-layout
V_{ac}	3.7 V	3.7 V
V_{rec}	2.287 V	2.229 V
ΔV_{rec}	3 mV _{pp}	2.8 mV _{pp}
V_{reg}	1.780 V	1.781 V
ΔV_{reg}	0.1 mV _{pp}	0.5 mV _{pp}
η_{wpt}	48 %	50.6 %

The above analysis and characterisation of WPT system is for inductive link with coil separation of 5 mm for delivering 10 mA current at 1.8 V. The same analysis is repeated for other two cases: a stronger inductive link created from 1.5 mm coil separation and a weaker inductive link created from 10 mm coil separation. For doing this, respective lumped model of inductive link is used in top test-bench, figure 6.3, The comparative post layout performance of WPT system for these different inductive links is listed in table 6.4.

Table 6.4: WPT performance summary for all inductive link

	Sep: 1.5 mm	Sep: 5 mm	Sep:10 mm
k	0.52	0.25	0.1
V_{ac}	3.6 V	3.7 V	4.7 V
I_{peak}	41.2 mA	37.5 mA	39.2 mA
P_{in}	32.8 mW	35.2 mW	51 mW
η_{wpt}	54.3 %	50.6 %	34.9 %

From table 6.4, it is observed that with the increase in distance between primary and secondary coils, there is decrease in coupling between the coils in the inductive link, resulting in less magnetic field

PMS and WPT Systems

from the primary coupling into secondary. That is why with increasing distance between the coils, the primary has to be driven with more power to deliver to the load.

Part IV

WPT Chip Production, Test and Verification

Chapter 7

Test and Verification

7.1 Chip and PCB

After post layout simulation of complete PRU system, it was sent for production to TSMC fab in November 2016 and was received in February 2017. The manufactured chip was packaged in 84 I/O pins JLCC package. The full layout is included in appendix. It is designed in 90nm process using 2.5 V devices. This process provides 1P-9M - 1 poly layer and 9 metal layers. However in this design, 1 poly and 8 metal layers is used. Basically every component layout used up-to 4 metal layers. Only the high current paths are made with parallel path of higher metal layers. The micrograph of produced layout is shown in figure [7.1](#).

While the chip was in production, test PCB board and antennas were designed and produced. EAGLE is used as PCB design tool. Jumper header pins are used for DC voltages whereas for ac inputs SMA connectors are used. Similarly, for decoupling and ripple rejection SMD MLCC capacitors are used but for stability purpose of LDO, electrolytic capacitor is used owing to requirement of better accuracy and higher ESR for compensation capacitor. In order to have better control of supplies to bias, buffer and pad circuits on board regulator is used. For convenience, instead of providing biases voltages from power supply, on board resistive network is implemented to generate required bias voltages. For sanity check of the chip, balun is used to created differential signal inputs. The test PCB and antenna are included in appendix.

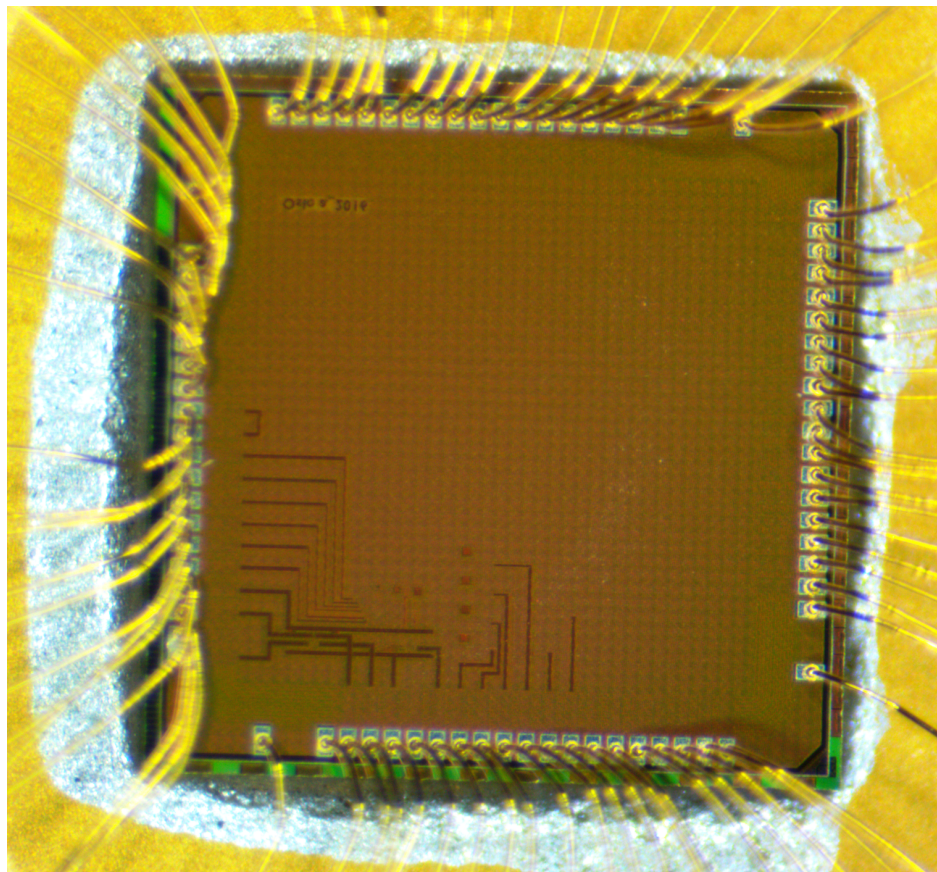


Figure 7.1: Micrograph of PMS chip

7.2 Measurement Setup

The laboratory setup done for measurement of data is shown in figure 7.2 . The primary antenna is driven by V_{ac} from arbitrary waveform generator, TGA 1244. The differential ac signals V_{in1} and V_{in2} generated from the secondary antenna, which are fed to the rectifier of PMS chip is measured with channel 1 and channel 2 of oscilloscope, Agilent 54624A. V_{rec} and V_{reg} are measured with channel 3 and channel 4 respectively. Agilent E3648A is used as power supply to the regulator on PCB. This regulator is generates 2.5 V as VDD and 1.18 V as V_{ref} . This VDD is used as supply for pad/ESD, on chip buffers and on board bias generation circuit. Keithley 6514 electrometer is used to measure current where required. All these devices are connected to a GPIB bus and controlled using Matlab script.

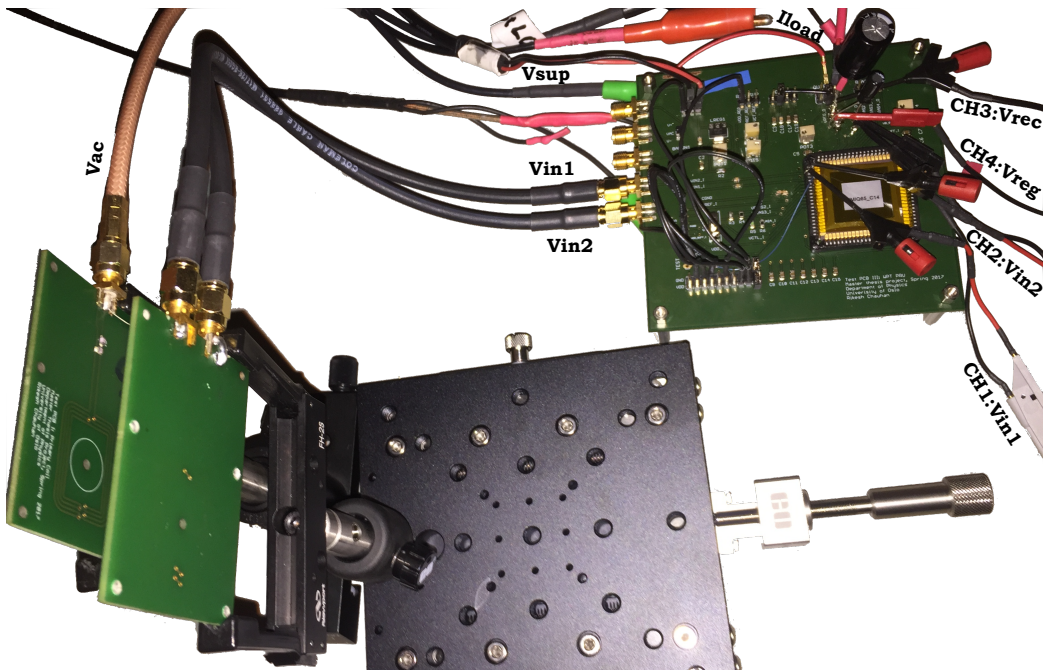


Figure 7.2: Measurement setup

7.3 Measurement Result and Discussion

As in simulation, first the performance of rectifier and LDO are measured, then PMS and finally WPT system, which are presented below.

7.3.1 Rectifier

For measuring the performance of rectifier on PMS chip, balun on test PCB is used to generate V_{in1} and V_{in2} . V_{ac} of 13.56 MHz frequency is supplied to the balun. Its magnitude is adjusted to 4.1 V so that the magnitude at the input of rectifier, V_{in} ($V_{in1} - V_{in2}$) is 2.6 V as in simulation. The bias and reference voltages for LDO are grounded in order to disable LDO for now. The potentiometer at V_{rec} node, as a load resistance, is adjusted for drawing 10 mA current.

Figure 7.3 shows measured input and output waveform for 10 mA load compared with corresponding PMS simulation. The average rectified output V_{rec} is a close to simulated value. The additional drop

Test and Verification

in measured V_{rec} is about 65 mV, which can be accounted to resistive drop along bonding wire, PCB trace and higher drain-source resistance of diodes. This assumption results in resistance of 6.5Ω in V_{rec} path, which in real cannot be so big. This means more than 10 mA current is drawn from the rectifier, proportionally dropping this higher voltage. The additional current may have been drawn by LDO because the LDO might not be completely turned off.

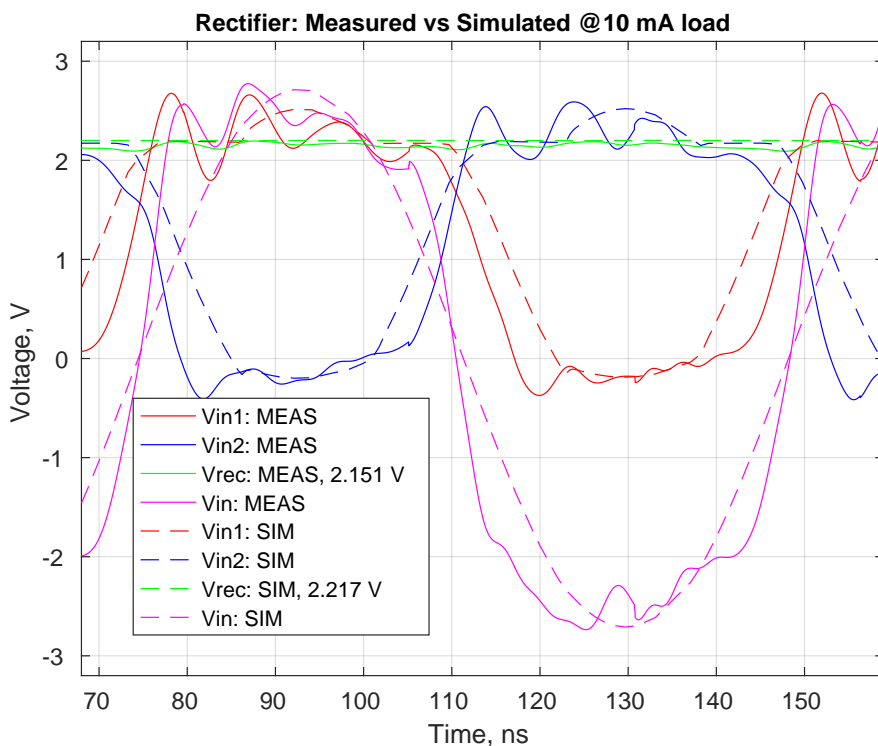


Figure 7.3: Measured rectifier waveform for 10 mA load

The differential input waveforms are similar in shape but during diode conduction the measured waveforms are distorted: V_{in1} and V_{in2} have additional peak and valley when rectifying diode are turned on and off respectively. [33] has discussed about similar issue in rectifier performance and accounted this distortion for parasitic inductance of bonding wire and PCB trace in addition with probe and pad capacitance while operating at higher frequency. In order to verify this clarification, the top level test bench is re-simulated with approximate parasitic inductance and capacitance and the distortion in V_{in1} and V_{in2}

Test and Verification

is noticed as in the result above. This distortion has affected the comparator performance resulting in faster turning on diodes and later turning off diodes. The later turning off of diodes results in reverse leakage current.

Figure 7.4 is performance of rectifier for 1 mA load where the distortion due to energy storing and realising in the parasitic inductor and capacitors is less pronounced. The simulated and measured performance is a close match in this case.

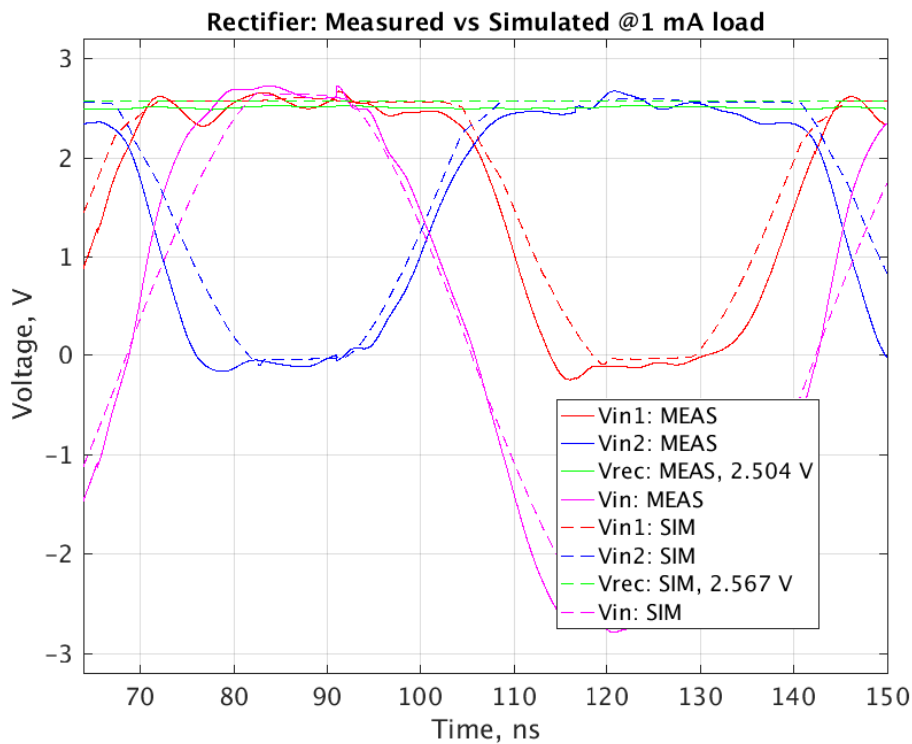


Figure 7.4: Measured rectifier waveform for 1 mA load

The measured rectified output for various load is presented in figure 7.5. The average rectified DC value is as expected but the ripple is unexpectedly higher. The ripple rejection capacitor was replaced with 100 μ F capacitor hoping for reduced ripple but only few milli volt reduction was observed. The frequency of ripple was 35 MHz, higher than 2 times the operating frequency which means the distortion in inputs is causing multiple conduction in a half cycle. The peaks in ripple

Test and Verification

corresponds to additional conduction during turning on of diodes and valleys in ripple corresponds to occurrence of reverse leakage during turning off time.

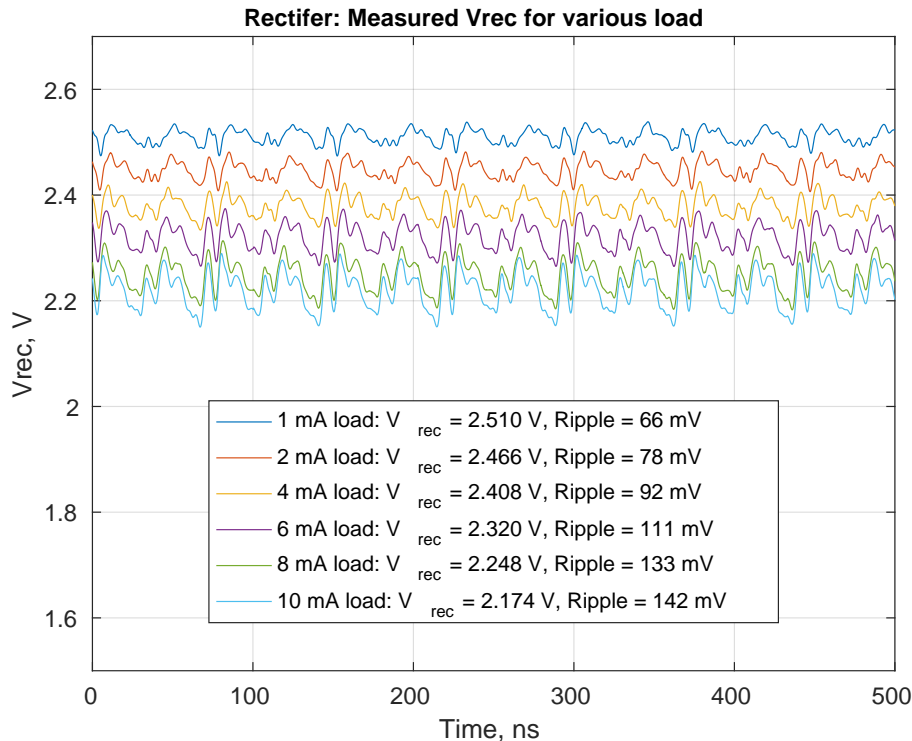


Figure 7.5: Measured rectifier output for various load

In order to measure input power, P_{in} , from signal source V_{ac} , first a 5Ω current sense resistor was connected in series between supply and balun and voltage drop across this resistor was measured. Current drawn from the source was then calculated by dividing voltage drop across the series resistor by its resistance value. Using Matlab, the average input power was calculated by integrating the product of instantaneous current waveform and input voltage waveform, V_{in} in figure 7.3 and dividing it by integration time, as in equation 7.1.

$$P_{avg} = \frac{1}{T_2 - T_1} \int_{T_1}^{T_2} v(t).i(t)dt \quad (7.1)$$

Similarly, output power, P_{load} delivered to load, realised with potentiometer, was calculated as product of rms value of V_{rec} and dc current,

I_{load} value read by Keithley 6514 electrometer measured at V_{rec} node, as in equation 7.2.

$$P_{load} = V_{rec_{rms}} \cdot I_{load} \quad (7.2)$$

For delivering 10 mA output current to load, V_{rec} is 2.151 V i.e 21.51 mW output power, the measured input power is 33.74 mW.. The results in measured efficiency of rectifier to be 62.5%.

Table 7.1: Rectifier measured performance

	Measured	Post-layout
Input magnitude	2.6 V	2.65 V
Rectified DC	2.17 V	2.285 V
Ripple Vpp	142 mV	4 mV
PCE	64.4 %	80.5 %
VCE	80.4 %	87.8 %

The post layout performance of rectifier is obtained from PMS simulation by disabling LDO. This is done in order to imitate the measurement scenerio.

7.3.2 LDO

For measuring the performance of LDO on PMS chip, no differential inputs to the rectifier was applied. The biasing and reference voltages given in table 6.1 were generated on test PCB and applied to PMS chip.

Figure 7.6 is the regulated voltage V_{reg} of LDO when the input voltage V_{rec} was swept using a voltage source. The load current was set to 5 mA by adjusting potentiometer. It is seen that the pass device starts conducting at around 1.9 V input and the regulated output is 1.8 V for both simulated and measured results. However the significant difference minimum drop across pass device. The measured minimum drop across pass device is 0.55 V compared to simulated 0.15 V which means minimum input voltage required for LDO to work is measured to be 2.45 V which is much higher than the simulated performance which is 1.95 V. This is be due to the produced pass device having much higher resistance than shown by simulation. This problem could have

been avoided by making the pass device much wider.

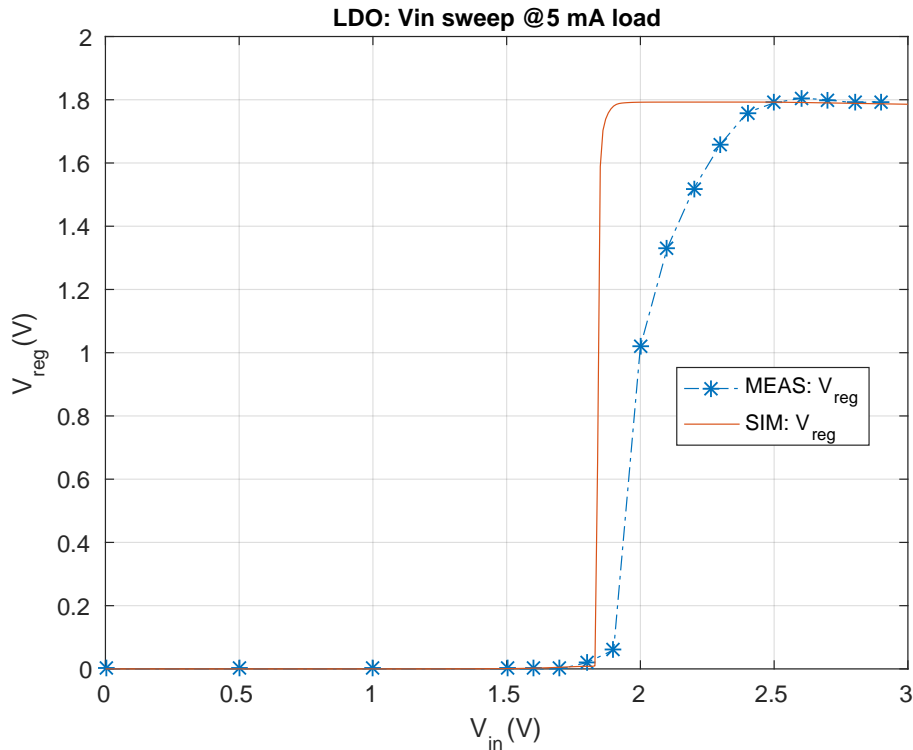


Figure 7.6: LDO input sweep for 5 mA load

Figure 7.7 is the performance of LDO when the load was swept from 0 mA to 11 mA by adjusting potentiometer. 2.45 V was applied as input because it is the minimum input required for the LDO to work as given in figure 7.6. The regulated output V_{reg} and current drawn from the source were measured in order to note quiescent current.

The variation in V_{reg} is not greater than 5 % of nominal value of 1.8 V i.e. within the desired margin. However, the quiescent current is much higher than simulated result. It is seen that measured quiescent current is 4 mA in average for all load current which was only 115 uA in simulation. This quiescent current is not entirely the leakage in the LDO. A rectifier turn down switch should have been made to turn off rectifier while testing LDO. So during this measurement rectifying diode in the rectifier were turned on, conducting some current through them. The large quiescent current of LDO is accounted for this diode

current.

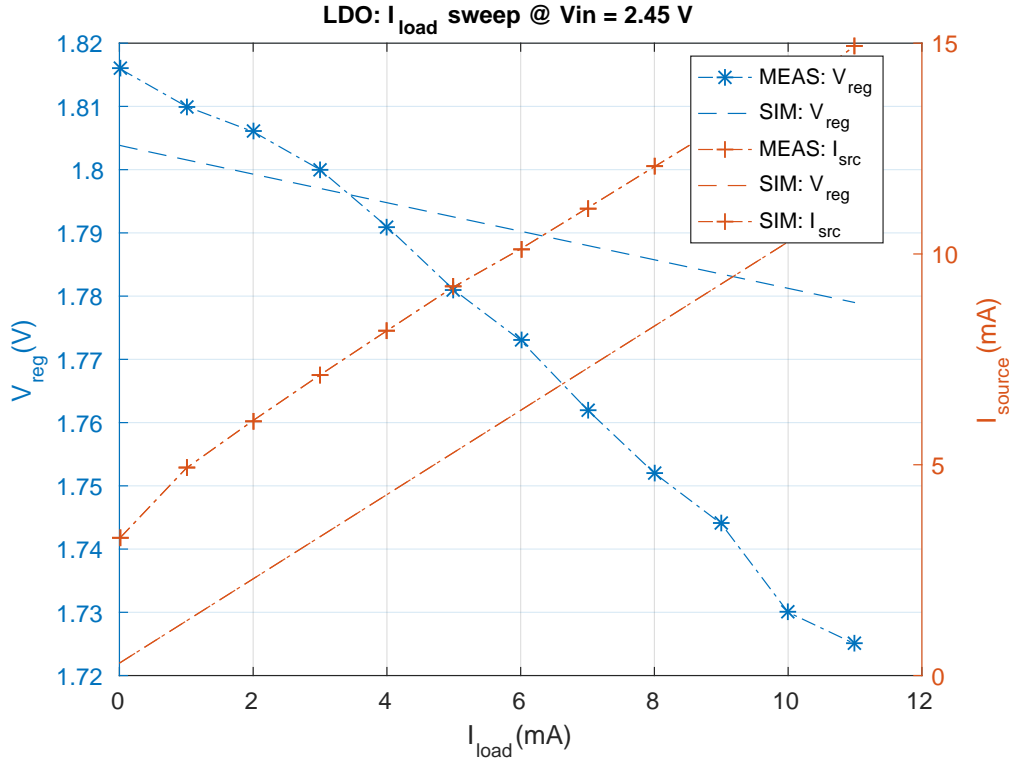


Figure 7.7: LDO load sweep

7.3.3 PMS Chip

As the PMS produced here consists of rectifier followed by LDO, the LDO should be able to operate with the given performance of rectifier. On verifying the LDO above, one limitation is observed. The minimum input voltage required to operate LDO is much higher than rectified output V_{rec} when operating to deliver 10 mA current. This has limited the further use of LDO in PMS system. Hence for the discussion ahead, rectifier is only considered as PMS. To check the sanity of LDO, its performance for 4 mA load which tightly meet the requirement of minimum input voltage is presented in figure 7.8.

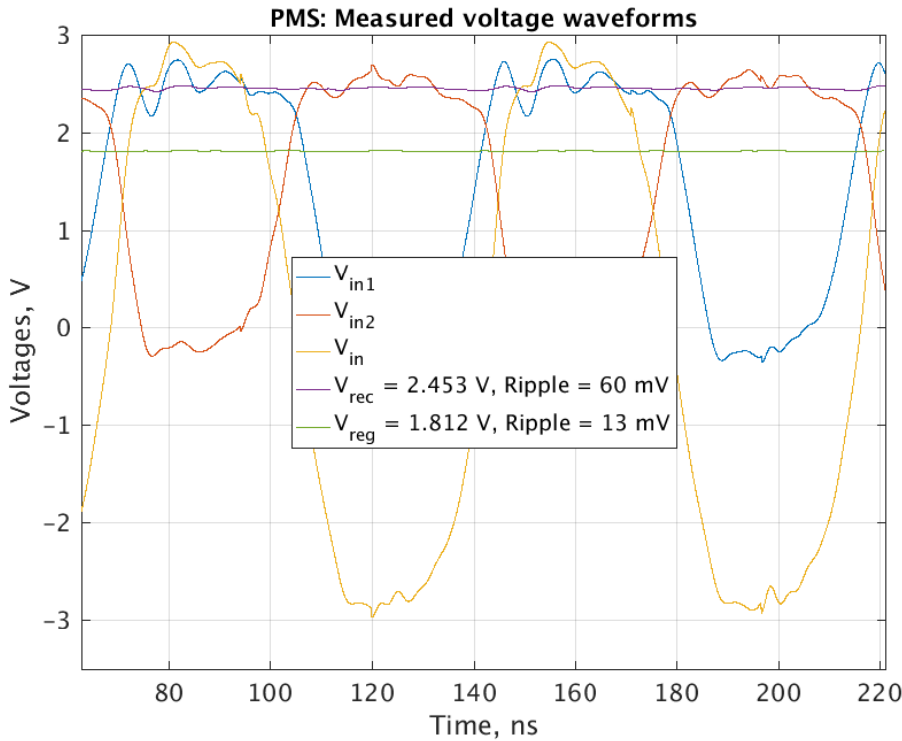


Figure 7.8: PMS performance

7.3.4 WPT System

For measuring the performance of WPT system, the setup is done as shown in figure 7.2. The measurement results of magnetic resonant inductive link with 5 mm coupling separation is presented here. 3.8 V magnitude sinusoidal signal is required to drive primary antenna in order to generate 2.65 V differential signals in the secondary coil.

The measured voltages waveform for 10 mA load is presented in figure 7.9 along with simulation result. The additional drop in V_{reg} , distortion of inputs, V_{in1} and V_{in2} and larger ripple are due to the same reasons discussed in rectifier measurement. The distortion is more pronounced here because of additional parasitic from the transfer link.

Figure 7.10 shows measured current and voltage in the primary coil. Input and output powers are calculated as discussed in rectifier measurement section. Here current sense resistance is used in series to primary coil. Thus obtained input power to primary was 45.6 mW to

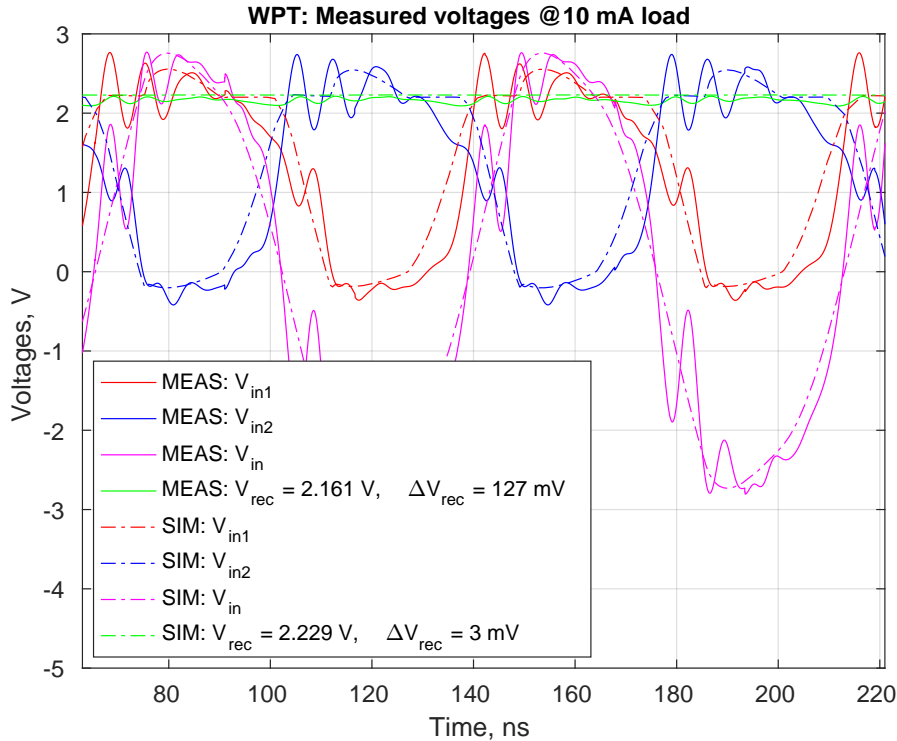


Figure 7.9: WPT from 5 mm coupling: voltage waveform

deliver 21 mW to load. This results in measured efficiency of 46.1 %. This to make things clear that this efficiency is the transfer efficiency from primary to rectifier output excluding LDO. Using rectifier measured efficiency from earlier section, the efficiency of resonant inductive link is 70.5 %.

The decreased efficiency can be explained with two main factors: effect of parasitics on rectifier and non-optimal resonance. As explained in rectifier measurement result, the parasitic capacitance and inductance have caused the distortion of rectifier inputs, significantly affecting the comparator performance which was designed to avoid reverse leakage of current. Similarly magnetic resonance created at the transfer link is dependent both on load and distance between the coil. During tuning of transfer link the load was modelled as dc load including the LDO, which is disabled during measurement due to its limitations, and not to mention rectifier itself being non-linear load which is always subjected to change.

Test and Verification

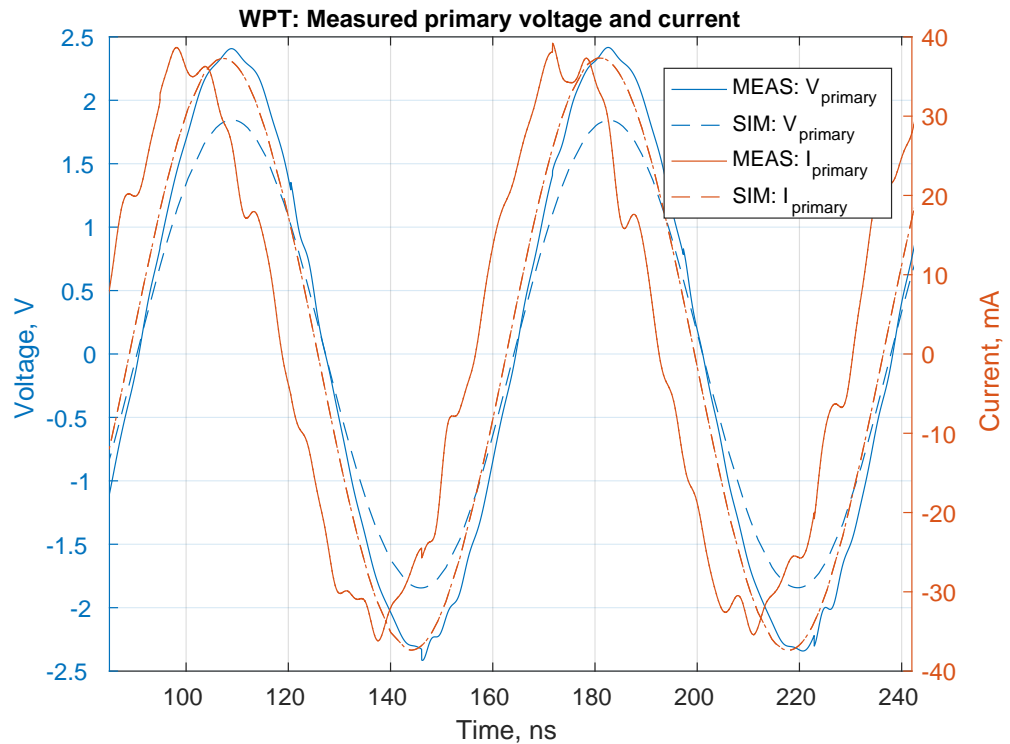


Figure 7.10: WPT 5 mm coupling: Voltage and current at primary coil

The measured performance of WPT with 5 mm coil separation is summarised in table 7.2

Table 7.2: WPT measured performance for 5 mm coupling

	Measured	Post-layout
V_{ac}	3.8 V	3.6 V
V_{rec}	2.1 V	2.23 V
ΔV_{rec}	113 mV _{pp}	2.8 mV _{pp}
η_{wpt}	46.1 %	63.4 %

Once again just to avoid confusion, it should be mention here that performance summary given in table 7.2 is for WPT system constituting resonant inductive link and rectifier.

As in simulation the performance is measured for 1.5 mm and 10 mm coil separation too. On doing so, the transfer link is realised with their respective resonant primary and secondary coil held at respective distance. The input voltage and current at the primary antenna for all three coupling cases for 10 mA load at rectifier output is shown in figure 7.11.

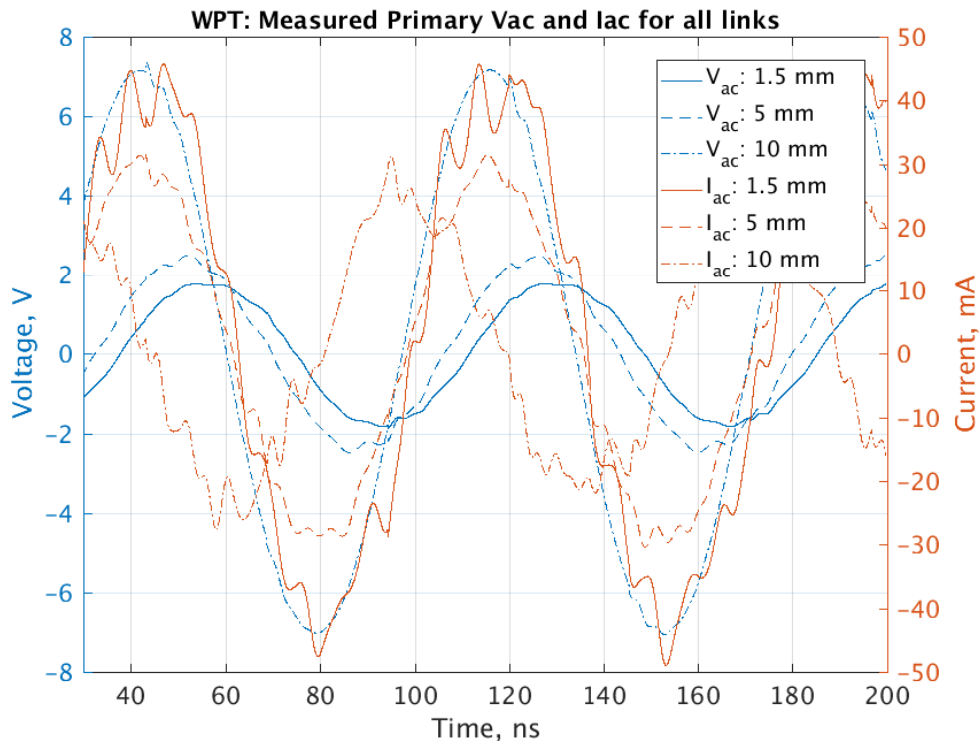


Figure 7.11: Primary voltage and current for various inductive link

On observing the voltage and current waveform in figure 7.11, it is found that their amplitude and phase difference are comparable to the simulated result for 1.5 mm and 5 mm distance coupling. However for the case of 10 mm, the phase difference between current and voltage has increased, thereby requiring much higher input voltage to deliver the same output current. As in other two case, load variation, unaccounted parasitic capacitance in simulation and inaccuracy in coil separation have obviously shifted the resonance frequency. In addition, [28], reports that optimisation for weakly coupled link should be done together with rectifier and regulator.

Test and Verification

The measured performance for all three cases of coupling are presented in table 7.3

Table 7.3: WPT measured performance for all inductive links

	Sepr: 1.5 mm	Sepr: 5 mm	Sepr:10 mm
V_{ac}	3.75 V	3.8 V	7.8 V
I_{peak}	45.3 mA	39.2 mA	28 mA
P_{in}	39.7 mW	45.6 mW	99.7 mW
η_{wpt}	52.9%	46.1 %	21 %

Part V

Conclusion

Chapter 8

Conclusion

In this project, wireless power harvesting system was designed, analysed, produced and tested. Magnetic resonance inductive coupling method was used for wireless power transfer. The WPT chip was produced using 90 nm CMOS devices. The target performance was to wirelessly power 10 mA load with 1.8 V.

The post-layout simulation result, summarised in table 6.3, showed that the target objective of WPT system implemented in this project can be achieved with efficiency greater than 50 %. Measured performance of rectifier was decent, the limitation being effect of parasitic inductance and capacitance. Similarly, in spite of leakage issue, LDO measured performance showed that its functionality agreed with the simulation result. The inductive link power transfer efficiency for strong and moderate coupling was reasonable good enough to give measured WPT system efficiency of 46.1 % taking rectifier only as PMS.

To sum up the work, it can be said that the conceptual design of WPT implemented in this work was approved by simulation, with measured results backing the simulated performance. The analysis of degraded measured results were traced to layout design of PMS and effect of parasitics.

8.1 Design issues

In course of this WPT chip design, I came across many design issues, most of which I learnt after the design. I learnt that these issues have

Conclusion

direct impact on the performances of the system and on addressing these issues the performance of the WPT system can be significantly improved.

- I followed a text book approach for designing which I later realised not to be an optimal design choice. For example, choosing device length 3 times the minimum feature size. Though simulation across all corners met the target requirements with chosen technique, there was still plenty room on the chip. Bigger devices sizes could have, on the one hand, make good use of available room and on the other hand, it could certainly have made the produced chip less prone to PVT variation.
- During verification of the chip, larger ripples, both in V_{rec} and V_{reg} were measured. The main reason for this is rectifier and LDO sharing the same ground path. During conduction of MOS diodes large ac current passed through the ground, eventually creating higher ripples and requiring large ripple rejection capacitors. Separate ground for rectifier and LDO and wider gaurding around the noisy rectifier, could have minimised the ripple amplitude in rectified output. Similarly, the higher current path reaching the diodes should be made with equal resistance. A slight difference in path resistance was observed in this design which resulted in asymmetric conduction of rectifying diodes.
- A more detail analysis of magnetic resonance inductive link is required. The coupling link was designed for fixed resonance frequency at 13.56 MHz but shift in resonance frequency was observed while taking measurements of WPT chip. It was mostly due to variation of load and inaccuracy in coil separation.
- The test PCB could have been made better in terms of both performance and test connivence. The current conduction paths, V_{in1} and V_{in2} should have been made shorter and symmetrical. The decoupling capacitors and ripple rejection capacitors should be place closer to their corresponding JLCC pins. For making measurements easier, more test points are required, especially current measurements points.
- The top level test-bench of WPT chip can also be improved to realise a real measurement set up. Inclusion of parasitics of probes increases the accuracy of measured data and hence the verification of performance. More important is inclusion of pad resistance

Conclusion

and capacitance which are the source of voltage/power loss and shift of resonance frequency respectively. Moreover, power down switches should be added to disable rectifier and LDO so that they can be tested separately.

8.2 Future Work

As this work is done as pilot project of implementing of WPT in 90 nm. it can be taken as a starting point to build an optimal WPT system for either charging or directly driving low power devices. I think it can work as reference and/or preliminary work on following perspective future works.

- The same design choices and architectures can be optimised for better efficiency in specific application. The boundary condition, problems and challenges discussed above should be first addressed. Other additional work includes, integration of over voltage protection circuit for rectifier and BGR for on chip biasing and reference voltage generation.
- Design and implementation of communication and transfer protocol between PTU and PRU can be other additional topic relating to this work. One can implement standard commercial protocols like Qi and AirFuel or can design one's own protocol optimised for specific application. On completion of these works, a complete independent WPT system is made.

Appendices

Appendix A

Rectifier Implementation

Rectifier Implementation

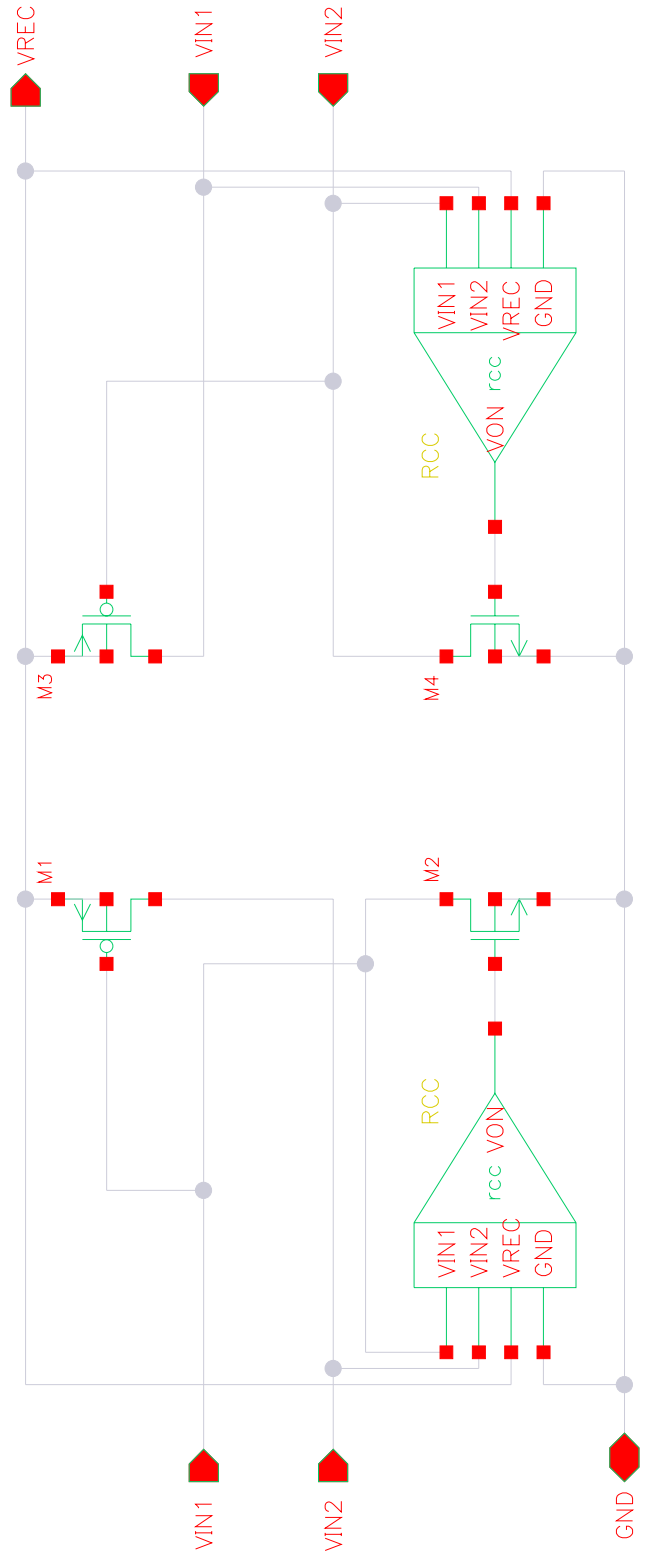


Figure A.1: Schematic of Rectifier

Rectifier Implementation

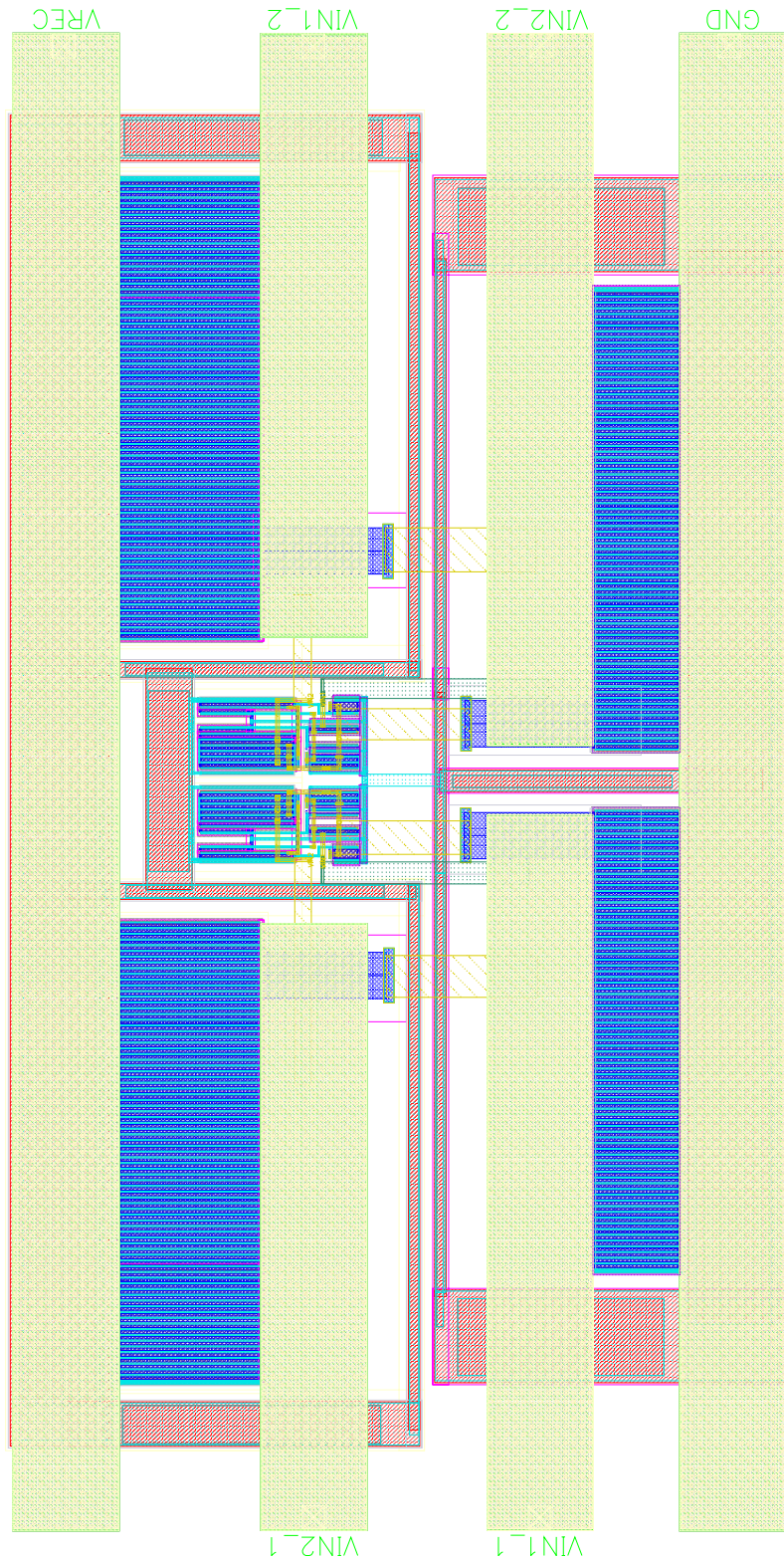


Figure A.2: Layout of Rectifier

Appendix B

LDO Implementation

LDO Implementation

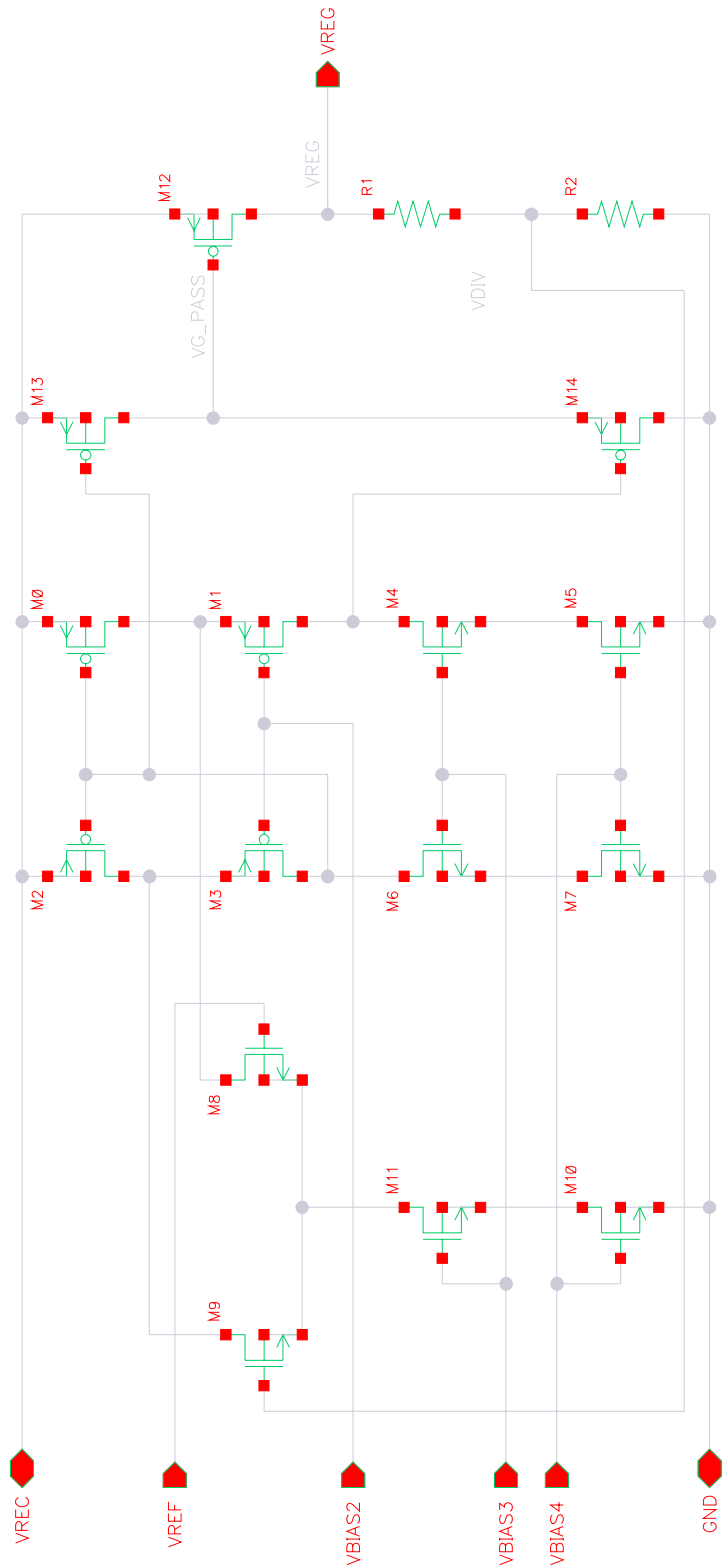


Figure B.1: Schematic of LDO

LDO Implementation

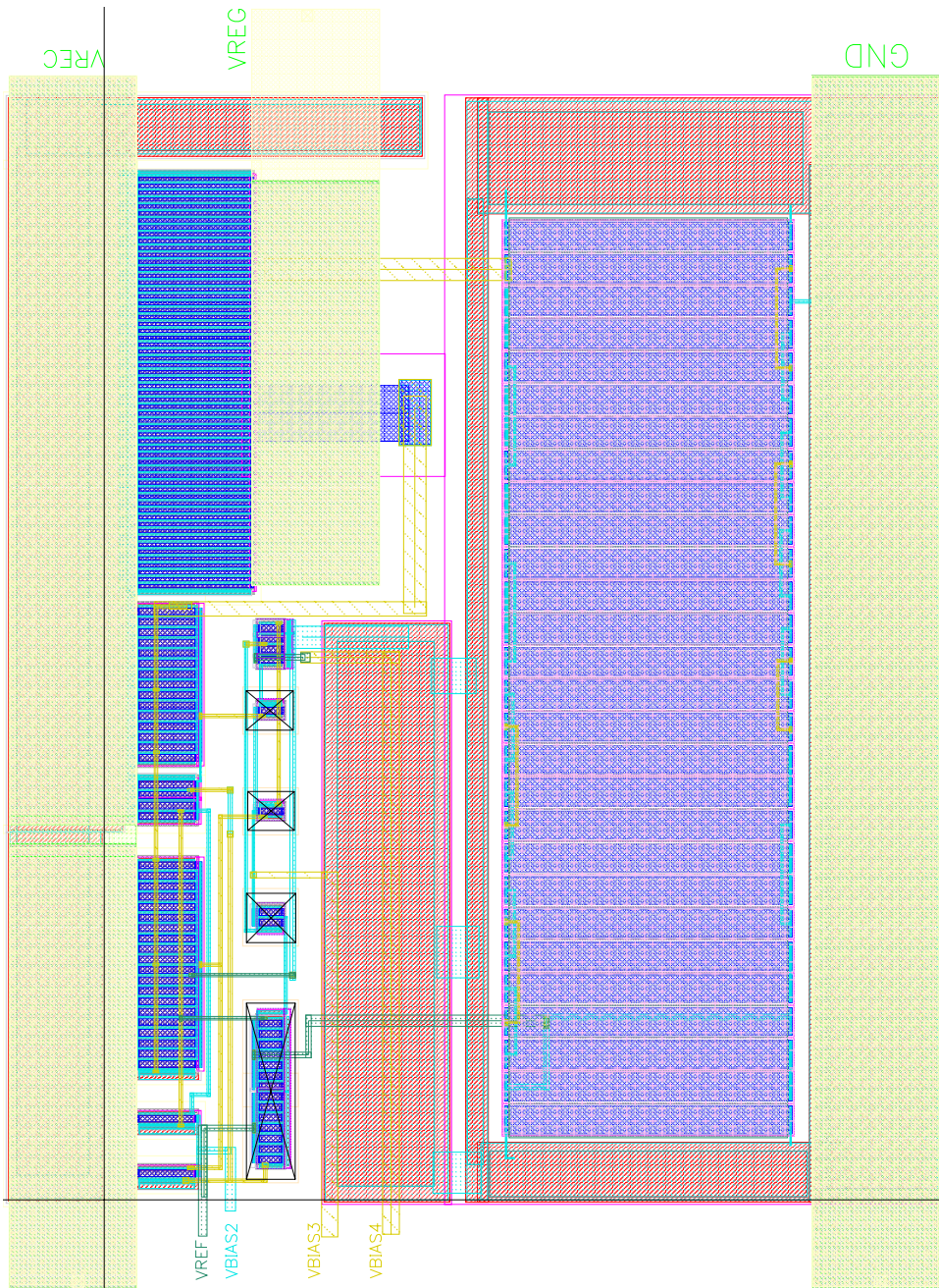


Figure B.2: Layout of LDO

Appendix C

PMS Chip

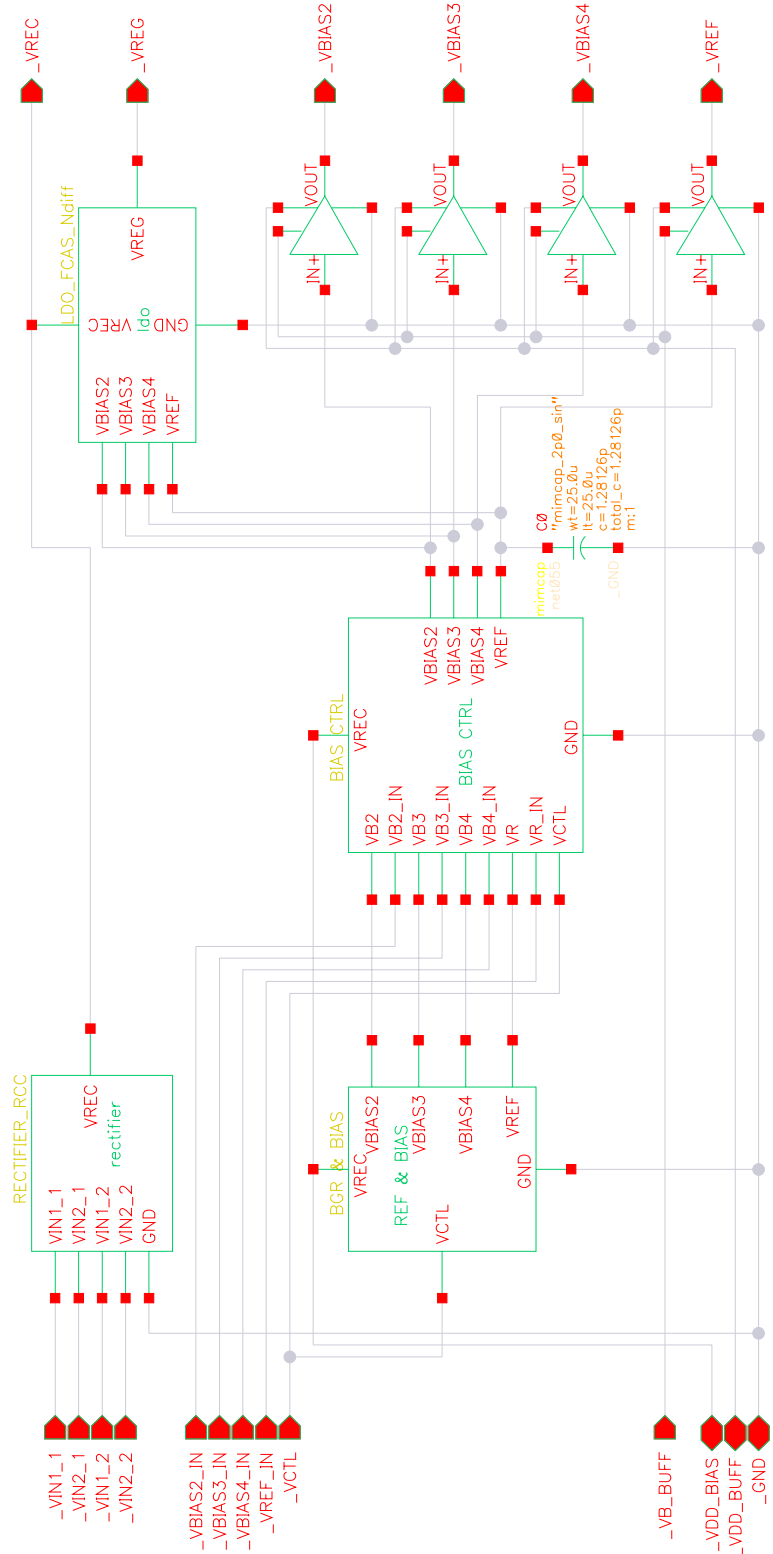


Figure C.1: Schematic of PMS chip

PMS Chip

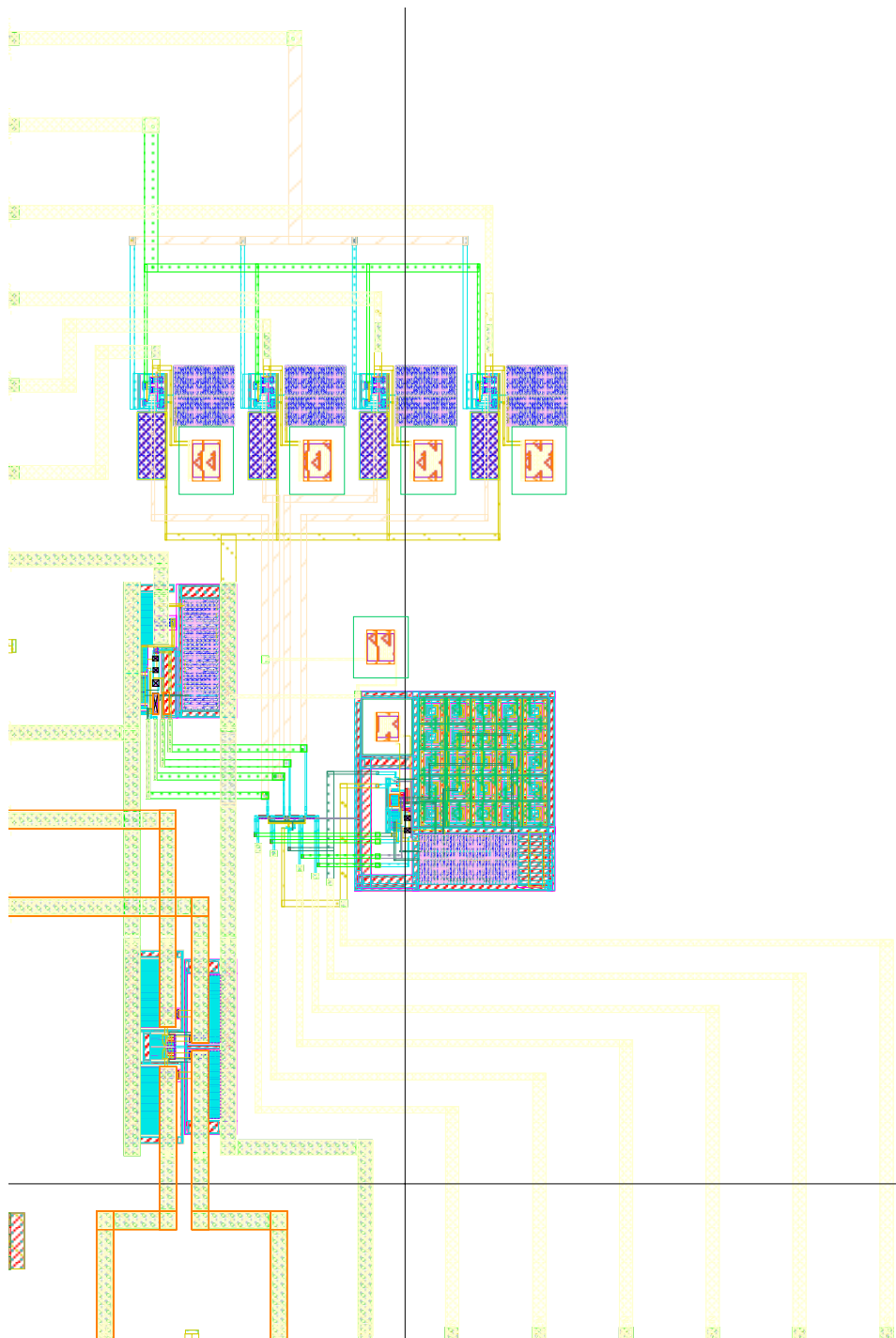


Figure C.2: Layout of PMS chip

Appendix D

Test PCBs

Test PCBs

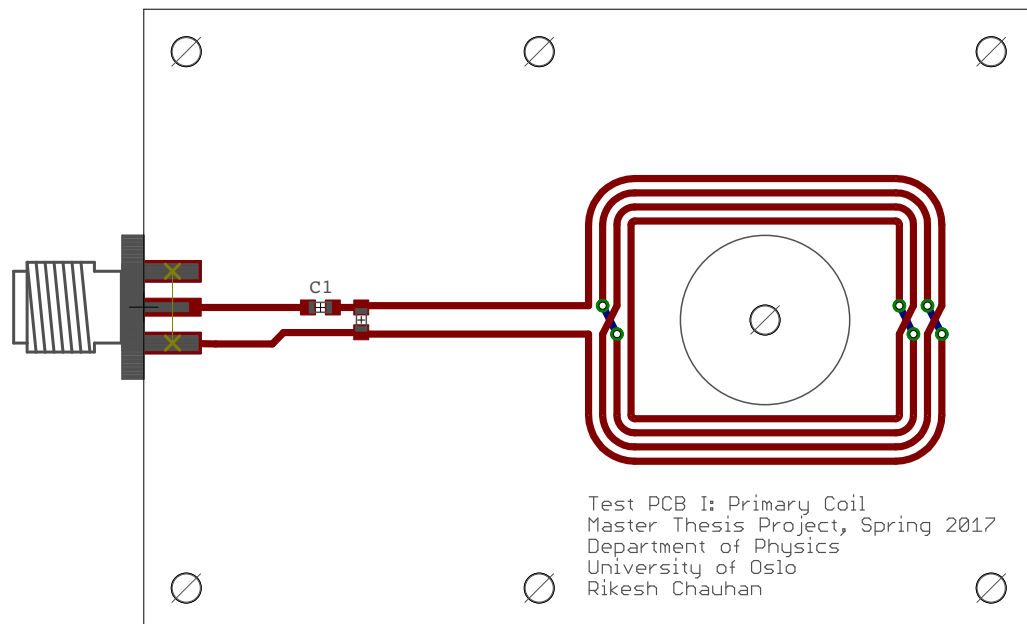


Figure D.1: Primary antenna layout

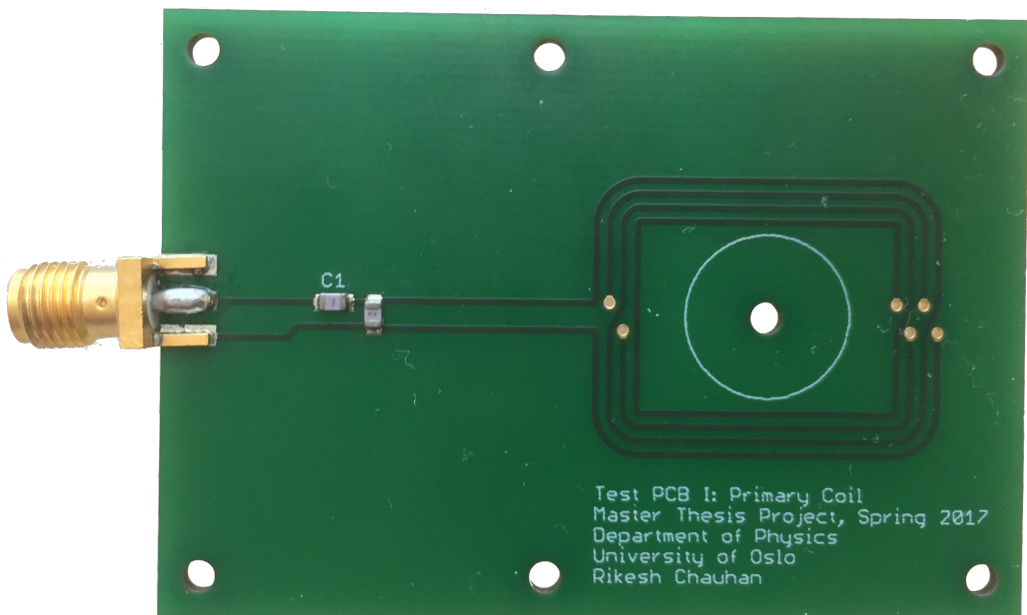


Figure D.2: Primary antenna PCB

Test PCBs

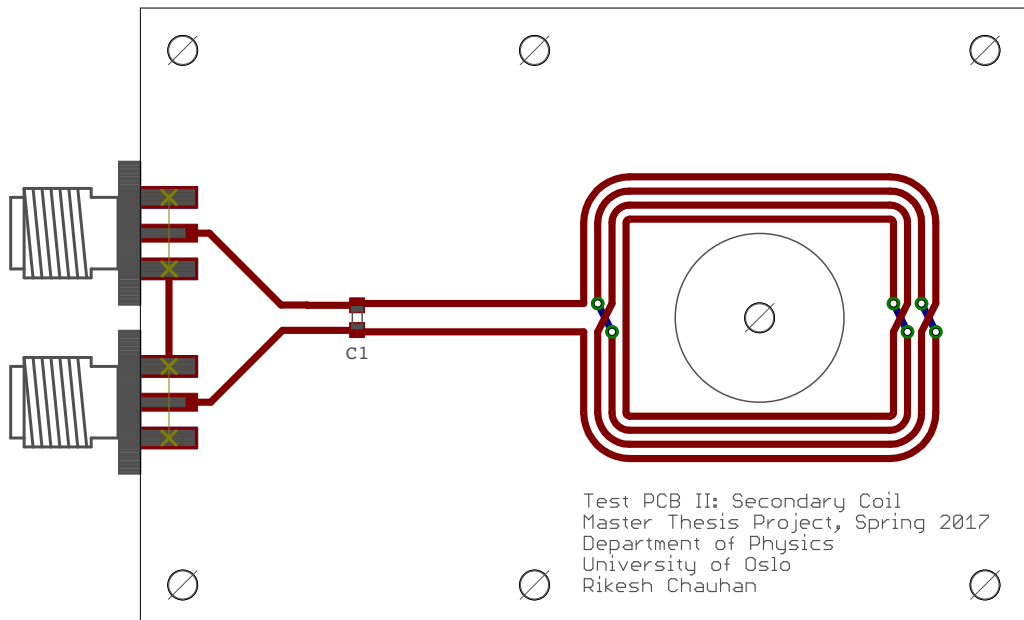


Figure D.3: Secondary antenna

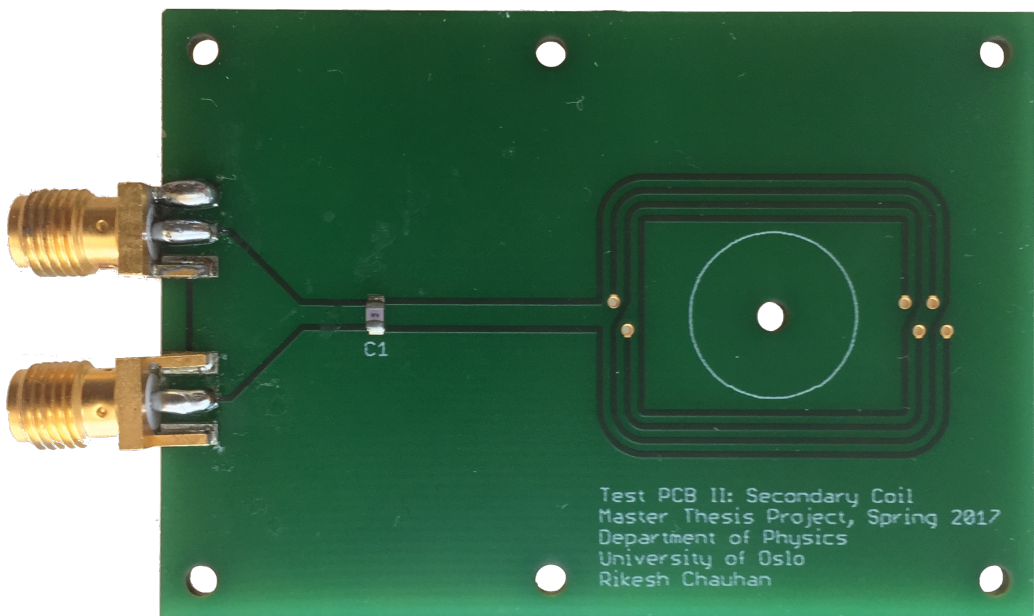


Figure D.4: Secondary antenna PCB

Test PCBs

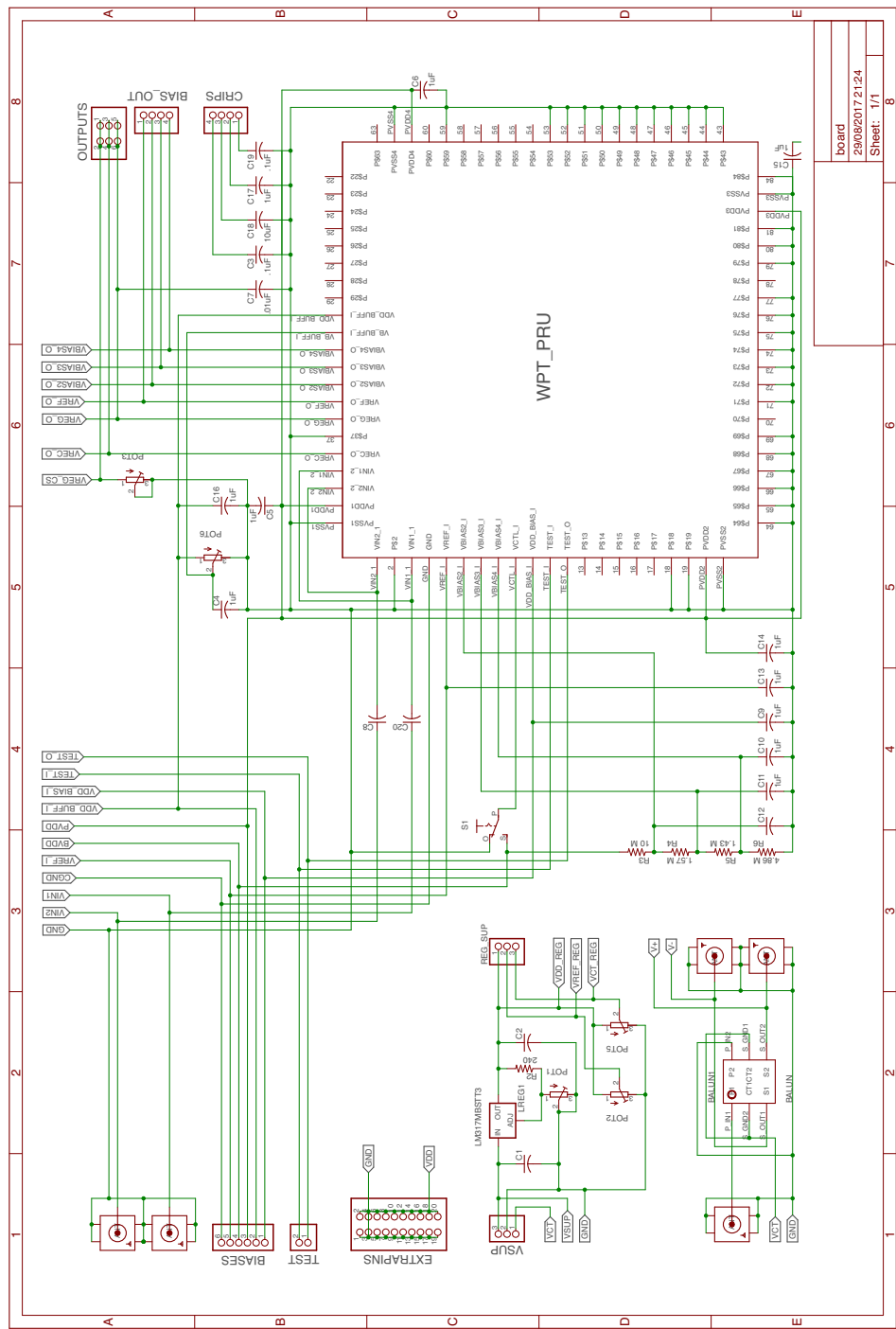


Figure D.5: Test PCB schematic

Test PCBs

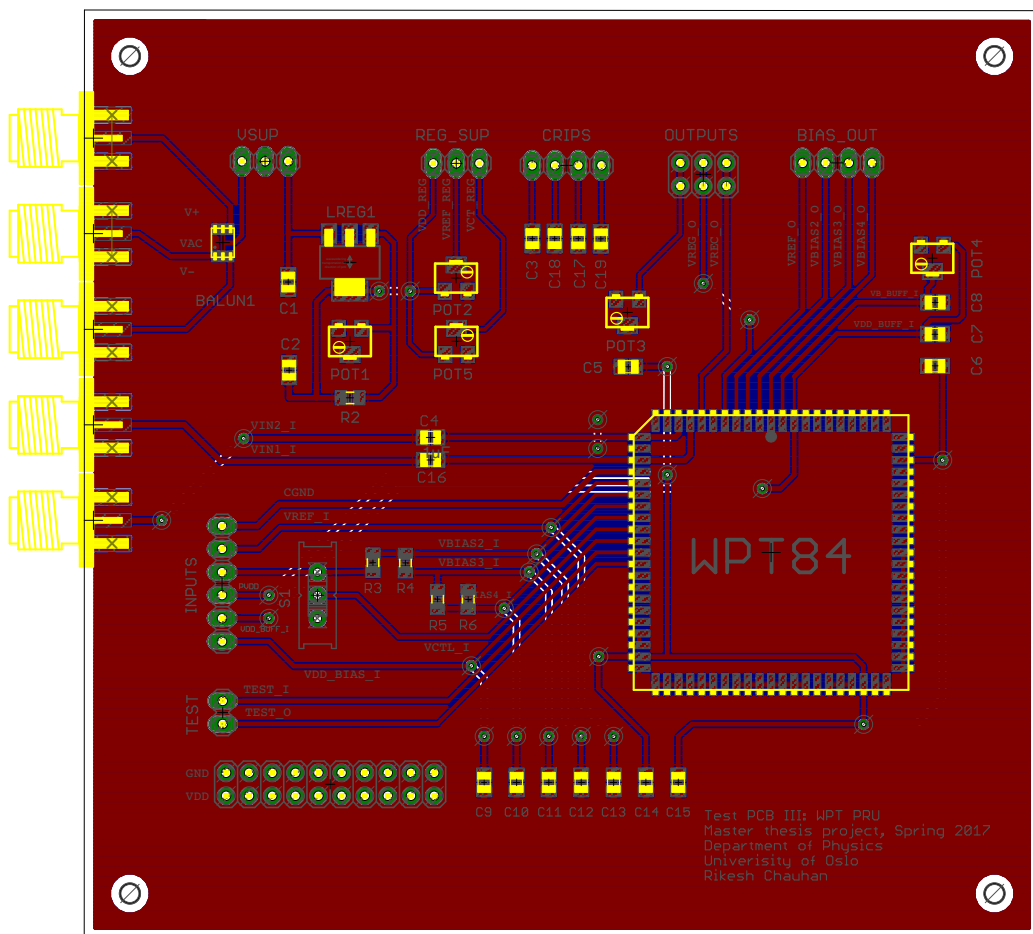


Figure D.6: Test PCB board layout

Test PCBs

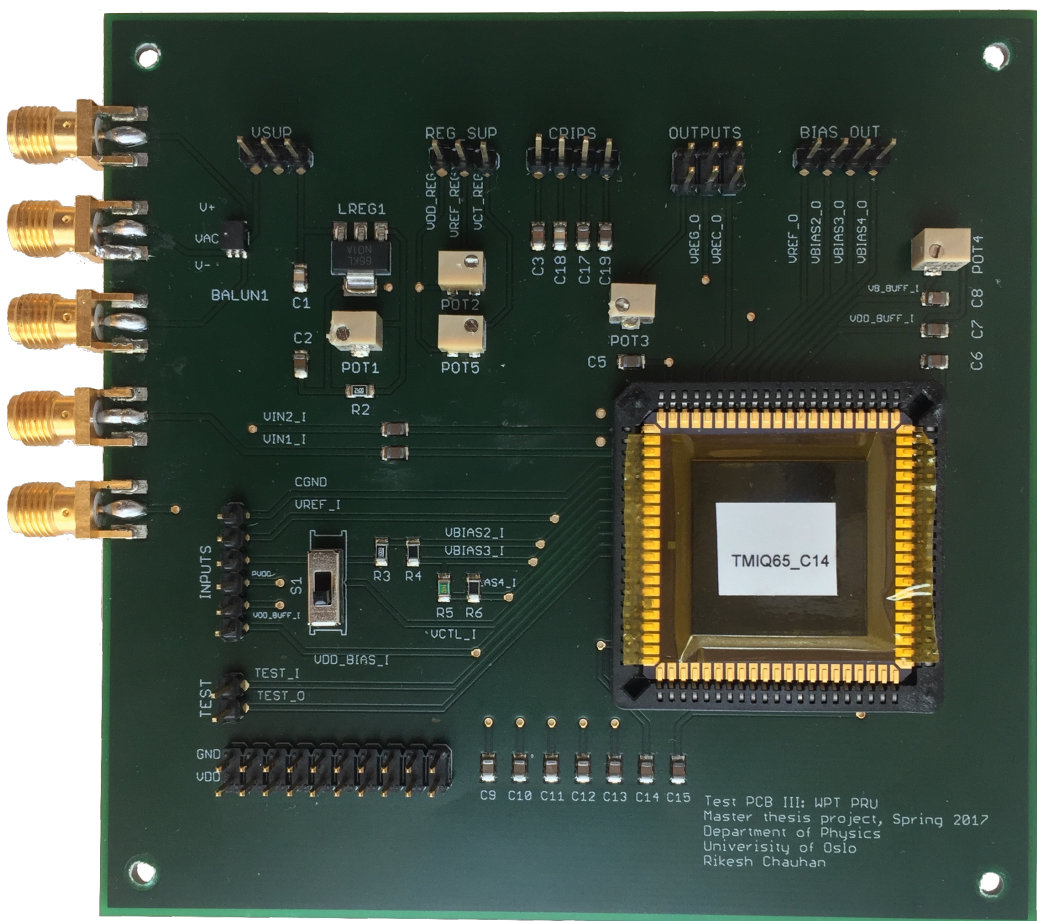


Figure D.7: Test PCB board

Appendix E

Matlab code for PMS measurement

```
1 clear all;
2 addpath(genpath('/home/mes/src/matlab/gpib/linux'));
3
4 %% Parameter declaration and initailisation
5 Voffset1 = 0;
6 Vamp1      = 3;           % Vpp in function generator
7 Freq1      = 13.56*10^6;
8 Vlimit     = 5;           % device range 2V-200V
9 Ilimit     = 20*10^-3;    % device range 20pA-20mA
10 mode      = 'I';
11 pause(1);
12
13 %% Instruments GPIB address
14 TTI1244_address = 6;      % Arbitrary function generator
15 HP54622_address = 24;     % Oscilloscope
16 K6514_address   = 18;     % Electrometer DMM
17 HPE3631_address = 8;      % Power supply
18
19 %% Power supply initailisation and setup
20 HPE3631Init(HPE3631_address);
21 HPE3631_SetILimit(1, 0.05);
22 HPE3631_SetILimit(2, 0.05);
23 HPE3631_SetVolt(1, 4);   % To regulator on PCB "Vsup"
24 HPE3631_SetVolt(2, 0);
25 HPE3631_Operate();
```

Matlab code for PMS measurement

```
26 pause(1);  
27  
28  
29 %% Function generator initailisation and setup  
30 TTi1244_Init(TTi1244_add);  
31 TTi1244_SetChannel(1); % Channel 1 as "Vac"  
32 TTi1244_SetTerm('50');  
33 TTi1244_SetWaveform('SINUS');  
34 TTi1244_SetAmplitude(Vamp1);  
35 TTi1244_SetFrequency(Freq1);  
36 TTi1244_DCoffset(Voffset1);  
37 TTi1244_ChannelEnable('ON', 1);  
38 pause(1);  
39  
40 %% Multimeter initailisation and setup  
41 GPIB_Write('*CLS;*RST;', K6514_add);  
42 K6514_SetMode(mode);  
43 K6514_SetRange(ILimit);  
44 pause(1);  
45 %K6514_QuickMeasure();  
46  
47 %% Oscilloscope initailisation and setup  
48 GPIB_Write('*CLS;*RST;', HP54622_add);  
49 %HP54622_AutoScale(1); % autoscaling channel 1  
50 HP54622_SetVerticalRange(1, 3, 0); % voltage scale  
51 HP54622_SetTimeScale(2*1/Freq1); % time scale  
52 pause(1);  
53 [time, data] = GetData(HP54622_DefaultAddr); % read all  
      channels  
54 Vrec_freq = HP54622_MeasFreq(3); % Vrec ripple freq  
55 Vreg_freq = HP54622_MeasFreq(4); % Vreg ripple freq  
56 pause(1);  
57  
58 Vin1 = data(:, 1); Vin1_vpp = peak2peak(Vin1); %  
      Channel 1 as "Vin1"  
59 Vin2 = data(:, 2); Vin2_vpp = peak2peak(Vin2); %  
      Channel 2 as "Vin2"  
60 Vrec = data(:, 3); Vrec_avg = mean(Vrec); %  
      channle 3 as "Vrec"  
61 Vrec_rip = peak2peak(Vrec);
```

Matlab code for PMS measurement

```
62 Vreg = data(:, 4); Vreg_avg = mean(Vreg); %  
    channle 4 as "Vreg"  
63 Vreg_rip = peak2peak(Vreg);  
64 Vin = Vin1 - Vin2; Vin_vpp = peak2peak(Vin)/2; % "Vin"  
65 time = time * 10^9 + 250; % in ns and starting with  
    0 ns  
66  
67 %% Plotting all voltage waveforms  
68 f1 = figure(1);  
69 plot(time, Vin1 , 'r', time, Vin2 , 'b', time, Vrec , 'g'  
    , time, Vreg , 'm'); hold on;  
70 plot(time, Vin); hold off;  
71 xlim = ([0, 500]);  
72 xlabel('Time, ns');  
73 ylabel('Voltages, V');  
74 grid on;  
75  
76 vin1_legend = sprintf('Vin1: V_{pp} = %.3f V,  
    Vin1_vpp);  
77 vin2_legend = sprintf('Vin2: V_{pp} = %.3f V,  
    Vin2_vpp);  
78 vrec_legend = sprintf('Vrec: V_{pp} = %.3f V, V_{avg}  
    = %.3f V', Vrec_rip, Vrec_avg);  
79 vreg_legend = sprintf('Vreg: V_{pp} = %.3f V, V_{avg}  
    = %.3f V', Vreg_rip, Vreg_avg);  
80 vin_legend = sprintf('Vin : V_{pp} = %.3f V, Vin_vpp  
    );  
81 legend(vin1_legend, vin2_legend, vrec_legend, vreg_leg  
    , vin_legend', 'location', 'best');  
82 title('PMS: Measured voltages', 'FontSize', 10);  
83  
84 %% save plot the plot  
85 set(f1, 'Units', 'Inches');  
86 pos = get(f1, 'Position');  
87 set(f1, 'PaperPositionMode', 'Auto', 'PaperUnits', 'Inches  
    ', 'PaperSize', [pos(3), pos(4)]);  
88 print(f1, 'pms_all_vs.pdf', '-dpdf');  
89 movefile('pms_all_vs.pdf', '../../../../../img/meas/  
    pms_all_vs.pdf');
```

Acronyms

A4WP Alliance for Wireless Power

BJT Bipolar Junction Transistor

CMOS Complementary Metal-Oxide-Semiconductor

CPT Capacitive Power Transfer

DC Direct Current

ESR Equivalent Series Resistance

FCC Federal Communications Commission

GM Gain Margin

ICMR Input Common Mode Range

IEEE Institute of Electrical and Electronics Engineers

IPT Inductive Power Transfer

JLCC J-Lead Chip Carrier

LDO Low Dropout Regulator

MLCC Multi-Layer Ceramic Capacitor

MOS Metal-Oxide-Semiconductor

nMOS n-channel MOS

PCB Printed Circuit Board

PCE Power Conversion Efficiency

PM Phase Margin

Acronyms

pMOS p-channel MOS

PMS Power Management System

PRU Power Receiving Unit

PSSR Power Supply Rejection Ratio

PTU Power Transfer Unit

PVT Process Voltage Temperature

RF Radio Frequency

RFID Radio Frequency Identification

SMA SubMiniature Coaxial Connector version A

SMD Surface Mounted Device

SMPS Switch Mode Power Supply

SOC System On a Chip

SRF Self Resonance Frequency

TSMC Taiwan Semiconductor Manufacturing Company

UGF Unity Gain Grequency

VCE Voltage Conversion Efficiency

V_p Peak Voltage

V_{pp} Peak to Peak Voltage

V_{tn} Threshold Voltage of n-channel MOS

V_{tp} Threshold Voltage of p-channel MOS

WPT Wireless Power Transfer

Bibliography

- [1] J. A. Paradiso and T. Starner. ‘Energy scavenging for mobile and wireless electronics’. In: *IEEE Pervasive Computing* 4.1 (Jan. 2005), pp. 18–27. ISSN: 1536-1268. DOI: [10.1109/MPRV.2005.9](https://doi.org/10.1109/MPRV.2005.9).
- [2] Lopez Research. *An Introduction to the Internet of Things (IOT)*. Retrieved from: http://www.cisco.com/c/dam/en_us/solutions/trends/iot/introduction_to_IoT_november.pdf. Nov. 2013.
- [3] Jan Rabaey. *Low Power Design Essentials*. 1st. Springer Publishing Company, Incorporated, 2009. Chap. 3,5,8,10. ISBN: 0387717129, 9780387717128. DOI: [10.1007/978-0-387-71713-5](https://doi.org/10.1007/978-0-387-71713-5).
- [4] Loreto Mateu and Francesc Moll. ‘Review of energy harvesting techniques and applications for Microelectronics’. In: *Proceedings of SPIE - The International Society for Optical Engineering*. Vol. 5837. June 2005.
- [5] Drayson Technologies Limited. ‘RF Energy Harvesting for the Low Energy Internet of Things’. In: (2015), p. 7.
- [6] X. Lu et al. ‘Wireless Charging Technologies: Fundamentals, Standards, and Network Applications’. In: *IEEE Communications Surveys Tutorials* 18.2 (Secondquarter 2016), pp. 1413–1452. ISSN: 1553-877X. DOI: [10.1109/COMST.2015.2499783](https://doi.org/10.1109/COMST.2015.2499783).
- [7] Klaus Finkenzeller. *RFID Handbook: Fundamentals and Applications in Contactless Smart Cards, Radio Frequency Identification and Near-Field Communication*. 3rd. John Wiley & Sons Ltd, 2010. ISBN: 9780470665121.
- [8] S. L. Ho et al. ‘A Comparative Study Between Novel Witricity and Traditional Inductive Magnetic Coupling in Wireless Charging’. In: *IEEE Transactions on Magnetics* 47.5 (May 2011), pp. 1522–1525. ISSN: 0018-9464. DOI: [10.1109/TMAG.2010.2091495](https://doi.org/10.1109/TMAG.2010.2091495).

Bibliography

- [9] B. L. Cannon et al. ‘Magnetic Resonant Coupling As a Potential Means for Wireless Power Transfer to Multiple Small Receivers’. In: *IEEE Transactions on Power Electronics* 24.7 (July 2009), pp. 1819–1825. ISSN: 0885-8993. DOI: 10.1109/TPEL.2009.2017195.
- [10] M. P. Theodoridis. ‘Effective Capacitive Power Transfer’. In: *IEEE Transactions on Power Electronics* 27.12 (Dec. 2012), pp. 4906–4913. ISSN: 0885-8993. DOI: 10.1109/TPEL.2012.2192502.
- [11] Retrieved from: <https://www.wirelesspowerconsortium.com/developers/specification.html>.
- [12] Ian Poole. *Qi Wireless Charging Standard*. Retrieved from: <http://www.radio-electronics.com/info/power-management/wireless-inductive-battery-charging/qi-wireless-charging-standard.php>.
- [13] Ian Poole. *A4WP Wireless Charging Tutorial*. Retrieved from: <http://www.radio-electronics.com/info/power-management/wireless-inductive-battery-charging/a4wp-wireless-charging.php>.
- [14] Rich McCormick. *Former wireless charging rivals join forces as new AirFuel Alliance*. Retrieved from: <https://www.theverge.com/2015/11/3/9666960/airfuel-alliance-formed-a4wp-pma-wireless-charging>. Nov. 2015.
- [15] Retrieved from: <https://www.airfuel.org>.
- [16] S. S. Hashemi, M. Sawan and Y. Savaria. ‘A High-Efficiency Low-Voltage CMOS Rectifier for Harvesting Energy in Implantable Devices’. In: *IEEE Transactions on Biomedical Circuits and Systems* 6.4 (Aug. 2012), pp. 326–335. ISSN: 1932-4545. DOI: 10.1109/TBCAS.2011.2177267.
- [17] Y. H. Lam, W. H. Ki and C. Y. Tsui. ‘Integrated Low-Loss CMOS Active Rectifier for Wirelessly Powered Devices’. In: *IEEE Transactions on Circuits and Systems II: Express Briefs* 53.12 (Dec. 2006), pp. 1378–1382. ISSN: 1549-7747. DOI: 10.1109/TCSII.2006.885400.
- [18] H. M. Lee and M. Ghovanloo. ‘An Integrated Power-Efficient Active Rectifier With Offset-Controlled High Speed Comparators for Inductively Powered Applications’. In: *IEEE Transactions on Circuits and Systems I: Regular Papers* 58.8 (Aug. 2011), pp. 1749–1760. ISSN: 1549-8328. DOI: 10.1109/TCSI.2010.2103172.

Bibliography

- [19] Gaurav Bawa and Maysam Ghovanloo. ‘Analysis, design, and implementation of a high-efficiency full-wave rectifier in standard CMOS technology’. In: *Analog Integrated Circuits and Signal Processing* 60.1 (2009), pp. 71–81. ISSN: 1573-1979. DOI: [10.1007/s10470-008-9204-7](https://doi.org/10.1007/s10470-008-9204-7).
- [20] Ian Poole. *PSU | Linear Power Supply*, Radio-electronics.com. Retrieved from: <http://www.radio-electronics.com/info/power-management/linear-power-supply-psu/basics-tutorial.php>.
- [21] K. Keikhosravy and S. Mirabbasi. ‘A 0.13- μm CMOS Low-Power Capacitor-Less LDO Regulator Using Bulk-Modulation Technique’. In: *IEEE Transactions on Circuits and Systems I: Regular Papers* 61.11 (Nov. 2014), pp. 3105–3114. ISSN: 1549-8328. DOI: [10.1109/TCSI.2014.2334831](https://doi.org/10.1109/TCSI.2014.2334831).
- [22] G. A. Rincon-Mora and P. E. Allen. ‘A low-voltage, low quiescent current, low drop-out regulator’. In: *IEEE Journal of Solid-State Circuits* 33.1 (Jan. 1998), pp. 36–44. ISSN: 0018-9200. DOI: [10.1109/4.654935](https://doi.org/10.1109/4.654935).
- [23] Behzad Razavi. *Design of Analog CMOS Integrated Circuits*. 1st ed. New York, NY, USA: McGraw-Hill, Inc., 2001. ISBN: 0072380322, 9780072380323.
- [24] Brian M. King. *Advantages of using PMOS-type low-dropout in-ear regulators in battery applications*. Retrieved from: http://www.ti.com/sc/docs/apps/msp/journal/aug2000/aug_04.pdf. Aug. 2000.
- [25] Everett Rogers. *Stability analysis of low-dropout linear regulators with a PMOS pass element*. Retrieved from: <http://www.ti.com/lit/an/slyt194/slyt194.pdf>. 1999.
- [26] John C. Teel. *Understanding power supply ripple rejection in linear regulators*. Retrieved from: <http://www.ti.com/lit/an/slyt202/slyt202.pdf>. 2005.
- [27] U. M. Jow and M. Ghovanloo. ‘Design and Optimization of Printed Spiral Coils for Efficient Transcutaneous Inductive Power Transmission’. In: *IEEE Transactions on Biomedical Circuits and Systems* 1.3 (Sept. 2007), pp. 193–202. ISSN: 1932-4545. DOI: [10.1109/TBCAS.2007.913130](https://doi.org/10.1109/TBCAS.2007.913130).

Bibliography

- [28] ‘The concepts of inductive powering’. In: *Inductive Powering: Basic Theory and Application to Biomedical Systems*. Ed. by Koenraad Van Schuylenbergh and Robert Puers. Dordrecht: Springer Netherlands, 2009, pp. 41–76. ISBN: 978-90-481-2412-1. DOI: [10.1007/978-90-481-2412-1_2](https://doi.org/10.1007/978-90-481-2412-1_2). URL: https://doi.org/10.1007/978-90-481-2412-1_2.
- [29] M. Drakaki, A. A. Hatzopoulos and S. Siskos. ‘CMOS Inductor Performance Estimation using Z- and S-parameters’. In: *2007 IEEE International Symposium on Circuits and Systems*. May 2007, pp. 2256–2259. DOI: [10.1109/ISCAS.2007.378732](https://doi.org/10.1109/ISCAS.2007.378732).
- [30] S. S. Mohan et al. ‘Simple accurate expressions for planar spiral inductances’. In: *IEEE Journal of Solid-State Circuits* 34.10 (Oct. 1999), pp. 1419–1424. ISSN: 0018-9200. DOI: [10.1109/4.792620](https://doi.org/10.1109/4.792620).
- [31] R. F. Xue, K. W. Cheng and M. Je. ‘High-Efficiency Wireless Power Transfer for Biomedical Implants by Optimal Resonant Load Transformation’. In: *IEEE Transactions on Circuits and Systems I: Regular Papers* 60.4 (Apr. 2013), pp. 867–874. ISSN: 1549-8328. DOI: [10.1109/TCSI.2012.2209297](https://doi.org/10.1109/TCSI.2012.2209297).
- [32] Z. N. Low et al. ‘Design and Test of a High-Power High-Efficiency Loosely Coupled Planar Wireless Power Transfer System’. In: *IEEE Transactions on Industrial Electronics* 56.5 (May 2009), pp. 1801–1812. ISSN: 0278-0046. DOI: [10.1109/TIE.2008.2010110](https://doi.org/10.1109/TIE.2008.2010110).
- [33] H. M. Lee and M. Ghovalloo. ‘An Integrated Power-Efficient Active Rectifier With Offset-Controlled High Speed Comparators for Inductively Powered Applications’. In: *IEEE Transactions on Circuits and Systems I: Regular Papers* 58.8 (Aug. 2011), pp. 1749–1760. ISSN: 1549-8328. DOI: [10.1109/TCSI.2010.2103172](https://doi.org/10.1109/TCSI.2010.2103172).
- [34] R. Jacob Baker. *CMOS Circuit Design, Layout, and Simulation*. 3rd. Wiley-IEEE Press, 2010. ISBN: 0470881321, 9780470881323.
- [35] David A Johns and Ken Martin. *Analog integrated circuit design*. 2E. John Wiley & Sons, 2012. ISBN: 978-1-118-09233-0.
- [36] Paul R. Gray et al. *Analysis and Design of Analog Integrated Circuits*. 5th. New York, NY, USA: Wiley Publishing, 2009. ISBN: 978-0-470-24599-6.